

**ROLE OF TIN DOPING ON THE IMPROVED
CONDUCTIVITY OF VANADIUM PENTOXIDE CATHODE
FOR LI-ION BATTERIES:
AN ATOMISTIC MODEL**

Lappawat Ngamwongwan



**A Thesis Submitted in Partial Fulfillment of the Requirements for the
Degree of Master of Science in Physics
Suranaree University of Technology
Academic Year 2020**

การศึกษาบทบาทของการเชื่อมต่อการเพิ่มความนำไฟฟ้าของขั้วแคโทดวานเนเดียม
เพนทอกไซด์สำหรับแบตเตอรี่ชนิดลิเทียมไอออน
โดยการจำลองระดับอะตอม

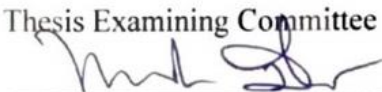


วิทยานิพนธ์นี้เป็นส่วนหนึ่งของการศึกษาตามหลักสูตรปริญญาวิทยาศาสตรมหาบัณฑิต
สาขาวิชาฟิสิกส์
มหาวิทยาลัยเทคโนโลยีสุรนารี
ปีการศึกษา 2563

**ROLE OF TIN DOPING ON THE IMPROVED CONDUCTIVITY OF
VANADIUM PENTOXIDE CATHODE FOR LI-ION BATTERIES:
AN ATOMISTIC MODEL**

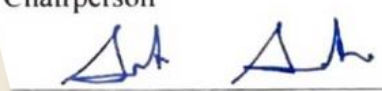
Suranaree University of Technology has approved this thesis submitted in partial fulfillment of the requirements for a Master's Degree.

Thesis Examining Committee



(Assoc. Prof. Dr. Panomsak Meemon)

Chairperson



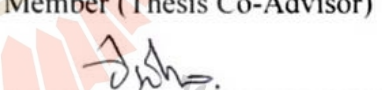
(Asst. Prof. Dr. Suwit Suthirakun)

Member (Thesis Advisor)



(Assoc. Prof. Dr. Sirichok Jungthawan)

Member (Thesis Co-Advisor)



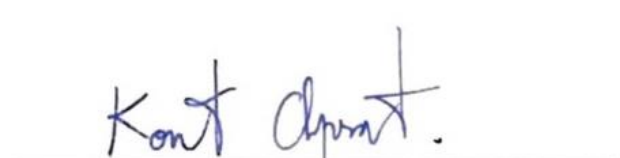
(Dr. Ittipon Fongkaew)

Member



(Dr. Pussana Hirunsit)

Member



(Assoc. Prof. Ft. Lt. Dr. Kontorn Chamniprasart)

Vice Rector for Academic Affairs

and Internationalization



(Assoc. Prof. Dr. Worawat Meevasana)

Dean of Institute of Science

ลภวัต งามวงศ์วาน : การศึกษาบทบาทของการเจือปนด้วยการเพิ่มความนำไฟฟ้าของขั้วแคโทดวานาเดียมเพนทอกไซด์สำหรับแบตเตอรี่ชนิดลิเทียมไอออนโดยการจำลองระดับอะตอม (ROLE OF TIN DOPING ON THE IMPROVED CONDUCTIVITY OF VANADIUM PENTOXIDE CATHODE FOR LI-ION BATTERIES: AN ATOMISTIC MODEL) อาจารย์ที่ปรึกษา : ผู้ช่วยศาสตราจารย์ ดร.สุวิทย์ สุธีรากุล, 130 หน้า.

วิทยานิพนธ์นี้ใช้ระเบียบวิธีการคำนวณบนพื้นฐานของทฤษฎี DFT + U ร่วมกับระบบสมการทางสถิติในการศึกษาบทบาทของการเจือปนด้วยการเพิ่มความนำไฟฟ้าของขั้วแคโทดวานาเดียมเพนทอกไซด์สำหรับแบตเตอรี่ชนิดลิเทียมไอออน โดยการเกิดของบัพทรงแบบจุดทั้งที่เกิดจากตัววัสดุเองและเกิดการเจือด้วยดีบุกได้ถูกศึกษาอย่างเป็นระบบ จากนั้นระบบสมการทางสถิติได้ถูกนำมาใช้เพื่อคาดคะเนความเข้มข้นของข้อบกพร่องแบบจุดและพาหะตัวกลาง ณ สภาวะสมดุลภายใต้เงื่อนไขความเป็นกลางทางไฟฟ้าของวัสดุ จากผลการคำนวณแสดงให้เห็นว่าเมื่อมีการเจือดีบุกนั้นการเกิดดีบุกแทนที่หมู่วานาเดิลนั้นเป็นข้อบกพร่องชนิดที่เกิดขึ้นมากที่สุด และการนำของอิเล็กตรอนถูกทำให้เกิดขึ้นได้ผ่านกระบวนการเคลื่อนที่ของโพลารอนที่เกิดขึ้นพร้อมกับข้อบกพร่องดังกล่าวหากโพลารอนนั้นสามารถหนีออกจากแรงดึงดูดของข้อบกพร่องดังกล่าวได้เมื่อเปรียบเทียบการเคลื่อนที่ของโพลารอนในวัสดุที่ไม่มีเจือปน พบว่าการเจือดีบุกมีบทบาทสำคัญในการเพิ่มความเข้มข้นของโพลารอนที่ถูกยึดไว้ในข้อบกพร่องผ่านการเกิดข้อบกพร่องดีบุกแทนที่หมู่วานาเดิล อีกทั้งดีบุกยังช่วยให้โพลารอนเหล่านั้นสามารถเคลื่อนที่ออกจากบริเวณศูนย์กลางของข้อบกพร่องได้ง่ายขึ้น หรือพูดอีกนัยหนึ่งว่าการที่อะตอมดีบุกเข้าไปแทนหมู่วานาเดิลนั้นช่วยลดอันตรกิริยาระหว่างศูนย์กลางของข้อบกพร่องแบบจุดกับโพลารอนที่ถูกยึดไว้ ส่งผลให้จำนวนพาหะตัวกลางในระบบเพิ่มขึ้นรวมถึงการนำไฟฟ้าของวัสดุที่ถูกเจือด้วยดีบุกดีขึ้นด้วย

สาขาวิชาฟิสิกส์
ปีการศึกษา 2563

ลายมือชื่อนักศึกษา ลภวัต งามวงศ์วาน
ลายมือชื่ออาจารย์ที่ปรึกษา Dr. Sirichok
ลายมือชื่ออาจารย์ที่ปรึกษาร่วม Sirichok

LAPPAWAT NGAMWONGWAN : ROLE OF TIN DOPING ON THE
IMPROVED CONDUCTIVITY OF VANADIUM PENTOXIDE CATHODE
FOR LI-ION BATTERIES: AN ATOMISTIC MODEL. THESIS ADVISOR :
ASST. PROF. SUWIT SUTHIRAKUN, Ph.D. 130 PP.

VANADIUM PENTOXIDE/POLARON/ POINT DEFECTS/ TIN-DOPING

In this thesis, a computational tool based on DFT+U coupled with a statistical model was utilized to study the role of the Sn doping on the improved conductivity of V_2O_5 based cathode for Li-ion batteries. The formation of point defects, including intrinsic and Sn-related defects, were investigated systematically. The statistical model with electroneutrality was applied to estimate the defect and carrier concentration at equilibrium. The computations reveal that neutral Sn substitution for VO (Sn_{VO}) is the most dominant in the presence of Sn doping. The electron conduction can occur by the transport of bound polarons in Sn_{VO} , escaping the defect center. Compared to the material without doping, Sn doping plays a significant role in the increase in the concentration of bound polarons via the formation of neutral Sn_{VO} . In addition, these polarons can escape from the defect center more easily. In other words, Sn substitution slightly weakens the interaction between defect center and the bound polaron. As a result, the number of charge carriers increase as well as the conductivity of the Sn-doped material.

School of Physics

Academic Year 2020

Student's Signature ลพพาวต งามวงศ์วาน

Advisor's Signature สุวิท สุทธิรักษ์

Co-Advisor's Signature Sirichok

ACKNOWLEDGEMENTS

I would like to express appreciation to my thesis advisor Asst. Prof. Dr. Suwit Suthirakun and co-advisor Assoc. Prof. Dr. Sirichok Jungthawan for their patience, kind support, guidance, discussion and encouragement throughout my thesis. I would like to acknowledge Assoc. Prof. Dr. Panomsak Meemon, Dr. Ittipon Fongkaew and Dr. Pussana Hirunsit for contributing as the thesis-examining committees. I am thankful to Dr. Ittipon Fongkaew for his help with discussion in the section of point defect I would like to thank the Development and Promotion of Science and Technology Talents Project (DPST, THAILAND) and Center for advanced nanomaterials and characterization for the scholarship during my Master's degree program and for financial support of this work. I acknowledge NSTDA Supercomputer Center (ThaiSC) and Institute of Science, Suranaree University of Technology, for computational resources. I would like to thank people from the School of Physics, Institute of Science, Suranaree University of Technology for their guidance and friendship. I also appreciate Apinya Ngoipala for kind support, suggestions, and comments for the whole time of doing this thesis. I am grateful to my friends in Computational Material Science and Catalysis (COMSCAT) Group for their assistance and friendship. Finally, I would like to express thanks to my family for their love, kind support and encouragement.

Lappawat Ngamwongwan

CONTENTS

	Page
ABSTRACT IN THAI.....	I
ABSTRACT IN ENGLISH	II
ACKNOWLEDGEMENTS.....	III
CONTENTS.....	IV
LIST OF TABLES	VII
LIST OF FIGURES	VIII
LIST OF ABBREVIATIONS.....	XIII
CHAPTER	
I INTRODUCTION.....	1
1.1 Li-ion batteries and cathode materials	1
1.2 Vanadium pentoxide as cathode material	5
1.3 Tin doping.....	9
1.4 Research objective	14
1.5 Scope and limitations.....	14
1.6 References.....	16
II ATOMISTIC MODELING.....	25
2.1 Many-body Schrödinger equation.....	25
2.2 Density functional theory (DFT)	27
2.3 The exchange-correlation functional	32
2.4 DFT+U approach	33

CONTENTS (Continued)

	Page
2.5	Wavefunction and pseudopotential..... 34
2.6	Summary of computational details 36
2.7	References..... 38
III	FORMATION OF INDIVIDUAL POINT DEFECT 41
3.1	Introduction..... 41
3.2	Computational method for studying point defects..... 42
3.2.1	Construction of defective models 42
3.2.2	Defect formation energy 42
3.2.3	Chemical potentials..... 43
3.3	Perfect vanadium pentoxide crystal 47
3.4	Intrinsic defects..... 49
3.5	Sn-related defects..... 60
3.6	Discussion..... 65
3.7	References..... 65
IV	DEFECT CONCENTRATIONS 73
4.1	Introduction..... 73
4.2	Computational methods 73
4.2.1	Defect concentrations at annealing 73
4.2.2	Defect concentrations after quenching..... 76
4.3	Defect concentrations in the absence of tin doping 76
4.4	Defect concentrations in the presence of tin doping..... 79
4.5	Discussion..... 83

CONTENTS (Continued)

	Page
4.6 References.....	83
V SMALL POLARON CONDUCTION.....	85
5.1 Introduction.....	85
5.2 Polaron as charge carriers.....	85
5.3 Polaron transport calculations.....	87
5.4 Polaron transport in the perfect crystal.....	89
5.5 Polaron transport in the absence of tin doping.....	91
5.6 Polaron transport in the presence of tin doping.....	96
5.7 Discussion.....	99
5.8 References.....	101
VI CONCLUSIONS.....	103
APPENDICES.....	106
APPENDIX A TUNING U PARAMETER.....	107
APPENDIX B PUBLICATION AND PRESENTATIONS.....	112
CURRICULUM VITAE.....	130

LIST OF TABLES

Table	Page
3.1 Bader charge analysis of Sn atom in Sn oxides and Sn-related defects.....	64
5.1 The reaction energy (ΔE), the associated energy barriers for forward direction (E_a) and reverse direction (E_r) of polaron migration in pristine system	90
5.2 The reaction energy (ΔE), the associated energy barriers for forward direction (E_a) and reverse direction (E_r) of polaron migration in the absence of Sn doping system which is modeled as the supercell containing a neutral O1 vacancy.....	93
5.3 The reaction energy (ΔE), the associated energy barriers for forward direction (E_a) and reverse direction (E_r) of polaron migration in the absence of Sn doping system which is modeled as the supercell containing a neutral Sn substitution for VO.....	98
5.4 The summary of important numbers, i.e., the polarons concentration (C_0), the depth of potential well (V), and the effective barrier for being unbound polaron (E_a) for the polaron transport in each system.....	101
A.1 The calculated structural parameters (lattice constants and bond lengths), band gap energy, and the position of polaronic state position compared with the experimental result.....	109

LIST OF FIGURES

Figure	Page
1.1 Schematic picture illustrates the working principles of a lithium-ion battery involved the lithium ions flow and electron flow during discharge and charge processes	2
1.2 Schematic illustration of Li ion intercalation during discharge process in V_2O_5 cathode with polaron formation and migration.....	7
1.3 Three possible defect sites of Sn impurity including i) Sn interstitial, ii) Sn substitution for V, and iii) Sn substitution for V combined with O vacancy.....	12
2.1 The scheme of self-consistent field (SCF) iterations for solving the Kohn-Sham equations and obtaining calculate total energy and other properties	31
2.2 Comparison of an all-electron wavefunction in Coulomb potential and a pseudo-wavefunction in pseudopotential. The r_c represents the cutoff radius where all-electron and pseudo wavefunction and potential are the same.....	35
3.1 The assessable range of chemical potential of O (μ_O) for V_2O_5 single phase synthesis. The range is limited by O-poor condition and O-rich condition which is altered under different growth condition i.e. annealing temperature and oxygen partial pressure. The blue and yellow dashed lines also show the O-rich limit under air with annealing temperature of 350 and 450 °C	46

LIST OF FIGURES (Continued)

Figure	Page
3.2 (a) unit cell of orthorhombic V_2O_5 containing 14 atoms where gray and red atoms represent V and O, respectively. (b) The pink polyhedron illustrates the distorted squared pyramid of VO_5 and all corresponding V-O bond lengths are in Å. (c) The calculated projected density of states (PDOS) of pristine V_2O_5 . The zero in energy is set to VBM where dashed line indicates the energy level of the last occupied electron.....	49
3.3 (a-j) Defect structures (near defect region) and gap state charge density of electronic defects, neutral vacancies, and neutral interstitials. The yellow and blue charge density represents occupied and unoccupied gap states. (k-m) The calculated PDOS of selected defects. (n) their defect formation energies at various charge states are plotted as a function of Fermi energy. The zero Fermi energy and its upper limit are set at VBM and CBM. The set of elemental chemical potentials is set as the experimental condition. The slope of each line indicates charge state of the defect, and only the most favorable charge state for a given Fermi energy is shown.	51
3.4 The crystal structure of O interstitial in two configurations which are (a) normal interstitial and (b) split interstitial. Only structures at the region near the defect site are shown for clarity. Also, the relative energy of each configuration compared to the lowest energy configuration.....	57

LIST OF FIGURES (Continued)

Figure	Page
3.5 (a-c) Defect structures (near defect region) and gap state charge density of (a) Sn interstitial, Sn_i (b) Sn substitution for V, Sn_V and (c) Sn substitution for VO, Sn_{VO} . Sn doping atoms are illustrated by dark blue balls. The yellow and blue charge density represents occupied and unoccupied gap states. (d-f) The corresponding PDOS of Sn-related defects. (g) their defect formation energies at various charge states are plotted as a function of Fermi energy.....	61
4.1 Illustration of the concentrations of some selected defects and carriers at different charge states occurred under thermodynamic equilibrium in the material without Sn doping at annealing temperature of 723 K and quenching into 300 K. The inset shows equilibrium Fermi energy of the system under annealed and quenched conditions.....	77
4.2 Illustrations of equilibrium defect concentration and Fermi energy as a function of Sn doping concentration under annealed and quenched conditions. (a) all charged states concentration of selected defects and carriers. (b) equilibrium Fermi energy. (c-d) concentration of dominant Sn-related defects at various charge states under annealing (c) and quenching (d) temperature.....	80
4.3 Defect structure (near defect region) of neutral complex defect between Sn substitution for V and Sn substitution for VO denoted as $[\text{Sn}_{VO} - \text{Sn}_V]$. The corresponding PDOS and defect formation energy of the complex are also plotted.....	82

LIST OF FIGURES (Continued)

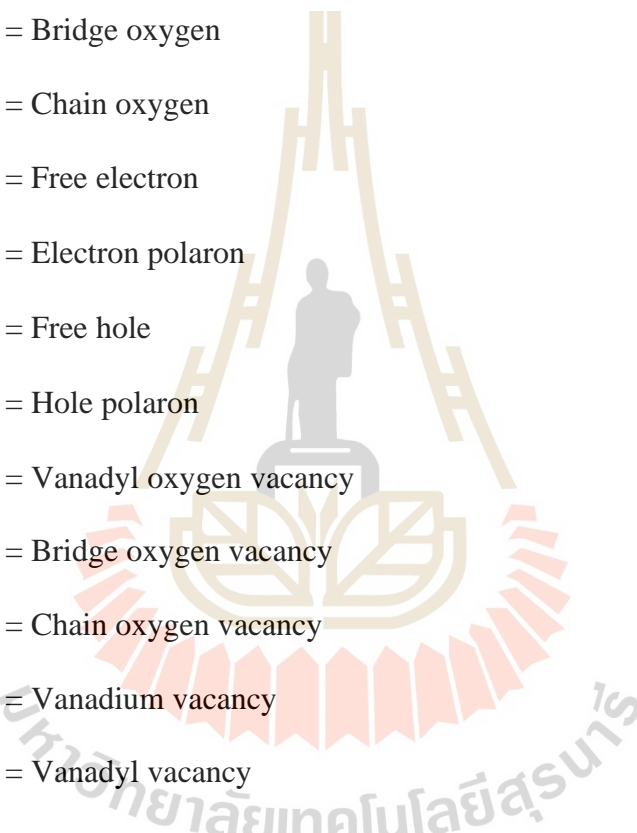
Figure	Page
<p>5.1 A schematic illustration of polaron transport in metal oxides. (a) lattice reorganization along the polaron hopping path from a M site to a neighboring M site, illustrating the change of bond length due to Coulombic force induced by electron charge. (b) Energy profile of the polaron hopping process between two M sites with respected to geometric configuration. W_H represents the energy required to generate the geometric configuration that suitable for hopping, i.e., transition state.....</p>	88
<p>5.2 A schematic illustration of polaron migration paths in pristine system. The diagrams display the nearest-neighbor and in-plane consecutive hopping. The numbers in circles are energies relative to the configuration I where the polaron located at initial site (I site). The numbers next to arrow indicate the hopping barriers. These numbers are equivalent to those in Table 5.1, and all energies are shown in eV.....</p>	91
<p>5.3 A schematic illustration of polaron migration paths in the absence of Sn doping system which is modeled as the supercell containing a neutral O1 vacancy. The diagrams display the nearest-neighbor and in-plane consecutive hopping. The numbers in circles are energies relative to the configuration I where the polaron located at initial site (I site). The numbers next to arrow indicate the hopping barriers. These numbers are equivalent to those in Table 5.2, and all energies are shown in eV.....</p>	95

LIST OF FIGURES (Continued)

Figure	Page
5.4 A schematic illustration of polaron migration paths in the presence of Sn doping system which is modeled as the supercell containing a neutral Sn substitution for VO. The diagrams display the nearest-neighbor and in-plane consecutive hopping. The numbers in circles are energies relative to the configuration I where the polaron located at initial site (I site). The numbers next to arrow indicate the hopping barriers. These numbers are equivalent to those in Table 5.3, and all energies are shown in eV.....	97
5.5 A schematic illustration of a bound polaron hop away from the defect center leads to an unbound polaron and a single donor. E_a represents the effective energy barrier for bound polaron hopping from the defect region to the bulk region. V represents the potential well of the defect region which is defined by the energy difference between polaron located in the defect center and polaron in the bulk region.....	100
A.1 Illustration of the position of polaronic state of Li-intercalated V_2O_5 and band gap energy of pristine V_2O_5 as a function of U parameters ranging from 2.0 to 6.0 eV. The calculated position of state to band gap ratio is also plotted with the experimental ratio (dotted line) in order to calibrate the appropriate U parameter.....	110

LIST OF ABBREVIATIONS

LIB	= Li-ion battery
EV	= Electric vehicle
NMC	= $\text{LiNi}_{1-x-y}\text{Mn}_x\text{Co}_y\text{O}_2$
NCA	= $\text{LiNi}_{1-x-y}\text{Co}_x\text{Al}_y\text{O}_2$
UPS	= Ultraviolet photoelectron spectroscopy
XPS	= X-ray photoelectron spectroscopy
XANES	= X-ray absorption near edge structure spectroscopy
XRD	= X-ray diffraction spectroscopy
FTIR	= Fourier transform infrared spectroscopy
DFT	= Density functional theory
U	= Hubbard U parameter
SCF	= Self-consistent field
LDA	= Local density approximation
GGA	= Generalized gradient approximation
PBE	= Perdew–Burke–Ernzerhof functional
PW91	= Perdew–Wang functional
PAW	= projector-augmented wave method
vdW	= Van der Waals
VASP	= Vienna Ab initio Simulation Package

LIST OF ABBREVIATIONS (Continued)

M	= Cation dopant
VO	= Vanadyl group
O1	= Vanadyl oxygen
O2	= Bridge oxygen
O3	= Chain oxygen
e^-	= Free electron
η^-	= Electron polaron
h^+	= Free hole
η^+	= Hole polaron
vac _{O1}	= Vanadyl oxygen vacancy
vac _{O2}	= Bridge oxygen vacancy
vac _{O3}	= Chain oxygen vacancy
vac _V	= Vanadium vacancy
vac _{VO}	= Vanadyl vacancy
O _i	= Oxygen interstitial
V _i	= Vanadium interstitial
Sn _i	= Tin interstitial
Sn _V	= Tin substitution for vanadium
Sn _{VO}	= Tin substitution for vanadyl
DOS	= Density of states
PDOS	= Projected density of states

LIST OF ABBREVIATIONS (Continued)

VB	= Valence band
VBM	= Valence band maximum
CB	= Conduction band
CBM	= Conduction band minimum
μ	= Chemical potential
T	= Temperature
p	= Oxygen partial pressure
DFE	= Defect formation energy
CTL	= Charge transition level
LE	= Linear interpolation method
CINEB	= Climbing Image Nudge Elastic Band method

CHAPTER I

INTRODUCTION

1.1 Li-ion batteries and cathode materials

Li-ion batteries (LIBs) are currently the most popular energy storage system which are widely used in various applications ranging from mobile phones, laptops, home batteries, electric vehicles (EVs), and power plants. In addition, the battery technology is of great importance because it is a key limiting factor of the emergence of other technologies, especially in the case of EVs. In particular, the driving range on a single charge of EVs is limited on the gravimetric and volumetric energy density of the batteries. Thus, the battery performances need to be further improved in term of low cost, long lasting, high safety, and high energy capacity in order to overcome the petroleum-based fuel. (Cheng *et al.*, 2011; X. Liu *et al.*, 2018; Michael M. Thackeray *et al.*, 2012; M. S. Whittingham, 1976; Xu *et al.*, 2012).

Rechargeable LIB is an electrochemical cell which mainly consists of anode, cathode, separator, and electrolyte. The working principle is basically an energy conversion between chemical and electrical energy during charge/discharge process. When the battery is fully charged, Li-ions are inserted in the entire of anode host. These Li-ions have high chemical potential and are ready to intercalate into the cathode framework. Until discharging, the battery is connected to an electric appliance and the circuit is closed as shown in Figure 1.1. These Li-ions readily transports through the electrolyte and separator, driven by the chemical potential

difference between two electrodes. Simultaneously, counter-electrons also migrate toward the cathode to compensate the flow of positively charged Li-ions. The transport of energetic electrons occurs via external circuit due to the blockage of the separator. The generated electricity can perform electronic work until the LIB is fully discharged. The recharge process can be done by applying an external potential to drive the reverse reaction. In particular, Li-ions are inserted into anode framework and becomes high chemically active again.

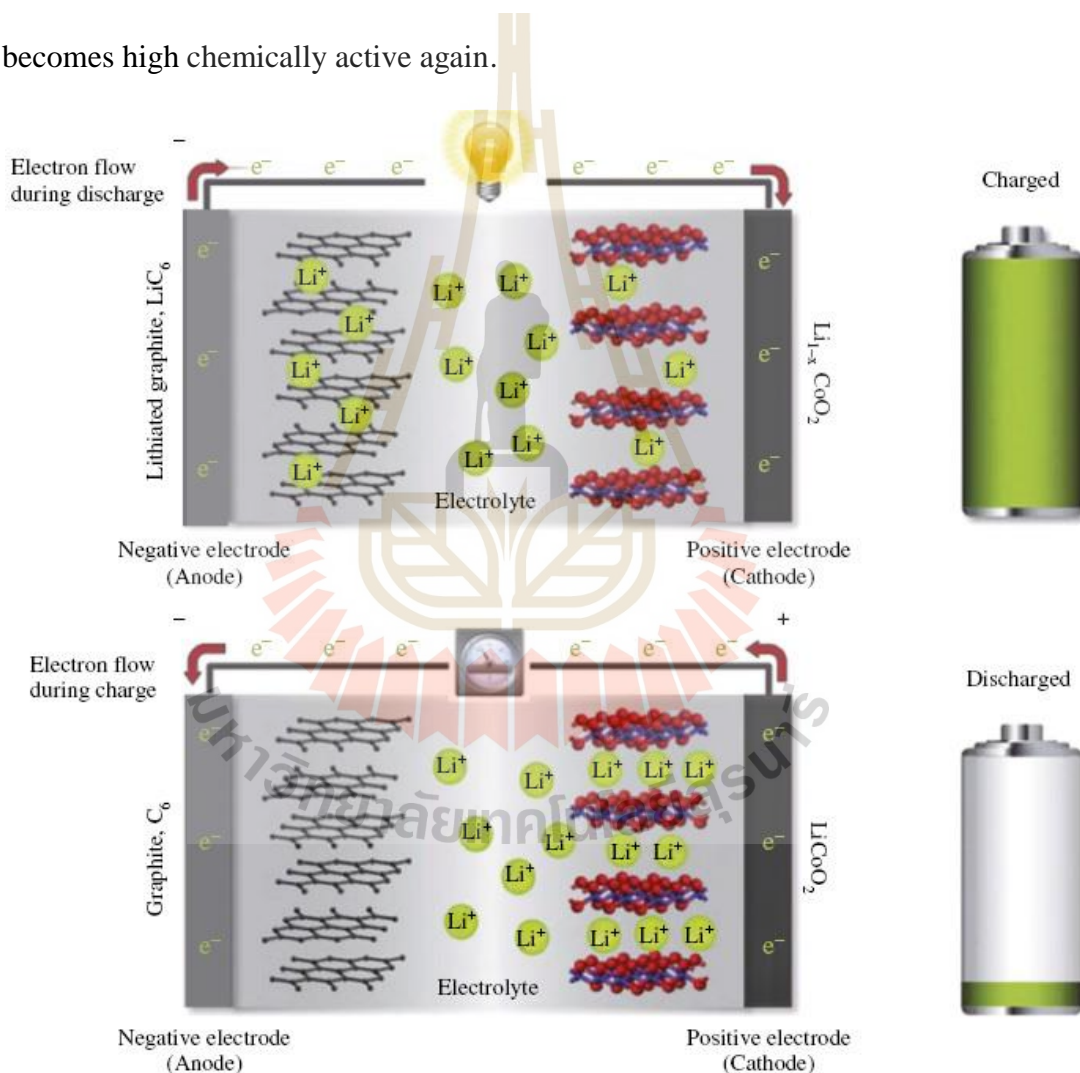


Figure 1.1 Schematic picture illustrates the working principles of a lithium-ion battery involved the lithium ions flow and electron flow during discharge (top panel) and charge processes (bottom panel) (Michael M. Thackeray *et al.*, 2012).

It should be noted that chemistry and morphology of electrode materials play substantial roles on battery performances (Xu *et al.*, 2012). In fact, the energy capacity of the battery corresponds to the number of Li accommodated in electrode materials. The rate capability of the battery is related to the kinetics of Li-ions and electrons transport especially inside electrode materials. Also, the reversibility of the charge/discharge process directly affects to the battery lifespan. Therefore, to boost the battery performance, many attempts in the discovery and optimization of electrode materials have been employed (Nitta *et al.*, 2015).

Nowadays, carbon-based materials e.g. graphite is the most widely used anode in commercial LIBs (Lu *et al.*, 2018; H. Wu *et al.*, 2012). On the other hand, various cathode materials, based on lithium intercalation in transition-metal oxides, polyanions, or layered materials, have been intensively investigated for high performance LIBs (Daniel *et al.*, 2014; Massé *et al.*, 2016). There are currently three main material families that are commercial or near commercial cathode for LIBs (Daniel *et al.*, 2014).

Layered oxides (LiMO_2) have been the most widely commercialized cathode materials for LIBs. Since 1980, LiCoO_2 was first proposed as the intercalated cathode for LIBs (Mizushima *et al.*, 1980). However, the irreversible phase transformation of the parent structure was observed after extracting 50% of the lithium. This poor structural instability limits the experimental capacity (at around 140 mAh/g) as compared to its theoretical capacity (280 mAh/g) (Daniel *et al.*, 2014). Then, a layered LiNiO_2 with iso-structure was proposed. Although it has high reversible capacity, its low electrochemical activity was caused by the Li/Ni antisite defect (Dahn *et al.*, 1990). In addition, the solid solution between Co and Ni could decrease

the Li/Ni disorder and exhibit better performance (Whitfield *et al.*, 2005). For example, $\text{LiNi}_{1-x-y}\text{Mn}_x\text{Co}_y\text{O}_2$ (NMC) provides high operating voltages (~ 4.7 V) and reversible capacity (200 mAh/g) in the cut-off voltage range 2.8–4.6 V (C.-f. Zhang *et al.*, 2009). Likewise, $\text{LiNi}_{1-x-y}\text{Co}_x\text{Al}_y\text{O}_2$ (NCA) also exhibit better electrochemical performance (Chen *et al.*, 2004). These materials are now used worldwide in high power and high energy LIBs (Goodenough and Kim, 2010; Manthiram, 2020). Nevertheless, cobalt is quite expensive and may outstrip production in the short coming due to the expansion of electric vehicle market. Also, nickel is an essential component in other industries e.g. stainless steel and non-ferrous alloy. Hence, many efforts tend to decrease or eliminate cobalt and nickel from cathode materials (M. Li and Lu, 2020; W. Li *et al.*, 2020; Schmuch *et al.*, 2018).

Spinel oxides (LiM_2O_4) are also investigated. For example, LiMn_2O_4 was first proposed for the LIBs in 1983 (M. M. Thackeray *et al.*, 1983). Compared to layered oxides LiMO_2 , it is a low cost, environmentally friendly, and safer alternative. However, it exhibits low practical capacity and energy density compared to other cathodes and suffers from capacity fading. Various strategies were employed to enhance the electrochemical performance of LiMn_2O_4 . Among them, doping with nickel ($\text{LiNi}_{0.5}\text{Mn}_{1.5}\text{O}_4$) reveals high operating voltage and good rate capability with the experimental capacity of 140 mAh/g (Ohzuku *et al.*, 1999).

Olivine phosphates (LiFePO_4) was proposed as promising alternative cathode materials (Padhi *et al.*, 1997) due to its low cost, low toxicity, high safety, low volume expansion, low capacity fading and high specific capacity of 170 mAh/g (Whittingham, 2004). However, LiFePO_4 exhibits a relatively low discharge voltage of 3.4 V which limits the power density of the battery (Whittingham, 2004). In

addition, it suffers from the low ionic conductivity due to the slow 1D migration of Li-ions.

A promising cathode material must satisfy many criteria such as low cost, environmentally friendly, high electrochemical performance, high capacity, high and stable voltage, compatible with the electrolyte, and high structural stability upon cycling to ensure long cycle life. Accordingly, a material that simultaneously satisfies all criteria has not yet been discovered (Massé *et al.*, 2016). Therefore, the development of non-commercialized cathode materials and discovery of new materials are of great importance. For instance, many researches pay attention on alternative polyanionic compounds, e.g. silicates (Li_2MSiO_4) (Nytén *et al.*, 2005), borates (LiMBO_3) (Legagneur *et al.*, 2001), and tavorite (LiMPO_4F) (Ramesh *et al.*, 2010), layered metal oxides, e.g. MoO_3 (Hu *et al.*, 2015) or V_2O_5 (Zhu *et al.*, 2020), and the emerging 2D materials like MXenes (Byeon *et al.*, 2017). In this work, the V_2O_5 , a promising cathode material, was considered. In addition, it provides a remarkably high theoretical capacity of 442 mAh g^{-1} over the commercialized cathodes e.g. LiCoO_2 and LiFePO_4 (Huang *et al.*, 2015).

1.2 Vanadium pentoxide as cathode material

In 1976, V_2O_5 was first proposed as a Li-ion intercalation host for cathode of Li-ion batteries by Whittingham *et al.* (M. Stanley Whittingham, 1976). The most stable phase orthorhombic $\alpha\text{-V}_2\text{O}_5$ has quasi-2D structure, and the layers of V_2O_5 are held together by weak Van der Waals interaction. The open-layered structures allow the facile Li-ions insertion into their interlayer space, leading to the plenty of insertion

sites (F. Liu *et al.*, 2012). The energy capacity of V_2O_5 is related to the reversible Li-ions insertion/extraction so called intercalation reaction, i.e.,



In addition, V_2O_5 also has the accessible redox pair e.g. V^{5+}/V^{4+} and V^{4+}/V^{3+} as well as high potential to drive the inserted Li-ions move into structure for the Li intercalation process (Chernova *et al.*, 2009; Marley *et al.*, 2015).

During the Li intercalation, the intercalated phase or $Li_xV_2O_5$ is altered by the values of x depending on concentration of Li-ions inserted within the host. Initially, a slightly distorted α -phase is stable ($x < 0.1$). Further lithiation can lead to stabilization in ϵ -phase ($0.35 < x < 0.7$) and δ -phase ($0.7 < x < 1$). In γ -phase ($1 < x < 2$), the phase transitions involve increased in separation of the V_2O_5 layers and produce structural distortions. Upon further lithiation ($2 < x < 3$), the γ -phase will be irreversibly transformed to the ω -phase (Mai *et al.*, 2010; Wang *et al.*, 2011; Whittingham, 2004). It should be noted that the irreversible of phase transition is problematic for experimental capacity and lifespan of the battery.

During the Lithiation process, ionized Li-ions and their associated electrons are inserted and diffused inside the V_2O_5 host matrix as shown in Figure 1.2. When electrons transport through the material, they initially localize at V-centers leading to the reduction of V^{5+} into V^{4+} as well as creation of small lattice distortion around the V-centers. The coupling between the localized electron and the distortion forms a quasi-particle namely small electron polaron since the distortions are in a length scale of unit cell size. (De Jesus *et al.*, 2016). The formation of the polaron can be supported by both experiments and computations of $Li_xV_2O_5$. Firstly, X-ray photoelectron spectroscopy (XPS) reveals that the number of reduced state V^{4+} is

increasing with lithiation (Q. H. Wu *et al.*, 2005). Secondly, the X-ray absorption near edge structure (XANES) illustrates the occupancy of electron in V-3d_{xy} lowest-lying state in conduction band due to the energy band splitting. This agrees well with the calculated partial density of state and crystal field theory (De Jesus *et al.*, 2016). Thirdly, the polaronic state corresponding to localized electron can be found by using the ultraviolet photoelectron spectroscopy (UPS) where the peak is about 1 eV above valence band edge (Q. H. Wu *et al.*, 2005) associated with the calculated peak in the band gap (Scanlon *et al.*, 2008). Lastly, the calculated formation energy of polaron is less than that of the delocalized electron by 0.22 eV (De Jesus *et al.*, 2016). These findings illustrate the formation of electron polaron in V₂O₅ host material. Furthermore, the electron polarons can be migrated through the material via polaron hopping process to the adjacent V-center. This process requires the thermal activation to overcome the calculated energy barrier of 0.22 eV for the polaron hopping along [110] direction. The details of the hopping process was investigated and written in previous work (Wattaisong *et al.*, 2019).

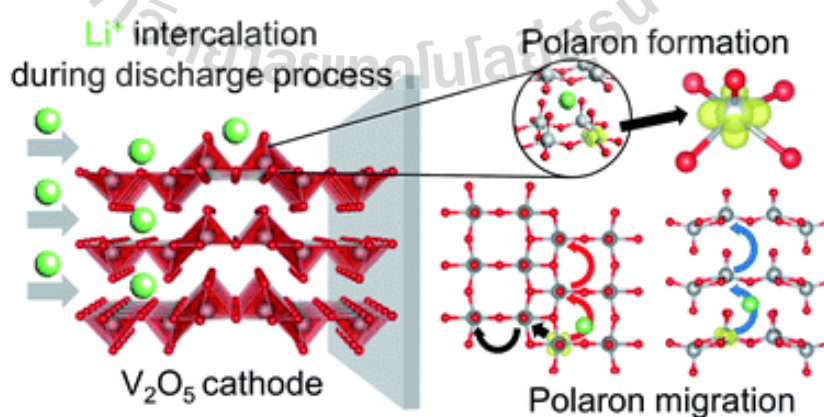


Figure 1.2 Schematic illustration of Li ion intercalation during discharge process in V₂O₅ cathode with polaron formation and migration (Wattaisong *et al.*, 2019).

Lithiation process at the low Li concentration limit was investigated under DFT method (Carrasco, 2014; Parija *et al.*, 2016; Suthirakun, Genest, *et al.*, 2018; Suthirakun, Jungthawan, *et al.*, 2018). The calculation reveals that the corresponding electron polaron prefers to locate nearby that Li-ion in order to minimize the total energy of the system. While other configurations, when polaron is far from Li-ion, could raise the energy up to 0.22 eV. This is due to the attractive force between positively charged Li-ion and negatively charged polaron.

After Li is inserted in the V_2O_5 matrix, it can further move from one site to the adjacent site by the Li diffusion. Interestingly, the Li-ion is likely to stick with the polaron, therefore, the Li diffusion will be occurred in a coupled fashion with the associated polaron (Maxisch *et al.*, 2006). In fact, the Li-ion could migrate along b direction and follow by the polaron hopping, alternately. This scenario has been proposed to be the lowest energy barrier path. Notably, the polaron hopping also plays an important role in Li diffusion process because it might be a rate limiting step (Suthirakun, Genest, *et al.*, 2018). This is similar to Li diffusion in other intercalated materials e.g. Li_xTiO_2 , (Kerisit *et al.*, 2009; Sushko *et al.*, 2010) Li_xFePO_4 , (Maxisch *et al.*, 2006), Li_2FeSiO_4 (Bui *et al.*, 2012), and TiO_2 host (J. Yu *et al.*, 2012).

Notably, in case of V_2O_5 , the electrons are conducted through polaron hopping process, which occasionally slower than the band-like electron conduction. The polaron hopping also plays an important role in Li-ion coupled polaron diffusion. The kinetics of these processes rely on the thermal activation to overcome the activation energy, which can be implied to macroscopic transport, i.e., electronic and ionic conductivity of the material. In ambient temperature, V_2O_5 is suffered from limited transport properties, i.e., moderate electron conductivity ($10^{-3} - 10^{-2} \text{ S cm}^{-1}$) and low

Li diffusion coefficient ($10^{-13} - 10^{-12} \text{ cm}^2 \text{ s}^{-1}$), resulting in slow rate capability (Huang *et al.*, 2015). In addition, the experimental energy capacity of V_2O_5 cathode is currently far from theoretical one, which could be originated from the sluggish electronic and ionic conductivity as well as irreversible of phase transition. These drawbacks could hinder V_2O_5 to be commercialized for high-performance LIBs.

1.3 Tin doping

In order to alleviate the drawbacks of material and to improve the electrode performance, several synthesis strategies have been utilized. Firstly, dimensional reduction of the particle size into nanoscale e.g. nanoparticle, nanowire, nanosheet, or nanoporous structure can significantly enhance the transport kinetics since Li diffusion and polaron hopping distance are shortened (Bruce *et al.*, 2008; H. Zhang *et al.*, 2011). Secondly, composite formation or coating with conductive carbon e.g. carbon black on V_2O_5 nanomaterials can enhance the electronic conductivity and suppresses the aggregation of the particles (Huang *et al.*, 2015). Finally, doping with oxygen vacancy or cation impurity could introduce more redox pairs e.g. $\text{V}^{5+}/\text{V}^{4+}$ and $\text{V}^{4+}/\text{V}^{3+}$, resulting in the improved electron conductivity (Z. Zhang *et al.*, 2010). In fact, some cation impurities could enlarge the interlayer space providing increased chances for Li intercalation (Zhan *et al.*, 2009).

Among cation impurities, Sn doping demonstrates a substantial change in electrochemical performance compared to the undoped as proposed in previous works (Y. W. Li *et al.*, 2013; Z. Y. Li *et al.*, 2016; Xing *et al.*, 2019). For example, 4% Sn-doped V_2O_5 provided higher specific capacity than the pristine (220.4 mAh g^{-1} vs 148.6 mAh g^{-1} at 500 mA g^{-1}) as well as the higher lithium diffusion coefficient

($4.45 \times 10^{-11} \text{ cm}^2 \text{ s}^{-1}$ vs $2.84 \times 10^{-11} \text{ cm}^2 \text{ s}^{-1}$) (Z. Y. Li *et al.*, 2016). Likewise, in the other work (Le *et al.*, 2019), the fabricated Sn-doped V_2O_5 has been retained the specific capacity of 334 mAh g^{-1} which is more than twice of the capacity in undoped film (157 mAh g^{-1}) at 500 mA g^{-1} . In addition, rate capability and cyclic stability of the batteries are improved by doping with Sn. Recently, a mesopore structure of 4% Sn-doped V_2O_5 can enhance electrical conductivity by four times compared to undoped sample (1.9×10^7 vs $5.7 \times 10^7 \text{ S/m}$) (Xing *et al.*, 2019). However, the electrode performance is also related to the doping concentration. For instances, the excessive doping e.g. 8% can instead diminish the electrochemical performance (Z. Y. Li *et al.*, 2016). Moreover, if the concentration is greater than the doping limit around 10%, the excess Sn dopant will be formed as secondary phase of SnO_2 (Rajeshwari *et al.*, 2018).

To the best of our knowledge, the origin of the improvement is not clearly presented in the literature. Based on the previous experiments (Y. W. Li *et al.*, 2013; Z. Y. Li *et al.*, 2016), the authors proposed the role of Sn impurity as followed. Firstly, Sn doping can affect the morphology and reduce the size of synthetic particles. According to SEM observations, the particle size of Sn-doped nanosheet is smaller than that of the undoped (45 nm vs 23 nm) (Le *et al.*, 2019). Secondly, Sn doping can increase $\text{V}^{4+}/(\text{V}^{4+}+\text{V}^{5+})$ ratio leading to the number of electron polarons, which might be affect to polaron hopping rate and electrical conductivity. Thirdly, the occupancy of Sn interstitial at interlayer cavity can stabilize the host structure during Li intercalation/extraction. Lastly, Sn impurity defects could be responsible for the nucleation centers for phase transformation. However, there is still lacking the

explanation and evidence especially the defect formation and charge carrier contribution upon Sn doping.

Based on the previous experiments, there is still a contradiction in preference of Sn doping site and contribution of associating carrier. Three possibilities of Sn doping models are proposed (see Figure 1.3). Firstly, Sn could be intercalated into the cavity between two V_2O_5 layers so called Sn interstitial. This defect could enlarge the interlayer space, leading to the slight expansion of unit cell along a and c directions as reported in X-ray diffraction (XRD) spectra (Le *et al.*, 2019; Y. W. Li *et al.*, 2013). Also, the XPS spectra shows the stable oxidation state of Sn^{4+} rather than Sn^{2+} , which produce compensating electron polarons nearby the Sn interstitial (Y. W. Li *et al.*, 2013). Secondly, the model of Sn substitution for V was also reported. The lattice expansion upon Sn doping can be originated from Sn located at V site due to the fact that Sn^{4+} has ionic radius 22% larger than V^{5+} (Xing *et al.*, 2019). Since Sn^{4+} replacing for V^{5+} is negatively charge defect, it could influence other positively charged compensation and do not generate electron polaron. Lastly, the Sn substitution can further induce the formation of oxygen vacancy (Z. Y. Li *et al.*, 2016). To the best of our knowledge, there is no experimental evidence apart from the XRD results, mentioning or confirming the preferential site of the Sn heteroatom. Indeed, Sn could be incorporated in both sites depending on synthetic conditions, e.g. synthesis method, doping concentration, temperature, and oxygen partial pressure. Identifying the preferential doping site and associating charge compensation mechanism are necessary to better understand the role of the Sn dopant on electrode performance.

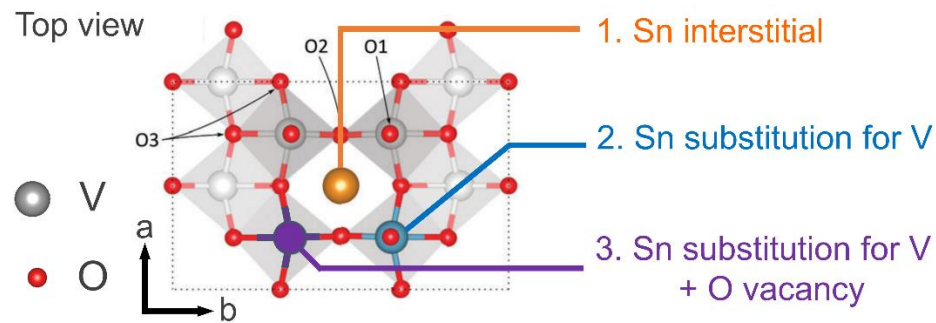


Figure 1.3 Three possible defect sites of Sn impurity including i) Sn interstitial, ii) Sn substitution for V, and iii) Sn substitution for V combined with O vacancy.

Recently, a theoretical study on defect formation in cation-doped V_2O_5 has been reported (McColl *et al.*, 2018). The classical pair-potential method was utilized to predict the location of cation dopants (M) ranging from M^+ to M^{6+} and their charge balancing mechanism. In case of M^{4+} interstitial, its positively charge could be compensated by O interstitial. Under O-deficiency condition, the O interstitial is possibly annealed by an O vacancy, and the electron polarons become charge compensators. In contrast, M^{4+} substitution could replace both V and its vanadyl O, i.e., vanadyl $(VO)^{3+}$ group, resulting in a net charge of +1, which is balanced by an electron polaron. The binding of polaron with the impurity defect is weaker than that with O vacancy in undoped case, leading to the better mobility of polaron as well as the enhanced electronic conductivity. Based on the calculated energy of formation, the latter case is slightly more favorable in case of Sn^{4+} doping (McColl *et al.*, 2018). It should be noted that the prior case can be more favorable in some condition.

Followed by a density functional theory (DFT) study of Sn-doped V_2O_5 (Suthirakun, Jungthawan, *et al.*, 2018), the Sn interstitial is energetically more favorable than the Sn substitution. Two extra electrons originated from Sn interstitial

are localized as polarons nearby the doping site. The energy barriers of these polarons escaping from the defect region are slightly high, but they are not bound to the defect center, leading to the increase in charge carrier concentration. Thus, Sn doping could enhance electronic conductivity. Although, the scenario of Sn-related defect inducing O vacancy formation has been proposed by the experiment (Z. Y. Li *et al.*, 2016) and the classical model (McColl *et al.*, 2018), it is worth noting that this complex defect has not been studied in the DFT level.

Understanding the formation of point defects might be a knowledge gap to explain the effect of Sn on the improved electrochemical performance of LIBs. Since defect formation could be the source of interlayer expansion, (Z. Y. Li *et al.*, 2016) blocking diffusion path, (Andrews *et al.*, 2018) influencing repulsive coulomb force between Li and dopant, or even being the center of nucleation and growth of phase transition during cycling. (D. M. Yu *et al.*, 2010). For decades, DFT based calculations have emerged as a predictive tool that complements experiments for defect identification (Freysoldt *et al.*, 2014). For instances, previous studies have revealed the insight into fundamental and mechanism of point defect formation in cathode materials, e.g. LiCoO_2 , LiFePO_4 , LiMn_2O_4 and Mg-doped LiCoO_2 , which could be beneficial for designing the cathode (Hoang and Johannes, 2018). Although, this powerful tool (Freysoldt *et al.*, 2014) was utilized to study the formation of point defects in a number of materials, the application on V_2O_5 especially upon Sn impurity has not been reported. The systematically study of point defect formation and charge compensation mechanism could provide more insight into the role of Sn doping on the electrode performance especially conductivity.

1.4 Research objective

The objective of this work is to investigate the role of Sn doping on improving electrode performance of Sn-doped V_2O_5 using DFT+U method coupled with a statistical model. The thermodynamics of point defect formation i.e. native and Sn-related defects was systematically studied using supercell approach. Subsequently, the calculated formation energies were used as input for the statistical model with the constraint of charge neutrality to estimate the defect and carrier concentrations upon Sn doping compared to without doping. Also, the charge transport in both cases was explored. These findings can imply the effect of Sn doping on the electrode performance especially electron conductivity.

1.5 Scope and limitations

As mentioned earlier, the roles of Sn doping on the improved electrode performance were proposed in many ways such as the reduction of nanoparticle size (morphology), the increase in structural stability, and the enlarging of interlayer space. However, this thesis mainly focuses solely on the effect of Sn doping on the improved electronic conductivity. Because the conductivity is strongly correlated to the formation of point defects and compensating charge carriers and their transport behavior which can be explored using the atomistic model calculations based on DFT. Basically, DFT suits for atomic level which is limited by the periodic model of around 200 atoms. To study the mesoscale and more complex phenomena, e.g., morphology of the nanoparticle or structural stability relating to phase transition, one might need other tools rather than DFT. Therefore, the scope of this study is limited on the change in electronic conductivity of the material upon doping with Sn.

For the model of Sn-doped V_2O_5 , three possibilities of Sn-related point defects were considered based on the previous works including i) Sn interstitial, ii) Sn substitutional for V, and iii) Sn substitution for VO. For simplicity, the effect of intercalated Li-ions was not considered, in other words, the study is limited at the initial state of the discharge process of the cathode where there is no Li-ion or it is in the very low concentration. Apart from the formation of Sn-related defects, the compensating defects either native defects or charge carriers were considered in term of defect formation energy. The statistical model was applied to estimate the concentrations of Sn-related defects, native defects, and charge carriers. It should be noted that the input parameters such as oxygen partial pressure and annealing temperature are set as the conventional synthesise condition of Sn-doped V_2O_5 .

Moreover, in this work, all DFT calculations was done by the introduction of Hubbard U parameters so-called DFT+U method. Relying on the assumption that the Hubbard U parameters can resolve the over-delocalization of electrons or the well-known self-interaction error of conventional DFT. The DFT+U approach is commonly used in case of transition metal oxides including V_2O_5 , to alleviate the over-localization error of d-electrons and to better describe the electron behavior inside the materials. However, the value of U parameter has a strong effect on the electron localization, polaron formation and even the transport of electron. Here, the value of U parameter was carefully tuned based on the localization behavior, i.e., the polaronic state of V_2O_5 observed in previous experiment. The tuned U value was used for all DFT+U calculations in this work.

1.6 References

- Andrews, J. L., Mukherjee, A., Yoo, H. D., Parija, A., Marley, P. M., Fakra, S., Prendergast, D., Cabana, J., Klie, R. F. and Banerjee, S. (2018). Reversible Mg-Ion Insertion in a Metastable One-Dimensional Polymorph of V_2O_5 . **Chem.** 4: 564.
- Bruce, P. G., Scrosati, B. and Tarascon, J.-M. (2008). Nanomaterials for Rechargeable Lithium Batteries. **Angew. Chem., Int. Ed.** 47: 2930.
- Bui, K. M., Dinh, V. A. and Ohno, T. (2012). Diffusion Mechanism of Polaron–Li Vacancy Complex in Cathode Material L_2FeSiO_4 . **Appl. Phys. Express.** 5: 125802.
- Byeon, A., Zhao, M.-Q., Ren, C. E., Halim, J., Kota, S., Urbankowski, P., Anasori, B., Barsoum, M. W. and Gogotsi, Y. (2017). Two-Dimensional Titanium Carbide MXene As a Cathode Material for Hybrid Magnesium/Lithium-Ion Batteries. **ACS Appl. Mater. Interfaces.** 9: 4296.
- Carrasco, J. (2014). Role of Van der Waals Forces in Thermodynamics and Kinetics of Layered Transition Metal Oxide Electrodes: Alkali and Alkaline-Earth Ion Insertion into V_2O_5 . **J. Phys. Chem. C.** 118: 19599.
- Chen, C. H., Liu, J., Stoll, M. E., Henriksen, G., Vissers, D. R. and Amine, K. (2004). Aluminum-doped lithium nickel cobalt oxide electrodes for high-power lithium-ion batteries. **J. Power Sources.** 128: 278.
- Cheng, F., Liang, J., Tao, Z. and Chen, J. (2011). Functional Materials for Rechargeable Batteries. **Adv. Mater. (Weinheim, Ger.).** 23: 1695.

- Chernova, N. A., Roppolo, M., Dillon, A. C. and Whittingham, M. S. (2009). Layered Vanadium and Molybdenum Oxides: Batteries and Electrochromics. **J. Mater. Chem.** 19: 2526.
- Dahn, J. R., von Sacken, U. and Michal, C. A. (1990). Structure and electrochemistry of $\text{Li}_{1\pm y}\text{NiO}_2$ and a new Li_2NiO_2 phase with the $\text{Ni}(\text{OH})_2$ structure. **Solid State Ionics.** 44: 87.
- Daniel, C., Mohanty, D., Li, J. and Wood, D. L. (2014). Cathode materials review. **AIP Conf. Proc.** 1597: 26.
- De Jesus, L. R., Horrocks, G. A., Liang, Y., Parija, A., Jaye, C., Wangoh, L., Wang, J., Fischer, D. A., Piper, L. F. J., Prendergast, D. and Banerjee, S. (2016). Mapping Polaronic States and Lithiation Gradients in Individual V_2O_5 Nanowires. **Nat. Commun.** 7: 12022.
- Freysoldt, C., Grabowski, B., Hickel, T., Neugebauer, J., Kresse, G., Janotti, A. and Van de Walle, C. G. (2014). First-Principles Calculations for Point Defects in Solids. **Rev. Mod. Phys.** 86: 253.
- Goodenough, J. B. and Kim, Y. (2010). Challenges for Rechargeable Li Batteries. **Chem. Mater.** 22: 587.
- Hoang, K. and Johannes, M. D. (2018). Defect physics in complex energy materials. **J. Phys.: Condens. Matter.** 30: 293001.
- Hu, X., Zhang, W., Liu, X., Mei, Y. and Huang, Y. (2015). Nanostructured Mo-based electrode materials for electrochemical energy storage. **Chem. Soc. Rev.** 44: 2376.

- Huang, X., Rui, X. H., Hng, H. H. and Yan, Q. Y. (2015). Vanadium Pentoxide-Based Cathode Materials for Lithium-Ion Batteries: Morphology Control, Carbon Hybridization, and Cation Doping. **Part. Part. Syst. Charact.** 32: 276.
- Kerisit, S., Rosso, K. M., Yang, Z. and Liu, J. (2009). Dynamics of Coupled Lithium/Electron Diffusion in TiO_2 Polymorphs. **J. Phys. Chem. C.** 113: 20998.
- Le, S. W., Li, Y. W., Xiao, S. H., Sun, T., Yao, J. H. and Zou, Z. G. (2019). Enhanced reversible lithium storage property of $\text{Sn}_{0.1}\text{V}_2\text{O}_5$ in the voltage window of 1.5-4.0 V. **Solid State Ionics.** 341: 8.
- Legagneur, V., An, Y., Mosbah, A., Portal, R., Le Gal La Salle, A., Verbaere, A., Guyomard, D. and Piffard, Y. (2001). LiMBO_3 (M=Mn, Fe, Co):: synthesis, crystal structure and lithium deinsertion/insertion properties. **Solid State Ionics.** 139: 37.
- Li, M. and Lu, J. (2020). Cobalt in lithium-ion batteries. **Science.** 367: 979.
- Li, W., Lee, S. and Manthiram, A. (2020). High-Nickel NMA: A Cobalt-Free Alternative to NMC and NCA Cathodes for Lithium-Ion Batteries. **Adv. Mater. (Weinheim, Ger.).** 32: 2002718.
- Li, Y. W., Yao, J. H., Uchaker, E., Zhang, M., Tian, J. J., Liu, X. Y. and Cao, G. Z. (2013). Sn-Doped V_2O_5 Film with Enhanced Lithium-Ion Storage Performance. **J. Phys. Chem. C.** 117: 23507.
- Li, Z. Y., Zhang, C. K., Liu, C. F., Fu, H. Y., Nan, X. H., Wang, K., Li, X. Y., Ma, W. D., Lu, X. M. and Cao, G. Z. (2016). Enhanced Electrochemical Properties of Sn-Doped V_2O_5 as a Cathode Material for Lithium Ion Batteries. **Electrochim. Acta.** 222: 1831.

- Liu, F., Song, S., Xue, D. and Zhang, H. (2012). Selective crystallization with preferred lithium-ion storage capability of inorganic materials. **Nanoscale Res. Lett.** 7: 149.
- Liu, X., Zeng, J., Yang, H., Zhou, K. and Pan, D. (2018). V₂O₅-Based Nanomaterials: Synthesis and Their Applications. **RSC Adv.** 8: 4014.
- Lu, J., Chen, Z., Pan, F., Cui, Y. and Amine, K. (2018). High-Performance Anode Materials for Rechargeable Lithium-Ion Batteries. **Electrochemical Energy Reviews.** 1: 35.
- Mai, L., Xu, L., Han, C., Xu, X., Luo, Y., Zhao, S. and Zhao, Y. (2010). Electrospun Ultralong Hierarchical Vanadium Oxide Nanowires with High Performance for Lithium Ion Batteries. **Nano Lett.** 10: 4750.
- Manthiram, A. (2020). A reflection on lithium-ion battery cathode chemistry. **Nat. Commun.** 11: 1550.
- Marley, P. M., Horrocks, G. A., Pelcher, K. E. and Banerjee, S. (2015). Transformers: the changing phases of low-dimensional vanadium oxide bronzes. **Chem. Commun. (Cambridge, U. K.).** 51: 5181.
- Massé, R. C., Liu, C., Li, Y., Mai, L. and Cao, G. (2016). Energy storage through intercalation reactions: electrodes for rechargeable batteries. **National Science Review.** 4: 26.
- Maxisch, T., Zhou, F. and Ceder, G. (2006). Ab initio study of the migration of small polarons in olivine Li_xFePO₄ and their association with lithium ions and vacancies. **Phys. Rev. B.** 73: 104301.

- McColl, K., Johnson, I. and Cora, F. (2018). Thermodynamics and Defect Chemistry of Substitutional and Interstitial Cation Doping in Layered Alpha-V₂O₅. **Phys. Chem. Chem. Phys.** 20: 15002.
- Mizushima, K., Jones, P. C., Wiseman, P. J. and Goodenough, J. B. (1980). Li_xCoO₂ (0<x<1): A new cathode material for batteries of high energy density. **Mater. Res. Bull.** 15: 783.
- Nitta, N., Wu, F., Lee, J. T. and Yushin, G. (2015). Li-ion battery materials: present and future. **Materials Today.** 18: 252.
- Nytén, A., Abouimrane, A., Armand, M., Gustafsson, T. and Thomas, J. O. (2005). Electrochemical performance of Li₂FeSiO₄ as a new Li-battery cathode material. **Electrochem. Commun.** 7: 156.
- Ohzuku, T., Takeda, S. and Iwanaga, M. (1999). Solid-state redox potentials for Li[Me_{1/2}Mn_{3/2}]O₄ (Me: 3d-transition metal) having spinel-framework structures: a series of 5 volt materials for advanced lithium-ion batteries. **J. Power Sources.** 81-82: 90.
- Padhi, A. K., Nanjundaswamy, K. S. and Goodenough, J. B. (1997). Phospho-olivines as Positive-Electrode Materials for Rechargeable Lithium Batteries. **J. Electrochem. Soc.** 144: 1188.
- Parija, A., Liang, Y., Andrews, J. L., De Jesus, L. R., Prendergast, D. and Banerjee, S. (2016). Topochemically De-Intercalated Phases of V₂O₅ as Cathode Materials for Multivalent Intercalation Batteries: A First-Principles Evaluation. **Chem. Mater.** 28: 5611.
- Rajeshwari, S., Kumar, J. S., Rajendrakumar, R. T., Ponpandian, N. and Thangadurai, P. (2018). Influence of Sn ion doping on the photocatalytic performance of

- V₂O₅ nanorods prepared by hydrothermal method. **Mater. Res. Express.** 5: 13.
- Ramesh, T. N., Lee, K. T., Ellis, B. L. and Nazar, L. F. (2010). Favorite Lithium Iron Fluorophosphate Cathode Materials: Phase Transition and Electrochemistry of LiFePO₄F–Li₂FePO₄F. **Electrochem. Solid-State Lett.** 13: A43.
- Scanlon, D. O., Walsh, A., Morgan, B. J. and Watson, G. W. (2008). An ab initio Study of Reduction of V₂O₅ through the Formation of Oxygen Vacancies and Li Intercalation. **J. Phys. Chem. C.** 112: 9903.
- Schmuck, R., Wagner, R., Hörpel, G., Placke, T. and Winter, M. (2018). Performance and cost of materials for lithium-based rechargeable automotive batteries. **Nat. Energy.** 3: 267.
- Sushko, M. L., Rosso, K. M. and Liu, J. (2010). Mechanism of Li⁺/Electron Conductivity in Rutile and Anatase TiO₂ Nanoparticles. **J. Phys. Chem. C.** 114: 20277.
- Suthirakun, S., Genest, A. and Rösch, N. (2018). Modeling Polaron-Coupled Li Cation Diffusion in V₂O₅ Cathode Material. **J. Phys. Chem. C.** 122: 150.
- Suthirakun, S., Jungthawan, S. and Limpijumnong, S. (2018). Effect of Sn-Doping on Behavior of Li-Intercalation in V₂O₅ Cathode Materials of Li-Ion Batteries: A Computational Perspective. **J. Phys. Chem. C.** 122: 5896.
- Thackeray, M. M., David, W. I. F., Bruce, P. G. and Goodenough, J. B. (1983). Lithium insertion into manganese spinels. **Mater. Res. Bull.** 18: 461.
- Thackeray, M. M., Wolverton, C. and Isaacs, E. D. (2012). Electrical energy storage for transportation—approaching the limits of, and going beyond, lithium-ion batteries. **Energy Environ. Sci.** 5: 7854.

- Wang, S., Lu, Z., Wang, D., Li, C., Chen, C. and Yin, Y. (2011). Porous monodisperse V_2O_5 microspheres as cathode materials for lithium-ion batteries. **J. Mater. Chem.** 21: 6365.
- Wattthaisong, P., Jungthawan, S., Hirunsit, P. and Suthirakun, S. (2019). Transport Properties of Electron Small Polarons in a V_2O_5 Cathode of Li-ion Batteries: A Computational Study. **RSC Adv.** 9: 19483.
- Whitfield, P. S., Davidson, I. J., Cranswick, L. M. D., Swainson, I. P. and Stephens, P. W. (2005). Investigation of possible superstructure and cation disorder in the lithium battery cathode material $LiMn_{1/3}Ni_{1/3}Co_{1/3}O_2$ using neutron and anomalous dispersion powder diffraction. **Solid State Ionics.** 176: 463.
- Whittingham, M. S. (1976). Electrical Energy Storage and Intercalation Chemistry. **Science** 192: 1126.
- Whittingham, M. S. (1976). The Role of Ternary Phases in Cathode Reactions. **J. Electrochem. Soc.** 123: 315.
- Whittingham, M. S. (2004). Lithium Batteries and Cathode Materials. **Chem. Rev. (Washington, DC, U. S.).** 104: 4271.
- Wu, H., Chan, G., Choi, J. W., Ryu, I., Yao, Y., McDowell, M. T., Lee, S. W., Jackson, A., Yang, Y., Hu, L. and Cui, Y. (2012). Stable cycling of double-walled silicon nanotube battery anodes through solid–electrolyte interphase control. **Nat. Nanotechnol.** 7: 310.
- Wu, Q. H., Thißen, A. and Jaegermann, W. (2005). Photoelectron Spectroscopic Study of Li Intercalation into V_2O_5 Thin Films. **Surf. Sci.** 578: 203.
- Xing, L., Yu, Q., Bao, Y., Chu, J., Han, K., Chong, S., Lao, C.-Y., Lai, F., Li, P., Xi, K. and Wang, W. (2019). Strong (001) Facet-Induced Growth of Multi-

- Hierarchical Tremella-Like Sn-Doped V_2O_5 for high-performance potassium-ion batteries. **J. Mater. Chem. A.** 7: 25993.
- Xu, B., Qian, D., Wang, Z. and Meng, Y. S. (2012). Recent progress in cathode materials research for advanced lithium ion batteries. **Mater. Sci. Eng. R Rep.** 73: 51.
- Yu, D. M., Zhang, S. T., Liu, D. W., Zhou, X. Y., Xie, S. H., Zhang, Q. F., Liu, Y. Y. and Cao, G. Z. (2010). Effect of manganese doping on Li-ion intercalation properties of V_2O_5 films. **J. Mater. Chem.** 20: 10841.
- Yu, J., Sushko, M. L., Kerisit, S., Rosso, K. M. and Liu, J. (2012). Kinetic Monte Carlo Study of Ambipolar Lithium Ion and Electron–Polaron Diffusion into Nanostructured TiO_2 . **J. Phys. Chem. Lett.** 3: 2076.
- Zhan, S. Y., Wang, C. Z., Nikolowski, K., Ehrenberg, H., Chen, G. and Wei, Y. J. (2009). Electrochemical properties of Cr doped V_2O_5 between 3.8 V and 2.0 V. **Solid State Ionics.** 180: 1198.
- Zhang, C.-f., Yang, P., Dai, X., Xiong, X., Zhan, J. and Zhang, Y.-l. (2009). Synthesis of $LiNi_{1/3}Co_{1/3}Mn_{1/3}O_2$ cathode material via oxalate precursor. **Transactions of Nonferrous Metals Society of China.** 19: 635.
- Zhang, H., Yu, X. and Braun, P. V. (2011). Three-dimensional bicontinuous ultrafast-charge and -discharge bulk battery electrodes. **Nat. Nanotechnol.** 6: 277.
- Zhang, Z., Shao, C., Zhang, L., Li, X. and Liu, Y. (2010). Electrospun nanofibers of V-doped TiO_2 with high photocatalytic activity. **J. Colloid Interface Sci.** 351: 57.

Zhu, Y., Yang, M., Huang, Q., Wang, D., Yu, R., Wang, J., Zheng, Z. and Wang, D.
(2020). V_2O_5 Textile Cathodes with High Capacity and Stability for Flexible
Lithium-Ion Batteries. **Adv. Mater. (Weinheim, Ger.)**. 32: 1906205.



CHAPTER II

ATOMISTIC MODELING

In material science community, the atomistic modeling has been found to be a powerful tool to provide a fundamental description of the material properties and phenomena. These properties of materials such as electronic, optical, and magnetic characters are significantly dominated by the behaviors on electrons inside the materials, which can be described Schrödinger equation. Density functional theory (DFT) is proven to be a successful quantum mechanics approach to model the material properties. In fact, DFT is now widespread all areas of condensed matter physics and quantum chemistry. This also includes the study of formation of point defects and carriers transport which is the focus of this work. The purpose of this chapter is to present an introduction into density functional theory and related concepts, which mostly relies on this book (Sholl and Steckel, 2011).

2.1 Many-body Schrodinger equation

To calculate the properties of a collection of atoms such as an isolated molecule or a crystalline solid, this system can be treated as a set of nuclei and their corresponding electrons, in which the behaviors of particles in the system derived from the Schrodinger equation. The simple form so-called the time independent and nonrelativistic Schrodinger equation is $\hat{H}\psi_i = E_i\psi_i$. The \hat{H} is the Hamiltonian operator describing the interaction of the system. While ψ_i ,

and E_i are eigen-wavefunction and associated eigen-energy of the system, corresponding to the solution i of the eigen-equation.

The expression of the Hamiltonian operator relies on the physical system. In some cases, e.g., the particle in a box and a harmonic oscillator, their Hamiltonian operators are in a simple form, and can be solved analytically. However, in case of the system being considered is more complicated due to the interaction between multiple electrons and nuclei. For the system consist of M nuclei and N electrons, the Hamiltonian \hat{H} can be written as,

$$\hat{H} = -\frac{1}{2} \sum_{I=1}^M \frac{1}{M_I} \nabla_I^2 - \frac{1}{2} \sum_{i=1}^N \nabla_i^2 + \sum_{I=1}^M \sum_{J>I}^M \frac{Z_I Z_J}{R_{IJ}} + \sum_{i=1}^N \sum_{i>j}^N \frac{1}{r_{ij}} - \sum_{i=1}^N \sum_{I>1}^M \frac{Z_I}{r_{iI}}$$

$$\hat{H} = T_n + T_e + V_{nn} + V_{ee} + V_{ne} \quad (2.1)$$

where i and j are the indices of electrons whereas I and J are those of nuclei. M_I and Z_I are the mass and charge of nuclei. Either R_{xx} or r_{xx} represents the distances between to particles. It should be noted that the above equation is written in atomic unit for simplicity. The first two terms are the kinetic energies of nuclei and electrons. The rest three terms are the coulomb interactions between nucleus-nucleus, electron-electron, and nucleus-electron, respectively.

Since atomic nuclei are much heavier than individual electrons. In fact, the mass of either a proton or a neutron in a nucleus is more than 1800 times that of an electron. Roughly, the nuclei move so slowly compared to the speed electron movement. So that, the first term (kinetic energy of nuclei) is zero. In addition, the third term (interaction between nucleus-nucleus) can be separately solved from the total Hamiltonian as classical, and the energy relating to this term remains almost constant. So, the

complexity of system is slightly reduced by considering the three remaining terms of Hamiltonian, e.g.,

$$\hat{H}_e = T_e + V_{ee} + V_{ne} \quad (2.2)$$

Then, only Hamiltonian for electron contribution was solved with fixed positions of the atomic nuclei. This separation of nuclei and electrons into two contributions is called the Born–Oppenheimer approximation (Born and Oppenheimer, 1927; Cederbaum, 2008).

For a particular system, the dimension of the full wavefunction rapidly increases as N , the number of electrons. For example, if a single molecule of O_2 is considered, the full wavefunction is a 48-dimensional function (3 dimensions for each of the 16 electrons). The dimension can be up to 23,000 dimensions, if a nanocluster of 100 Pt atoms is considered. In the Hamiltonian, the coulomb interaction term between electron-electron reveals that the electronic motion is correlated. This means the individual wavefunction cannot be solved without simultaneously considering all the other electrons. Finding the exact solutions of the systems is very difficult or impossible even in the case of moderate N . This problem is also known as a many-body Schrodinger equation.

2.2 Density functional theory (DFT)

To solve the many-body problem, several approximations have been proposed to simplify the complexity of problem. Let us consider the ground state electronic wavefunction, the wavefunction should be a function of spatial coordinates of N electrons, i.e., $\psi_0 = \psi(r_1, r_2, \dots, r_N)$. The earliest approximation was proposed by Hartree (Hartree, 1928). The total wavefunction ψ_0 possibly approximates as a product

of individual electron wave functions, $\psi_0 = \psi_1(r_1) \cdot \psi_2(r_2) \cdot \dots \cdot \psi_N(r_N)$. This is known as Hartree product where it breaks the full wavefunction of N-interacting electrons into a product of N non-interacting wavefunctions. However, this electron wavefunction does not satisfy the anti-symmetric property of the Fermions which follow Pauli exclusion principle. The more appropriate trial wavefunction should be written in the Slater determinant format (Slater, 1930) as following,

$$\psi_0 = \frac{1}{\sqrt{N!}} \begin{vmatrix} \psi_1(r_1) & \psi_2(r_1) & \cdots & \psi_N(r_1) \\ \psi_1(r_2) & \psi_2(r_2) & \cdots & \psi_N(r_2) \\ \vdots & \vdots & \ddots & \vdots \\ \psi_1(r_N) & \psi_2(r_N) & \cdots & \psi_N(r_N) \end{vmatrix} \quad (2.3)$$

This approximated wavefunction is known as Hartree-Fock, ψ_{HF} . Substituting ψ_{HF} in expectation value of Hamiltonian in order to find the total energy, in turns, generates a new term called exchange term, satisfying the anti-symmetric property (Fock, 1930). Nevertheless, the Hartree-Fock method does not take into account the correlation of interacting between electron-electron.

Instead of using full electron wavefunction, the quantity so-called electron density distribution $n(r)$ is used to describe the system, which is the key concept of density functional theory. One example of the advantages of using electron density is that it compresses the information of full wavefunction, which is a function of $3N$ coordinates, into the electron density $n(r)$, which is a function of only three coordinates. As a result, the complexity of the system is significantly decreased especially the moderate or large system. The density functional theory relies on the mathematical theorem from Hohenberg and Kohn (Hohenberg and Kohn, 1964) and a set of equations derived by Kohn and Sham (Kohn and Sham, 1965).

Let us begin with the Hohenberg-Kohn theorems. The first one states that the ground state electron density $n(r)$ for any electronic system uniquely determines that system. In other words, all ground state properties can be expressed in term of the ground state electron density $n(r)$, including the total electronic energy, kinetic energy, or even the potential energy. Notably, the summation over all electrons number in each energy terms in the Hamiltonian becomes the integration over all electron density $n(r)$. The second theorem also states that the electron density $n(r)$ that minimizes the energy of the overall functional is the ground state electron density. If the functional form were known, then the electron density could be varied until the energy from the functional is minimized, giving us the electron density.

Unfortunately, the true form of the overall energy functional $E[n(r)]$ is still unclear. Based on Kohn and Sham method, they divide the functional into known and unknown energy functionals. The kinetic energy functional is separated into the known term corresponding to non-interacting electrons, $T_{non}[n(r)]$ and the unknown term corresponding to electron-electron correlation, $T_{corr}[n(r)]$. Likewise, the potential energy functional is divided into three terms. The first two known terms $E_{Ne}[n(r)]$ and $E_{ee}[n(r)]$ are coulomb interaction between the non-interacting electrons and nuclei and between pairs of non-interacting electrons, respectively. The last term is unknown which includes all unknown and quantum effect such as exchange and correlation of electrons. All unknown terms are combined as the exchange-correlation functional denoted as $E_{xc}[n(r)]$. Therefore, the overall energy functional $E[n(r)]$ can be written as

$$E[n(r)] = T_{\text{non}}[n(r)] + E_{Ne}[n(r)] + E_{ee}[n(r)] + E_{xc}[n(r)] \quad (2.4)$$

$$E[n(r)] = T_{\text{non}}[n(r)] + \int n(r)V_{Ne}dr + \frac{1}{2} \int \int \frac{n(r)n(r')}{|r-r'|} dr dr' + E_{xc}[n(r)]. \quad (2.5)$$

The difficulty of the fully solving the many-body Schrodinger equation was solved by Kohn and Sham. They showed that the task of finding the electron density can be done by solving a set of equations, in which each equation considers only a single electron.

The Schrodinger-like equations so-called Kohn–Sham equations can be expressed as

$$\left[-\frac{\nabla^2}{2} + V_H[n(r)] + V_{ext}[n(r)] + V_{xc}[n(r)] \right] \psi_i^{KS}(r) = E_i \psi_i^{KS}(r), \quad (2.6)$$

$$\left[-\frac{\nabla^2}{2} + \frac{1}{2} \int \frac{n(r')}{|r-r'|} dr' - \sum_{I=1}^M \int \frac{Z_I}{|R_I-r|} dr + V_{xc}[n(r)] \right] \psi_i^{KS}(r) = E_i \psi_i^{KS}(r). \quad (2.7)$$

$\psi_i^{KS}(r)$ is the Kohn-Sham orbital of the electron number in band index i , and E_i is corresponding electron energy. The first term in Hamiltonian is basically kinetic energy operator of the single electron being considered. The second term is called Hartree potential describing the Coulomb repulsion between the single electron and the total electron density. The third term is called external potential describing the Coulomb attraction between the single electron and nuclei. For the last term, $V_{xc}[n(r)]$ is the exchange-correlation potential which can be expressed as a functional derivative by

$$V_{xc}[n(r)] = \frac{\delta E_{xc}[n(r)]}{\delta n} \quad (2.8)$$

To solve the Kohn–Sham equations, the second Hohenberg-Kohn theorem was employed. The problem is usually treated in an iterative way so-called the self-consistent field (SCF) method as shown in Figure 2.1.

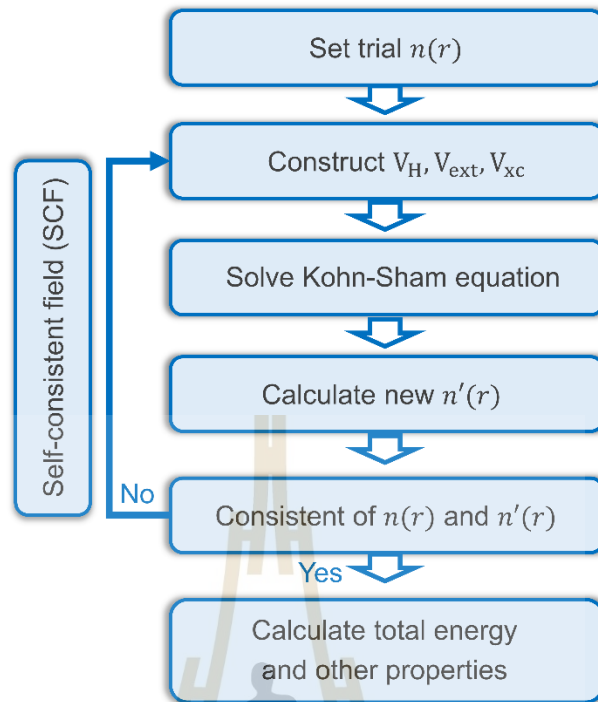


Figure 2.1 The scheme of self-consistent field (SCF) iterations for solving the Kohn-Sham equations and obtaining calculate total energy and other properties.

The procedure of self-consistent field is outlined as following:

- I) Set an initial trial electron density $n(r)$.
- II) Construct the Hartree, external, and exchange-correlation potential based on the electron density.
- III) Solve the Kohn-Sham equations to find single electron wavefunctions ψ_i .
- IV) Calculate new electron density from the calculated wavefunctions.
- V) Compare new electron density with the one in previous iteration. If the two densities are the same, then the obtained electron density is the ground state electron density of the system. If the two densities are different, the mixing of them will be used as the next trial electron density and sent back to step II) until being self-consistent.

As ground state electron density represents the characteristic of the system being considered, this density can be further used to calculate the ground state energy and force acting on each atom. Also, other material properties can be calculated from the (or a set of) calculated ground state electron density or energy.

2.3 The exchange-correlation functional

According to the second Hohenberg-Kohn theorem, the more accurate results can be acquired if the exact form of overall functional was known. As mentioned earlier, the exchange-correlation functional $E_{xc}[n(r)]$ is a collection of unknown terms such as the quantum effect of exchange and correlation between electrons. However, the exchange-correlation functional of the homogeneous electron gas system can be solved analytically. This simplest form is approximated to use in the inhomogeneous system as

$$E_{xc}^{LDA}[n(r)] = \int n(r)\epsilon_{xc}[n(r)]dr \quad (2.9)$$

where $\epsilon_{xc}[n(r)]$ is the exchange-correlation electron density of a uniform gas. This is the idea of local density approximation (LDA) where the functional depends only on the electron density $n(r)$ at the position being considered. Due to the inhomogeneous behavior of the real system, the gradient of electron density should be included to improve the approximation. This is called the generalized gradient approximation (GGA) as

$$E_{xc}^{GGA}[n(r)] = \int n(r)\epsilon_{xc}[n(r), \nabla n(r)]dr. \quad (2.10)$$

In fact, there are various forms of GGA functionals which are differed by the mathematical term of $\epsilon_{xc}[n(r), \nabla n(r)]$. Two of the most widely used functionals in calculations of crystalline solid are the Perdew–Burke–Ernzerhof functional (PBE) and the Perdew–Wang functional (PW91).

2.4 DFT+U approach

According to the ground state energy calculated from equation 2.5, the third term contributed from the interaction between electrons (Hartree term) also include the interaction between the electron and itself, leading to the so-called self-interacting error. In the Hartree-Fock method the self-interaction was cancelled out with the term from exchanged term. However, the standard DFT with an approximated exchange-correlation functional cannot remove the self-interaction properly, and it cause the overestimation of electron-electron repulsion resulting in the over-delocalization. As a result, the standard DFT might fail to predict some properties of strongly correlated materials including transition metal oxides with the presence of d or f electrons. For instances, it is unsuccessful for predicting the electron localization behavior because of the over-delocalized valence electrons.

From this problem, DFT+U method is formulated to improve the description of the ground state energy of the strongly correlated materials. The concept of solving this problem is adding Hartree-Fock like formalism at the interactions of electrons localization on the same atomic centers which is called as an on-site interaction. In addition, another term relating to double counting is also introduced to correct the energy contribution. Within DFT+U method, the ground state energy of a particular system can be expressed as (Himmetoglu *et al.*, 2014),

$$E^{DFT+U}[n(r), n_{ilm\sigma}] = E^{DFT}[n(r)] + E^{on-site}[n_{ilm\sigma}] - E^{dc}[n_{ilm\sigma}], \quad (2.11)$$

where E^{DFT} is the convention energy of the system from the electron density $n(r)$, $E^{on-site}$ is the energy contribution from the Hartree-Fock like term due to the on-site interaction of localized electrons occupied in atom I with angular momentum l , magnetic moment m and spin σ . The term E^{dc} is for the correcting of double counting from the added on-site energy $E^{on-site}$. In this thesis, the Dudarev's approach (Dudarev *et al.*, 1998) with the rotationally invariant formalism was used to describe $E^{on-site}$ and E^{dc} in the on-site interaction energy. In practice, the on-site interaction strength is involved by two parameters including the on-site Coulomb term U and the site exchange term J . Thus, the correctness of DFT+ U method depends strongly on the value of U and J parameters for describing each system. One need to be carefully select the value of these parameters.

2.5 Wavefunction and pseudopotential

In the previous section, the density functional theory that approximates many-body Schrodinger equation was introduced. One might wonder about the form of the electron wavefunction or Kohn-Sham of the electron which is not stated in the Hohenberg-Kohn theorem and the Kohn-Sham equation. Indeed, the Kohn-Sham orbitals might be very complex or even impossible to express in exact function. In practical, the Kohn-Sham orbitals are, therefore, written in the form of Taylor expansion. The basis set can be localized atomic orbitals, Gaussian functions, or planewaves depending on the system being considered. Just in case of the crystalline solid, the system composes of well-aligned atoms, and the electrons are interacted with the periodic potential. So that, the planewaves with periodicity is an appropriated basis

set to represent the periodic behavior of Kohn-Sham orbitals. The plane wave is written in term of wave vector k in the reciprocal space. The number of basis set using in the expansion is limited by the term cut-off energy. In addition, Bloch theorem can be applied to this periodic system which can reduce a number of atoms in the crystal into considering the atoms in a unit cell. This concept dramatically reduces the required computational resources of solving the Kohn-Sham equations.

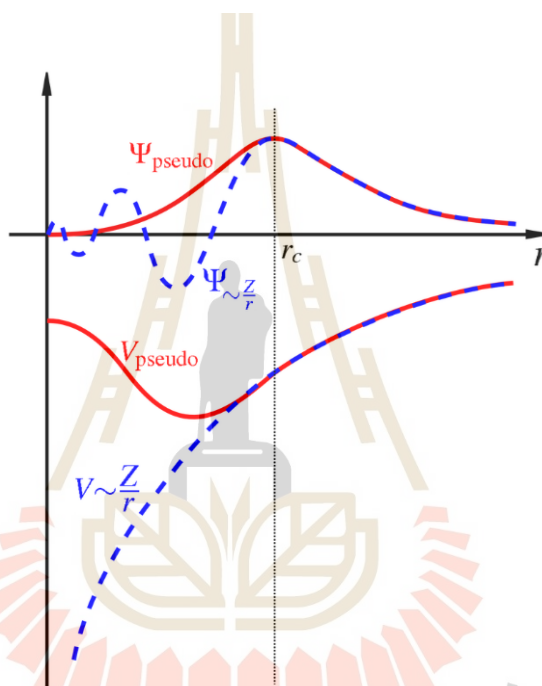


Figure 2.2 Comparison of an all-electron wavefunction in Coulomb potential (blue dashed line) and a pseudo-wavefunction in pseudopotential (red line). The r_c represents the cutoff radius where all-electron and pseudo wavefunction and potential are the same (Payne *et al.*, 1992).

The introduction of pseudopotential is another concept that can speed-up the calculations. Although all electrons in the atoms are indistinguishable, the reactivity or importance of the electrons highly depend on their energy level. In general molecules and crystalline solid, the valence electrons strongly influence materials properties and

phenomena such as chemical bonding, electron transport, light absorption, etc. Whereas the contribution of core electrons is negligible due to the screening effect. This leads us to the concept of pseudopotential where the core electrons, i.e. inside cutoff radius (r_c), are fixed and combined with the nucleus. The pseudopotential and the corresponding wavefunction compared to all-electron ones are illustrated in Figure 2.2. From the graph, the pseudopotential resolves the singularity of the all-electron potential around the nucleus. In addition, the introduced pseudo-wavefunction also adjusts high oscillation of all-electron wavefunction near the core. As a result, the wavefunction can be expanded using a smaller number of planewave, which could also reduce the computational resources. To emphasize, the introduction of pseudopotential is an effective concept to speed-up the calculations based on the frozen-core electrons approximation not only decrease the number of considering electrons i.e. valence electrons, but also smaller the basis set using for representative of the Kohn-Sham orbitals. In this work, the projector-augmented wave (PAW) method was used, and more details about how to construct any pseudopotential are written in literature (Blöchl, 1994; Kresse and Joubert, 1999).

2.6 Summary of computational details

All calculations were carried out using the spin-polarized density functional theory (DFT) as implemented in Vienna *Ab initio* Simulation Package (VASP) (Kresse and Furthmüller, 1996a, 1996b; Kresse and Hafner, 1993). The projector augmented-wave method was employed to construct pseudopotential describing the interaction of frozen-core and valence electrons (Blöchl, 1994; Kresse and Joubert, 1999). The valence electron wavefunctions of V $3s^23p^63d^34s^2$, O $2s^22p^4$ and Sn $4d^{10}5s^25p^2$ were

expanded in plane wave basis with a cut-off energy of 500 eV. The exchange-correlation functional was approximated by the modified Perdew-Burke-Ernzerhof (PBE) approach called optPBE-vdW which included van der Waals interaction (Klimeš *et al.*, 2009, 2011; Perdew *et al.*, 1996). This implementation has been proposed to be an efficient and accurate dispersion interaction for correcting the error in determining the interlayer spacing and behavior of ion intercalation in V_2O_5 (Carrasco, 2014). The U parameter was applied to account for spurious self-interaction error occurred upon using conventional DFT when treating the highly correlated electron materials such as V_2O_5 (Dudarev *et al.*, 1998; Scanlon *et al.*, 2008). In particular, the charge localization upon the creation of native defect is the main behavior in this thesis. Therefore, the U value of V-3d electrons was carefully tuned (3.5 eV) to reproduce the localization behavior of extra electrons obtained from UPS (Wu *et al.*, 2005) as detailed in Appendix A. The Gaussian smearing method ($\sigma = 0.05$ eV) was used with the self-consistent field convergence criteria of 10^{-6} eV.

The 1x3x3 supercell of orthorhombic V_2O_5 (18 formula units or $V_{36}O_{90}$) the most stable phase, with periodic boundary condition was used as the model for all calculations. This supercell size is sufficiently large to reach the convergence of oxygen vacancy formation energy (Scanlon *et al.*, 2008) and to accommodate lattice distortion of the polaron (Suthirakun *et al.*, 2018). The Brillouin zone integration was adopted by 2x2x2 k -mesh sampling using Monkhorst-Pack scheme (Monkhorst and Pack, 1976). To obtain the optimized structure of pristine and defective supercell, all atoms were allowed to relax for minimizing the Hellmann-Feynman force acting on each atom until the forces are less than 0.02 eV/Å.

2.7 References

- Blöchl, P. E. (1994). Projector Augmented-Wave Method. **Phys. Rev. B.** 50: 17953.
- Born, M. and Oppenheimer, R. (1927). Zur Quantentheorie der Molekeln. **Annalen der Physik.** 389: 457.
- Carrasco, J. (2014). Role of Van der Waals Forces in Thermodynamics and Kinetics of Layered Transition Metal Oxide Electrodes: Alkali and Alkaline-Earth Ion Insertion into V_2O_5 . **J. Phys. Chem. C.** 118: 19599.
- Cederbaum, L. S. (2008). Born–Oppenheimer approximation and beyond for time-dependent electronic processes. **J. Chem. Phys.** 128: 124101.
- Dudarev, S. L., Botton, G. A., Savrasov, S. Y., Humphreys, C. J. and Sutton, A. P. (1998). Electron-Energy-Loss Spectra and the Structural Stability of Nickel Oxide: An LSDA+U Study. **Phys. Rev. B.** 57: 1505.
- Fock, V. (1930). Näherungsmethode zur Lösung des quantenmechanischen Mehrkörperproblems. **Zeitschrift für Physik.** 61: 126.
- Hartree, D. R. (1928). The Wave Mechanics of an Atom with a Non-Coulomb Central Field. Part I. Theory and Methods. **Mathematical Proceedings of the Cambridge Philosophical Society.** 24: 89.
- Himmetoglu, B., Floris, A., de Gironcoli, S. and Cococcioni, M. (2014). Hubbard-corrected DFT energy functionals: The LDA+U description of correlated systems. **Int. J. Quantum Chem.** 114: 14.
- Hohenberg, P. and Kohn, W. (1964). Inhomogeneous Electron Gas. **Physical Review.** 136: B864.
- Klimeš, J., Bowler, D. R. and Michaelides, A. (2009). Chemical Accuracy for the Van der Waals Density Functional. **J. Phys.: Condens. Matter.** 22: 022201.

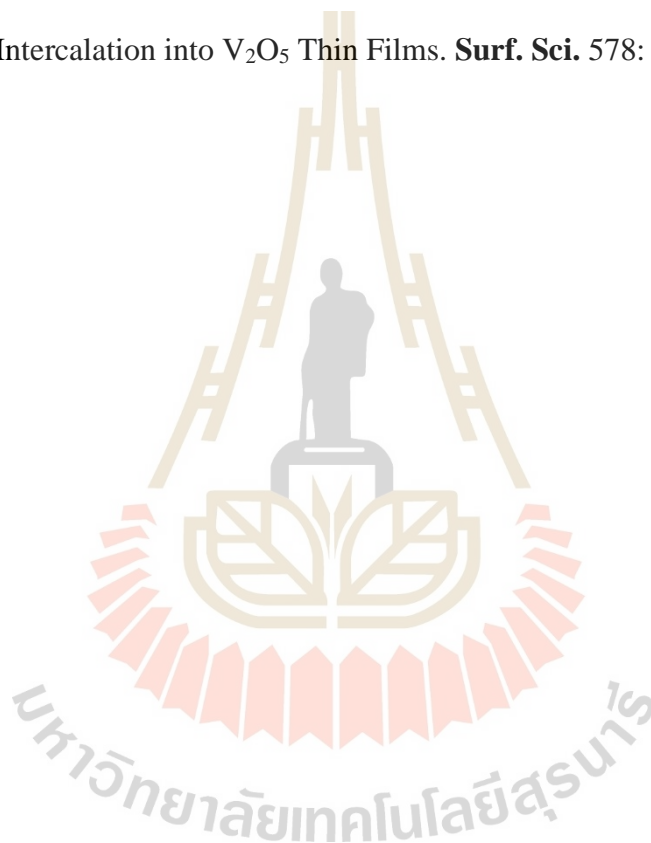
- Klimeš, J., Bowler, D. R. and Michaelides, A. (2011). Van der Waals Density Functionals Applied to Solids. **Phys. Rev. B.** 83: 195131.
- Kohn, W. and Sham, L. J. (1965). Self-Consistent Equations Including Exchange and Correlation Effects. **Physical Review.** 140: A1133.
- Kresse, G. and Furthmüller, J. (1996a). Efficiency of ab-initio Total Energy Calculations for Metals and Semiconductors Using a Plane-Wave Basis Set. **Comput. Mater. Sci.** 6: 15.
- Kresse, G. and Furthmüller, J. (1996b). Efficient Iterative Schemes for ab initio Total-Energy Calculations Using a Plane-Wave Basis Set. **Phys. Rev. B.** 54: 11169.
- Kresse, G. and Hafner, J. (1993). Ab initio Molecular Dynamics for Liquid Metals. **Phys. Rev. B.** 47: 558.
- Kresse, G. and Joubert, D. (1999). From Ultrasoft Pseudopotentials to the Projector Augmented-Wave Method. **Phys. Rev. B.** 59: 1758.
- Monkhorst, H. J. and Pack, J. D. (1976). Special Points for Brillouin-Zone Integrations. **Phys. Rev. B.** 13: 5188.
- Payne, M. C., Teter, M. P., Allan, D. C., Arias, T. A. and Joannopoulos, J. D. (1992). Iterative minimization techniques for ab initio total-energy calculations: molecular dynamics and conjugate gradients. **Rev. Mod. Phys.** 64: 1045.
- Perdew, J. P., Burke, K. and Ernzerhof, M. (1996). Generalized Gradient Approximation Made Simple. **Phys. Rev. Lett.** 77: 3865.
- Scanlon, D. O., Walsh, A., Morgan, B. J. and Watson, G. W. (2008). An ab initio Study of Reduction of V_2O_5 through the Formation of Oxygen Vacancies and Li Intercalation. **J. Phys. Chem. C.** 112: 9903.

Sholl, D. and Steckel, J. A. (2011). *Density Functional Theory: A Practical Introduction*: Wiley.

Slater, J. C. (1930). Note on Hartree's Method. **Physical Review**. 35: 210.

Suthirakun, S., Genest, A. and Rösch, N. (2018). Modeling Polaron-Coupled Li Cation Diffusion in V_2O_5 Cathode Material. **J. Phys. Chem. C**. 122: 150.

Wu, Q. H., Thißen, A. and Jaegermann, W. (2005). Photoelectron Spectroscopic Study of Li Intercalation into V_2O_5 Thin Films. **Surf. Sci**. 578: 203.



CHAPTER III

FORMATION OF INDIVIDUAL POINT DEFECT

3.1 Introduction

The recent experimental works proposed that Sn doping can generate extra charge carriers, i.e., electron polarons, leading to the improved electrochemical performance of V_2O_5 cathode. In fact, these carriers could be originated from the charge balancing mechanism of Sn-related defects or defect complexes. The fundamental knowledge about formation of point defects and compensating charge carriers could be a key information to better understand the role of Sn doping on the improved electronic conductivity. Therefore, in this chapter, the geometric, electronic, and thermodynamic properties of each individual point defects were studied in a systematic manner. The detailed computational method to construct the defects and to calculate their formation energies are described in section 3.2. Before considering the point defects in the material, the crystal structure and electronic structure of orthorhombic V_2O_5 are briefly explained in section 3.3. In section 3.4, the intrinsic defects were constructed, and the geometry and defect formation energy were systematically studied. Likewise, the Sn-related point defects originated from the Sn doping in V_2O_5 also elaborated in section 3.5.

3.2 Computational method for studying point defects

3.2.1 Construction of defective models

To construct the model of an individual defect, the supercell approach was used where a particular point defect was introduced into a 1x3x3 supercell of V₂O₅ (Freysoldt *et al.*, 2014). For example, in case of Sn substitution for V, a V atom was replaced by the Sn atom. Subsequently, all atoms in the defective supercell were allowed to relax until the maximum force acting on each atom is less than 0.02 eV/Å. Similarly, oxygen vacancy was constructed by removing an O atom. The sufficiently large supercell was used to minimize the interaction between the defect and itself from neighbor periodic images, resulting in the model of the isolated point defect. All lattice parameters of the supercell were fixed during the relaxation because doping at diluted limit should not have much effect on the lattice parameters. As a result, the crystal structure and electronic ground state energy of each defective system were obtained. This energy was used to further calculate the defect formation energy as explained in the next section. In addition, it is possible that defects can exchange electrons with the reservoir resulting in charged defects where their relative stabilities are of interest for studying donor/acceptor behavior. The charged defects can be constructed by changing the total number of electrons in the system.

3.2.2 Defect formation energy

The stability of neutral and charged point defects were considered in term of defect formation energies. The formation energy of a given point defect X in charge state q can be expressed by (Freysoldt *et al.*, 2014; Zhang and Northrup, 1991)

$$E^f(X^q, E_F) = E_{tot}(X^q) - E_{tot}(bulk) - \sum_i n_i \mu_i + q(E_{vbm} + E_F) + E_{corr}. \quad (3.1)$$

When $E_{tot}(X^q)$ and $E_{tot}(bulk)$ are the electronic energy of a defective and defect-free supercell, respectively. The integer n_i is the number of elemental specie i , either added ($n_i > 0$) or removed ($n_i < 0$) compared to defect-free supercell. The μ_i represents chemical potential of elemental specie i associated with the required energy for exchanging the element to the reservoir. The detailed calculations of chemical potential of each elemental species, corresponding to experimental condition, are explained in next section. In case of charged defect, the formation energy also depends on chemical potential of electron (Fermi energy) in the material, i.e., $E_{vbm} + E_F$. The last term, E_{corr} , is the electrostatic energy correction due to an artifact in finite-size supercell. In fact, the adapted Makov-Payne correction (Murphy and Hine, 2013) was employed due to the anisotropic dielectricity as often used in other quasi-2D materials e.g. CeO₂ (Shi *et al.*, 2016) and MoO₃ (Lambert *et al.*, 2017).

3.2.3 Chemical potentials

As the defect formation energy depends on the chemical potentials of constituent elements, i.e., μ_V , μ_O , and μ_{Sn} . The set of chemical potentials was carefully defined based on synthesis condition of V₂O₅. In fact, μ_V and μ_O are not independent under thermodynamic equilibrium, as constrained by

$$2\mu_V(T, p) + 5\mu_O(T, p) = \mu_{V_2O_5}(T, p) \approx E_{tot}(V_2O_5). \quad (3.2)$$

When p and T are O₂ partial pressure and annealing temperature corresponding to the synthesis condition. The $\mu_{V_2O_5}$ is basically Gibbs free energy of V₂O₅, which can be approximated to be the electronic energy, $E_{tot}(V_2O_5)$ because the energy contributions from zero-point vibration and entropy can be ignored for solids.

To avoid the formation of secondary phase, it is necessary to consider the upper and lower limit of $\mu_O(T, p)$. In fact, when $\mu_O(T, p)$ is lower than a specific value, the V_2O_5 could be reduced to a lower-valence oxide i.e. VO_2 . Specifically, this is called the O-poor limit which can be defined as,

$$\mu_O^{O-poor}(T, p) = E_{tot}(V_2O_5) - 2E_{tot}(VO_2). \quad (3.3)$$

Here, $E_{tot}(VO_2)$ is electronic energy of VO_2 . As a result, the calculated μ_O^{O-poor} of -3.41 eV was obtained, in which this value is independent on the synthesis parameters.

On the contrary, $\mu_O(T, p)$ is higher than a specific point or at high pressures, the oxygen gas molecules possibly be condensed on the surface. This maximum of $\mu_O(T, p)$ is called O-rich condition which is limited by

$$\mu_O^{O-rich}(T, p) = \frac{1}{2}\mu_{O_2}(T, p) \leq \frac{1}{2}(E_{tot}(O_2) + E_{ZPE}(O_2)), \quad (3.4)$$

when $\mu_{O_2}(T, p)$ is the chemical potential of O_2 molecule depending on the reaction condition, and $E_{ZPE}(O_2)$ is zero-point vibration energy of O_2 . Since the calculated $E_{tot}(O_2)$ has a significant error from the well-known over binding energy of O_2 molecule, it was calculated indirectly as the experimental binding energy of 5.23 eV subtracted by two times of energy of isolated oxygen atom (Lee and Han, 2013; L. Wang *et al.*, 2006). As a result, the calculated $E_{tot}(O_2)$ is -4.78 eV. Notice that the reduction enthalpy of V_2O_5 to VO_2 is improved when using this method (-1.02 eV and -0.40 eV for with and without correction compared to the experimental data of -1.28 eV) (Lutfalla *et al.*, 2011). With the calculated $E_{ZPE}(O_2)$ of 0.096 eV, the calculated μ_O^{O-rich} is dependent on the O_2 partial pressure and annealing temperature, but no

greater than -2.34 eV ($E_{tot}(O_2) + E_{ZPE}(O_2)$). In particular, the $\mu_{O_2}(T, p)$ at a given reaction condition can be calculated by,

$$\begin{aligned}\mu_{O_2}(T, p) &= E_{tot}(O_2) + E_{ZPE}(O_2) - TS + k_B T \ln p \\ \mu_{O_2}(T, p) &= E_{tot}(O_2) + E_{ZPE}(O_2) - k_B T \ln Q + k_B T \ln p.\end{aligned}\quad (3.5)$$

Here, total partition function Q is the multiplication of translational, rotational, and vibrational partition function at temperature T which can be calculated using the TURBOMOLE code and TmoleX User Interface (Steffen *et al.*, 2010). The k_B is Boltzmann's constant.

In general, the defect formation energy calculations are carried out for the chemical potential ranging between O-rich and O-poor limits which corresponds to the reaction condition. Figure 3.1 shows the assessable chemical potential range of O (μ_O) for V_2O_5 single phase synthesis under different O_2 partial pressure and temperature. The secondary phase VO_2 can be formed in case μ_O beyond O-poor limit as highlighted in gray area. Likewise, the O_2 deposition can be occurred when μ_O is greater than O-rich limit as highlighted in blue area which also depending on the O_2 pressure. The O-rich limit approaches the maximum value when synthesis under very extreme condition near absolute zero temperature and/or high O_2 pressure.

In practical, the synthesis of Sn-doped V_2O_5 often did under atmospheric pressure (O_2 partial pressure = 0.21 atm) and annealing temperature ranging from 350-450 °C as reported in previous experiments (Y. W. Li *et al.*, 2013; Z. Y. Li *et al.*, 2016; Xing *et al.*, 2019). The range μ_O of the synthesis under atmospheric pressure and annealing temperature of 350 °C (623 K) and 450 °C (723 K) are illustrated as blue and yellow arrows, respectively. Notice that these range of

μ_{O} corresponding to the experimental conditions are considerably narrow. For instances, μ_{O} can be varied for 0.35 eV (from -3.41 to -3.06 eV) or for 0.23 eV (from -3.41 to -3.18) at 350 and 450 °C. Due to this narrow range, defining the chemical potential (μ_{O}) whichever value inside this range does not affect the energetics of point defect formation in conventional synthesis of Sn-doped V_2O_5 corresponding to aforementioned experiments. To simplify, the μ_{O} of -3.18 eV was selected to be a representative condition for most sections in this thesis.

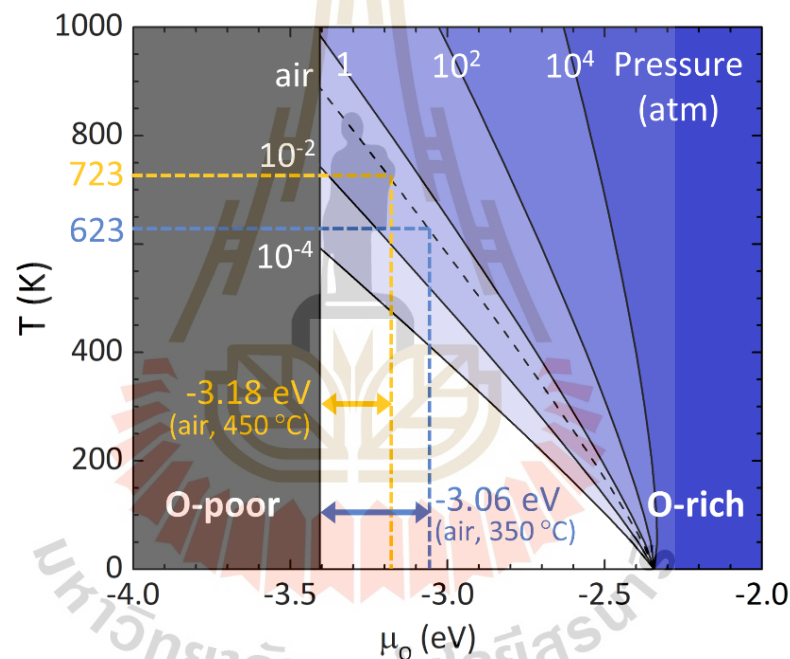


Figure 3.1 The assessable range of chemical potential of O (μ_{O}) for V_2O_5 single phase synthesis. The range is limited by O-poor condition (gray region) at $\mu_{\text{O}} = -3.41$ eV and O-rich condition (blue region) which is altered under different growth condition i.e. annealing temperature and oxygen partial pressure. The blue and yellow dashed lines also show the O-rich limit under air with annealing temperature of 350 and 450 °C, respectively.

In case of Sn impurities, the chemical potential of Sn, μ_{Sn} , is in equilibrium with the Sn sources including Sn-metallic, SnO, and SnO₂. The chemical potential of Sn is always minimized among the sources, i.e.,

$$\mu_{Sn} = \min(E(Sn) , E(SnO) - \mu_O , E(SnO_2) - 2\mu_O). \quad (3.6)$$

When $E(Sn)$, $E(SnO)$, and $E(SnO_2)$ are the electronic energies of Sn, SnO, and SnO₂. As a result, SnO₂ is the phase that control the Sn doping limit. So that under thermodynamic equilibrium, μ_{Sn} can be calculated by

$$\mu_{Sn} = E(SnO_2) - 2\mu_O. \quad (3.7)$$

This is consistent with the observed impurity phase of SnO₂ in case of the excessive Sn doping as previously reported in experiment (Rajeshwari *et al.*, 2018).

3.3 Perfect vanadium pentoxide crystal

The crystal structure of orthorhombic V₂O₅ is well reported in previous experimental and theoretical studies (Bachmann *et al.*, 1961; Eyert and Höck, 1998). For the sake of completeness, its crystal structure was briefly discussed here. Figure 3.2(a) shows the unit cell containing two formula units (V₄O₁₀) with the calculated lattice constants of $a = 11.665 \text{ \AA}$, $b = 3.621 \text{ \AA}$, and $c = 4.447 \text{ \AA}$ which is in agreement with the experimental values ($a = 11.510 \text{ \AA}$, $b = 3.563 \text{ \AA}$, and $c = 4.369 \text{ \AA}$) (Bachmann *et al.*, 1961). Each vanadium ion is surrounded by five oxygen ions forming a distorted square pyramid (VO₅) with the calculated V-O bond lengths depicted in Figure 3.2(b). Three inequivalent oxygen atoms can be identified: vanadyl-oxygen (O1) pointing in the normal direction, bridge-oxygen (O2) at the corner-sharing polyhedra, and chain-oxygen (O3) at the edge-sharing polyhedra. The

monolayer V_2O_5 is formed by connecting the VO_5 pyramids via edge-sharing and corner-sharing polyhedra in ab -plane to form zigzag double chains along b -direction. These layers are stacked together along c -direction with weak van der Waals interaction to form a quasi-2D structure like graphite (Bachmann *et al.*, 1961; Enjalbert and Galy, 1986). Note that the calculated lattice constant c with dispersion energy correction (4.447 Å), is closer to the experimental value as compared to that without the correction (4.804 Å) (Scanlon *et al.*, 2008).

Likewise, the electronic structure of V_2O_5 has been extensively explored computationally and experimentally. It is an n -type semiconductor with an experimental band gap of 2.35 eV (Hieu and Lichtman, 1981). In this work, within the DFT+U description of $U_{3d}(V) = 3.5$ eV, the calculated PDOS exhibits similar band-gap energy (2.18 eV) and DOS features to those of the previous computational works, Figure 3.2(c) (Chakrabarti *et al.*, 1999; Lambrecht *et al.*, 1981). The top of the valence band (VB) is predominantly composed of O-2p, while the V-3d mainly contributes to the states at the conduction band (CB). Due to a large distortion of VO_5 pyramids from the octahedral symmetry, the interaction between V atoms are strong, resulting in the split-off of V-3d orbitals with a low-lying d_{xy} orbital (De Francesco *et al.*, 2006; Eyert and Höck, 1998; Lambrecht *et al.*, 1981; Q. Wang *et al.*, 2016).

In appendix A section, Table A.1 summarizes the calculated structural and electronic properties related values, i.e., lattice constants, bond lengths, and band-gap energy as compared to previous computations and experiments. The systematic agreement indicates that the inclusion of U parameter and van der Waals interaction in the model being studied is reliable. Note that the inclusion of van der Waals

interaction mainly affects the structural property, i.e., the interlayer spacing, whereas the U correction mostly changes the electronic structure, i.e., band-gap energy.

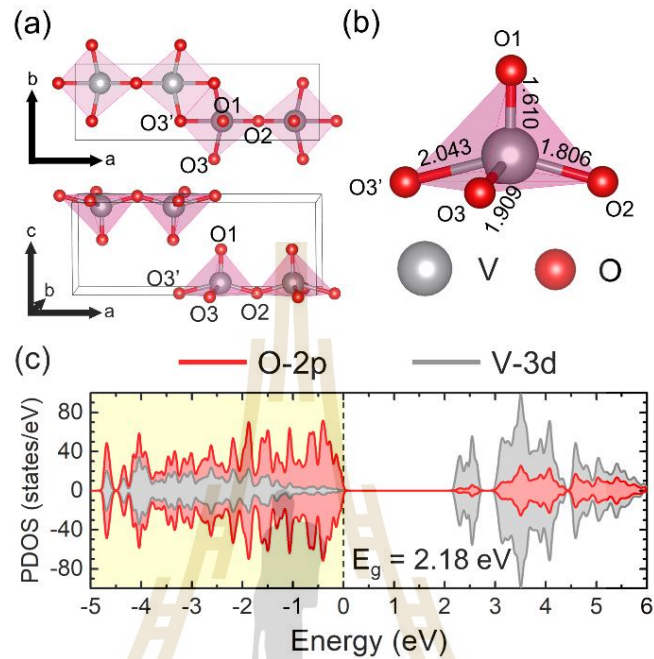


Figure 3.2 (a) unit cell of orthorhombic V_2O_5 containing 14 atoms where gray and red atoms represent V and O, respectively. (b) The pink polyhedron illustrates the distorted squared pyramid of VO_5 and all corresponding V-O bond lengths are in Å. All 3-dimensional representations of crystal structure are illustrated using VESTA program (Momma and Izumi, 2008). (c) The calculated projected density of states (PDOS) of pristine V_2O_5 . The zero in energy is set to VBM where dashed line indicates the energy level of the last occupied electron.

3.4 Intrinsic defects

In this section, the properties of various native point defects in V_2O_5 including electronic defects (electron and hole), vacancies, and self-interstitials were examined. The antisite disorders were neglected due to the mismatch in ionic radius and strong

ionicity of V_2O_5 similar to the case of TiO_2 (Na-Phattalung *et al.*, 2006). Herein, the model of neutral and charged defects were constructed. The optimized defect structures and corresponding gap state charge density of electronic defects and neutral vacancies and neutral interstitials are also shown in Figure 3.3(a-j). Furthermore, in some important cases, the density of state was calculated and plotted in Figure 3.3(k-m) to explore the electronic properties. Subsequently, the stability and donor/acceptor behavior of these defects were determined by considering defect formation energies (DFE). As mention earlier, the parameters are set corresponding to the representative growth condition, i.e., μ_O of -3.18 eV and annealing temperature of 723 K. In Figure 3.3, the DFE were plotted as a function of Fermi energy ranging from 0 to 2.18 eV corresponding to VBM and CBM. The slope of each line represents charge state of defect, and only the most stable charge state for a given Fermi energy are plotted. The detailed calculations of each defect species are described as follows.

A. Electronic defects

The electron-doped system was obtained by manually adding one extra electron into the supercell. The detail of local structure distortion and electronic structure of electron-doped system have been extensively discussed in a previous work (Watthaisong *et al.*, 2019). On one hand, the added electron localized at a V-center induces a small distortion around the VO_5 unit where the V–O bonds are slightly lengthened leading to a formation of a small electron polaron (η^-). The added electron mainly occupied the low-lying V- d_{xy} states at 1.2 eV above the VBM, which is consistent with the PDOS and the shape of the polaronic isosurface, as illustrated in Figure 3.3(a) and (k). Based on PBE+U method ($U=3.5$ eV), it should be noted that the electron polaron is not fully localized at the V-center, but partially (around 10%)

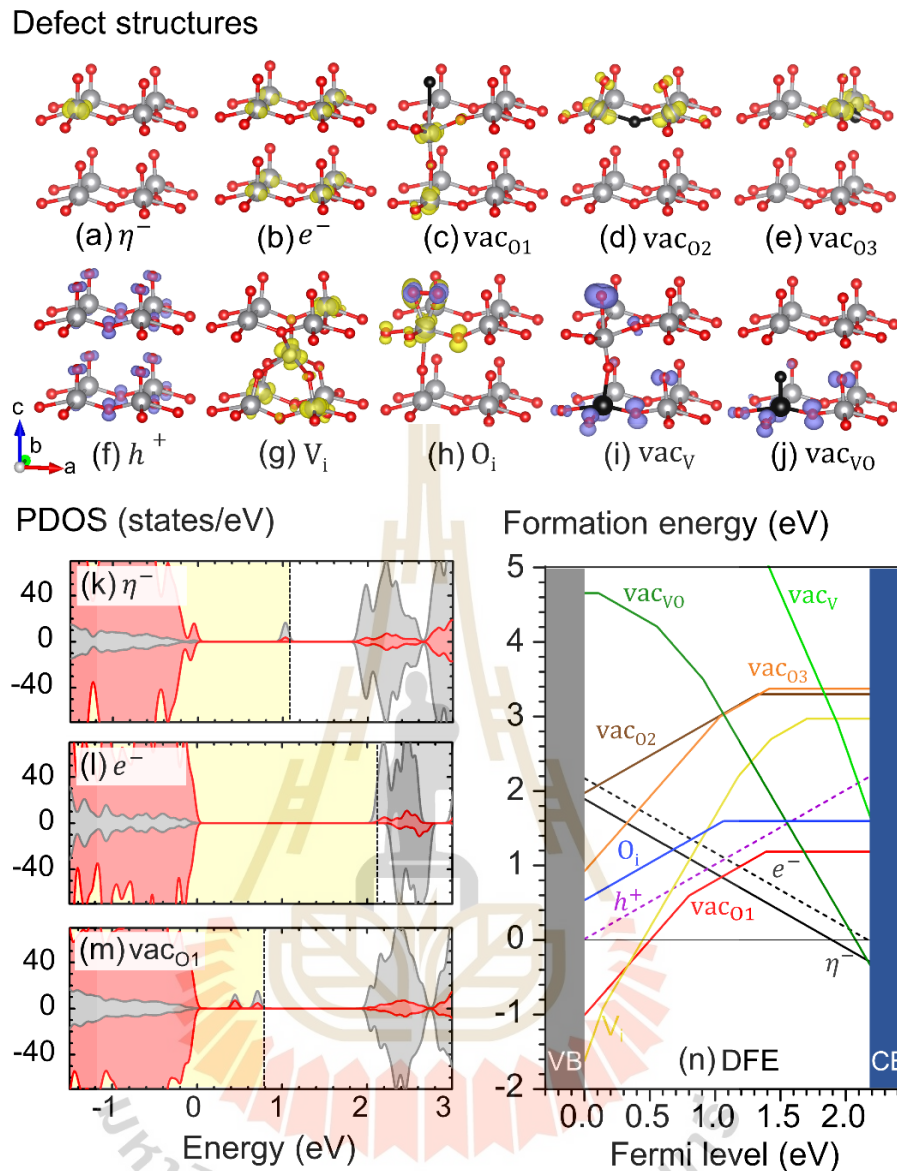


Figure 3.3 (a-j) Defect structures (near defect region) and gap state charge density of electronic defects, neutral vacancies, and neutral interstitials. The yellow and blue charge density represents occupied and unoccupied gap states. (k-m) The calculated PDOS of selected defects. (n) their defect formation energies at various charge states are plotted as a function of Fermi energy. The zero Fermi energy and its upper limit are set at VBM and CBM. The set of elemental chemical potentials is set as the experimental condition. The slope of each line indicates charge state of the defect, and only the most favorable charge state for a given Fermi energy is shown.

spills to the neighboring V center connected with O2 in *a*-direction. However, the charge localization is still located in a unit cell, referring as a small electron polaron.

In Figure 3.3(n), the black solid line represents DFE of η^- in charge state -1. It is intersected with the zero formation energy for perfect V_2O_5 as plotted in black horizontal line at the Fermi energy of 1.89 eV. Beyond this Fermi energy, the perfect crystal prefers to receive an electron to form the more stable electron polaron due to its lower DFE. In other words, the polaronic defect exhibits the charge transition level (CTL) between 0 and -1 charge state at $\varepsilon(0/-1) = 1.89$ eV. Indeed, the electron polaron can be occurred under the Fermi energy below the $\varepsilon(0/-1)$, but in less proportion depending on the exponential of its DFE at that Fermi energy.

On the other hand, the added electron can exhibit delocalization behavior, which partially occupies all V centers in the supercell. Such behavior contributes to a shift of the Fermi energy into the conduction band indicating a formation of a free electron (e^-), as shown in Figure. 3.3(l). The DFE of e^- is also plotted as black dashed line. The formation of small electron polaron is energetically more favorable with a self-trapped energy of 0.28 eV which is consistent with the previously reported value of 0.22 and 0.40 eV (De Jesus *et al.*, 2016; Watthaisong *et al.*, 2019). The quantitative difference could be originated from the strong influence of the applied U-value as also discussed in previous work (Watthaisong *et al.*, 2019). The preferred trapped state implies that carrier species in V_2O_5 are mainly small polarons rather than free electrons as also mentioned in several other theoretical studies (Carrasco, 2014; De Jesus *et al.*, 2016; Ioffe and Patrino, 1970; Scanlon *et al.*, 2008; Suthirakun, Genest, *et al.*, 2018; Suthirakun, Jungthawan, *et al.*, 2018; Watthaisong *et al.*, 2019). The computational predictions are consistent with the XPS

result of the reduced V_2O_5 showing the existence of partial V^{4+} centers (Sun *et al.*, 2018; Wu *et al.*, 2004).

In addition, the analogous calculation for hole-doped system was investigated where an electron is removed from the supercell. In contrast to electron doping, a hole prefers to partially delocalize over all O atoms in the supercell and contributes to unoccupied states as a free hole (h^+) as shown in Figure 3.3(f). The DFE of h^+ is plotted as purple dotted line in Figure 3.3(n). Notably, the polaronic behaviors, e.g. charge localization and deep gap state, cannot be captured by this setting parameters.

B. Oxygen vacancies

Oxygen vacancies (vac_O) are generally created from thermal and chemical reduction, which can be measured by many experimental techniques (Devriendt *et al.*, 1996; Hermann *et al.*, 1999; Kang *et al.*, 2014; Su and Schlögl, 2002). The role and effect of vac_O on such application are of great interest. In theoretical studies, the geometrical and electronic structure induced by vac_O are extensively investigated on both surface (Ganduglia-Pirovano and Sauer, 2004; Goclon *et al.*, 2009; Hermann *et al.*, 2001) and bulk models (Scanlon *et al.*, 2008). From the crystal structure of V_2O_5 , there are three inequivalent oxygen sites: vanadyl oxygen (O1), bridge oxygen (O2) and chain oxygen (O3). Scanlon *et al.* examined geometrical and electronic structures of all three distinct vac_O . They reported that oxygen vacancies can produce electron polarons into the system, leading to the increase in carrier concentration and electronic conductivity (Scanlon *et al.*, 2008).

To repeat the Scanlon *et al.*, the neutral O1, O2, and O3 vacancies were studied in this work with the van der Waals interaction. As a result, the vac_O in

all three cases can induce the local lattice distortion and donates two extra electrons that localized at two neighboring V-centers, becoming two electron polarons as shown in Figure 3.3(c-e). In Figure 3.3(m), the calculated PDOS of O1 vacancy shows that the two polaronic gap states are in the same spin component which is consistent with the ferromagnetism of V_2O_{5-x} in previous experiment and calculation (Cezar *et al.*, 2014; Xiao and Guo, 2009). However, the configuration of these two polarons are different, depending on the symmetry of vac_O . In case of O1 vacancy (vac_{O1}), it forms the stable apex-shared V_2O_9 bi-pyramid (see Figure 3.3(c)). Upon the formation of vac_{O1} , the undercoordinated V atom moves downward to form V-O1 bond with the O1 of the underneath layer. Such a distorted structure allows accommodation of the two polarons resulting in a stable bi-polaronic configuration ($V^{4+}-O-V^{4+}$) as illustrated in the charge density plot of Figure 3.3(c). On the contrary, O2 vacancy (vac_{O2}) repels the two neighboring undercoordinated V-centers in x -direction, leading to two polarons localized on both neighboring V-centers as shown in Figure 3.3(d). Likewise, the formation of the O3 vacancy (vac_{O3}) pushes the neighboring V-centers in the y -direction, resulting in the polarons localized on both V-centers as depicted in Figure 3.3(e). These polarons configurations are consistent with the finding in Scanlon *et al.* work.

Next, the relative stabilities of all vac_O , i.e., vac_{O1} , vac_{O2} , and vac_{O3} were examined. Due to the two occupied gap states (electron polarons), an oxygen vacancy can donate up to two electrons to the host material, yielding possible charge states of +2, +1, or 0. The calculated DFE of vac_{O1} , vac_{O2} , and vac_{O3} in possible charge states are plotted as red, brown, and orange lines in Figure 3.3(n). All vac_O exhibit neutral charge states at Fermi energy close to the CBM. These defects donate

their electrons to form charge state of +1 at the $\varepsilon(+1/0) = 1.40, 1.34,$ and 1.41 eV for $\text{vac}_{\text{O}1}$, $\text{vac}_{\text{O}2}$, and $\text{vac}_{\text{O}3}$, respectively. It should be noted that the charge transition levels are quite far from the CBM, so that the vac_{O} can be referred as deep donor defect. In addition, $\text{vac}_{\text{O}1}$ and $\text{vac}_{\text{O}3}$ can further donate the remaining electron to form charge state +2 at the $\varepsilon(+2/+1) = 0.81$ and 1.03 eV, respectively. The $\text{vac}_{\text{O}2}$ of +2 charge state does not exist because its optimized structure involves movement of O1 to occupy the original $\text{vac}_{\text{O}2}$ position and form a $\text{vac}_{\text{O}1}$ instead.

Furthermore, the calculated DFEs indicate that the $\text{vac}_{\text{O}1}$ is much more stable than $\text{vac}_{\text{O}2}$ and $\text{vac}_{\text{O}3}$ by at least 2 eV. This is because the two V-centers of apex-shared V_2O_9 in $\text{vac}_{\text{O}1}$ is more stable than the V-centers with dangling bonds in $\text{vac}_{\text{O}2}$ and $\text{vac}_{\text{O}3}$. Thus, vac_{O} is likely to take place at the O1 site which agrees very well with the previous works (Basu *et al.*, 2016; Fujikata *et al.*, 2020; Kang *et al.*, 2014; Scanlon *et al.*, 2008).

C. Vanadium interstitials

To create the neutral V self-interstitial defect (V_i), a V atom was inserted between V_2O_5 layers where it is surrounded by six O atoms including four O1 atoms of below layer and two O2 atoms of the above layer with the V-O bond lengths of $2.06 - 2.13 \text{ \AA}$, as shown in Figure 3.3(g). The inserted position of the interstitial atom corresponds well with the previous computational works such as Li interstitial (Scanlon *et al.*, 2008) and other cations interstitial (McCull *et al.*, 2018). The neutral V_i generated five electrons aligned in the same spin. The two of the five electrons localize at the V_i site whereas the other three electrons are trapped as small polarons at the three different neighboring V-centers, as shown in occupied states charge density in Figure 3.3(g). The local distortion occurred upon the polaron formation

pushes the inserted V atom to the off-centered position which minimizes the distance to the three reduced V-centers. These three polarons are arranged in such a way that the in-plane distortion and vertical repulsion are avoided (Suthirakun, Jungthawan, *et al.*, 2018). It is noted that the V_i , theoretically, donates only three extra electrons to form the polarons resulting in an oxidation state of V^{3+} . Such a high charge state could dramatically increase carrier concentrations, which in turn, improve electronic conductivity of the materials. The yellow line in Figure 3.3(n) illustrates the DFE of V_i in different charge states, which composes of 4 donor transition levels as listed here: $\varepsilon(+5/+3) = 0.15$ eV, $\varepsilon(+3/+2) = 1.19$ eV, $\varepsilon(+2/+1) = 1.41$ eV, and $\varepsilon(+1/0) = 1.69$ eV. Notice that the charge state +3, corresponding to donated three polarons at the nearby V_i , is stable in the wide region. Whereas the charge state +5 which donate the two self-localized polarons is stable only at fermi energy approach VBM. The highly charged donor (+3 and +5) of V_i is energetically more favorable than double donor vac_{O1} when fermi energy approaches to VBM. Notably, the negative DFE of V_i and vac_{O1} could be limited the p-type doping. This is because the impurity defect would be compensated by these defects instead of h^+ . So, the doping would not increase h^+ concentration (Freysoldt *et al.*, 2014).

D. Oxygen interstitials

Likewise, the neutral O self-interstitial (O_i) was considered similar to V self-interstitial. An O atom was inserted at the high symmetric site between the layers as the initial configuration. After geometry relaxation, the inserted O atom is likely to bond with one terminal O1 atom. The O-O bond is tilted from the a -axis to c -axis by 45° with the bond length of 1.33 \AA and denoted as “normal interstitial” as shown in Figure 3.4(a). In addition, the configuration where the pair of O interstitial

and lattice O1 share the same O1 site which is called “split interstitial” as shown in Figure 3.4(b) was considered. The O-O bond length is 1.34 Å, aligned parallel to *a*-axis. The center of the bond is at the lattice O1 site with the O and V distance of 2.00 Å. In other words, this defect can be named as a substitution of O₂ molecule at O1 site whereas the O-O bond is slightly longer than that of the O₂ molecule (1.21 Å). This type of defect is also found in other metal oxides e.g. Ga₂O₃ (Kobayashi *et al.*, 2019), TiO₂ (Na-Phattalung *et al.*, 2006), and ZnO (Limpijumnong *et al.*, 2005). In addition, the electronic energy of the O split interstitial becomes lower than that of the normal one around 0.36 eV. Therefore, the O split interstitial was selected as a representative for the defect.

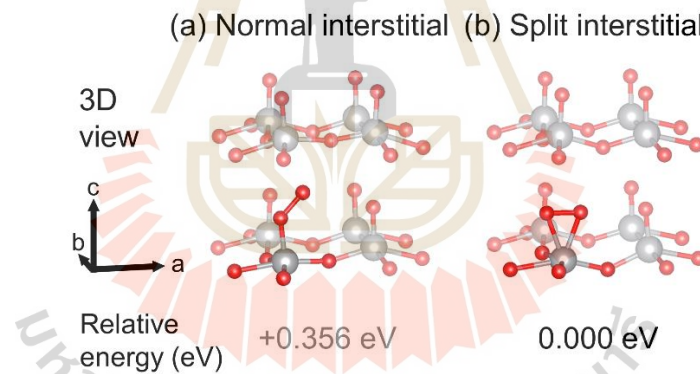


Figure 3.4 The crystal structure of O interstitial in two configurations which are (a) normal interstitial and (b) split interstitial. Only structures at the region near the defect site are shown for clarity. Also, the relative energy of each configuration compared to the lowest energy configuration.

In Figure 3.3(h), the charge density of neutral O split interstitial (O_i) displays both occupied and unoccupied states as the yellow and blue-colored isosurface. Both occupied and unoccupied gap states indicate that O_i could act as both

donor and acceptor. From the calculated DFE (blue line in Figure 3.3(n)), the O_i defect is, however, stable in the charge state 0 and +1 with CTL at $\varepsilon(+1/0) = 1.06$ eV. The O_i donates an electron occupied in the highest energy state and turns to be a single donor under lower Fermi energy. In general, the O_i in metal oxides is likely to be the acceptors, it is interesting that the O_i in V_2O_5 is more stable as donors rather than acceptors. Such donor behavior of the O_i has also been reported in other metal oxides (Pakeetood *et al.*, 2019). While the acceptor state (charge state of -1) is not likely to occur since the added electron does not fill the unoccupied state of O-O π antibonding, instead it forms a small polaron at the nearby V-center. In addition, a higher charge state of O_i defect was examined. The molecular O_2 located at O1 site in the double donor O_i tends to move away from the lower V-center. As a result, the defect O_i is decomposed into O_2 molecule and vac_{O1} . Thus, the O_i in higher charge state can be neglected due to its instability.

E. Vanadium vacancies and Vanadyl vacancies

As shown in Figure 3.3(i), a formation of neutral V vacancy (vac_V) creates a large lattice reorganization around the defect site. The V-center directly above the defect site displaces downward to bond with the dangling O1 atom with the V-O1 bond length of 1.61 Å yielding a distorted VO_6 octahedra. Such reorganization was accompanied by the breaking of V-O1 bond of the original VO_5 square pyramid where its equilibrium distance become 2.26 Å, leaving an isolated oxygen atom between the V_2O_5 layers. Its five unoccupied gap states are plotted as blue-colored isosurface in Figure 3.3(i). Its calculated DFE of vac_V in charge states ranging from 0 to -5 are plotted as light green color in Figure 3.3(n). The DFE of vac_V is

significantly higher than those other defects, leading to the thermodynamically unstable.

In addition, the dramatic reorganization occurred upon the formation of vac_V leads to the formation of an isolated oxygen atom and gives rise to a possible formation of vanadyl vacancy (vac_{VO}). In other words, it is structurally appealing to remove both V and its O1 at the same time. Formation of vac_{VO} does not significantly distort the host structure as compared with that of the vac_V . Its charge density of three unoccupied states reveals the formation of large hole polarons at the layered oxygen atoms as shown in Figure 3.3(h). The calculated DFE of vac_{VO} in charge states 0 to -3 are plotted as dark green color in Figure 3.3(n). Only highly charged acceptor of -3 is dominant when the Fermi energy approaches the CBM. Note that this defect is identical to the complex defect between vac_V and vac_{O1} . The calculated binding energy of the defect complex, i.e., $\text{vac}_{VO} \rightarrow \text{vac}_V + \text{vac}_{O1}$, is 3.80 eV at the Fermi energy of 1.0 eV above the VBM. Such a high binding energy implies that it is more likely to form the vacancy pair, vac_{VO} , rather than the isolated vac_V and vac_{O1} .

According to the calculated DFEs, vac_V and vac_{VO} generate shallow acceptor states that can provide holes to the system. However, the acceptors are readily compensated by the low DFE donors, i.e., vac_{O1} , instead of forming a hole at both conditions. As a result, the intrinsic *p*-type doping is difficult to occur in V_2O_5 . Nevertheless, it is noted that the recent work has been reported *p*-type conductivity of hydrated amorphous V_2O_5 (Choi *et al.*, 2019).

3.5 Sn-related defects

So far, the defect properties intrinsic defects relating to both native V and O atoms and their stabilities was examined. In this section, the formation of point defects originated from Sn doping was further investigated. The local defect structure and electronic properties of Sn-related defects as well as their stabilities were calculated and discuss like the previous section. Three possibilities of Sn incorporation were considered as proposed in the experiments including i) Sn interstitial, ii) Sn substitution for V, and iii) Sn substitution for vanadyl (VO). The optimized defect structures and corresponding gap state charge density of neutral Sn-related defects are shown in Figure 3.5(a-c) as well as the corresponding density of state in Figure 3.5(d-f). Subsequently, the stability and donor/acceptor behavior of these defects were determined by considering defect formation energies (DFE) as also shown in Figure 3.5(g). The detailed properties of each defect were discussed as follows.

A. Tin interstitial

In case of Sn interstitial (Sn_i), a Sn atom was inserted between V_2O_5 layers where it is surrounded by six O atoms including four O1 atoms of below layer and two O2 atoms of the above layer, as shown in Figure 3.5(a). The inserted position of the interstitial atom corresponds well with a previous work of Sn interstitial. In the neutral charge state of Sn_i , four occupied gap states corresponding to four electrons were observed in PDOS in Figure 3.5(d). The first two states with opposite spin alignment are partially shared between s-orbital of Sn atom and nearby atoms like covalent interaction. While the remaining two are fully localized at two neighbor V-

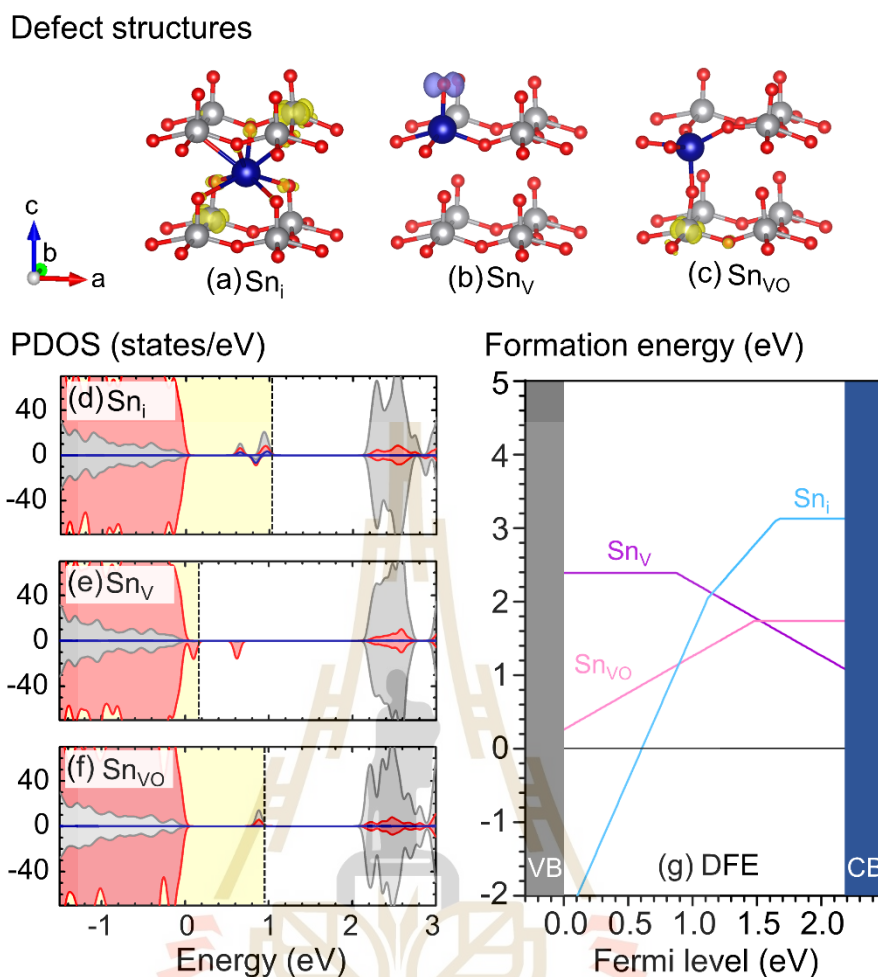


Figure 3.5 (a-c) Defect structures (near defect region) and gap state charge density of (a) Sn interstitial, Sn_i (b) Sn substitution for V, Sn_V and (c) Sn substitution for VO, Sn_{VO} . Sn doping atoms are illustrated by dark blue balls. The yellow and blue charge density represents occupied and unoccupied gap states. (d-f) The corresponding PDOS of Sn-related defects. (g) their defect formation energies at various charge states are plotted as a function of Fermi energy.

centers next to the interstitial site, forming two polarons in the same spin alignment. In addition, the interstitial atom is off-center e.g. shifting toward those polarons. These finding agree very well with a previous calculation of Sn_i defect in V_2O_5

(Suthirakun, Jungthawan, *et al.*, 2018). Due to two electrons localized at Sn atom, the oxidation state of Sn_i is more likely to be +2 instead of +4. The DFE of Sn_i is plotted as light-blue line in Figure 3.5(g). The Sn_i defect can be formed in the charge state +4, +2, and 0, with the CTLs are $\varepsilon(+4/+2) = 1.12$ eV and $\varepsilon(+2/0) = 1.68$ eV. As a result, the Sn_i acts as a deep donor defect. Although, the calculated DFE in high positively charge state (+4) is significantly low in Fermi energy below 0.9 eV, the charge balancing acceptors like vac_V or vac_{V0} is not likely to form due to their high DFEs at that region. As a result, only electron polarons could be charge compensator for Sn_i , becoming the lower charge state e.g., +2 or 0. However, the DFE of the +2 or 0 charge state is quite high compared to the other Sn-related defects. Thus, the formation Sn_i is not favorable.

B. Tin substitution for vanadium

Figure 3.5(b) shows the defect structure of Sn substitution for V (Sn_V). Five O atoms slightly move outward the Sn dopant due to the larger ionic radius of Sn^{4+} compared to V^{5+} . In theoretical, Sn^{4+} substituted for lattice V (V^{5+}) can generate the defect with charge state of -1. The negatively charged Sn_V can be compensated by the hole localization at the neighboring O1 as shown in blue isosurface. This is corresponded to the unoccupied state in PDOS of neutral Sn_V as shown in Figure 3.5(e). Notice that the hole polaron in the hole-doped system cannot be observed, but the hole localization can be found in this case. The DFE of Sn_V is plotted as purple line in Figure 3.5(g). The neutral charge state has comparatively high in formation energy. It is more stable as a singly acceptor at charge state -1 in a wide range of Fermi energy with the CTL $\varepsilon(0/-1) = 0.88$ eV. This negatively charged Sn_V could be

compensated by other positively charged defect especially vac_{O1} which is the most stable intrinsic defect.

C. Tin substitution for vanadyl group

According to the charge compensation mechanism of Sn_{V} as mentioned earlier, the combination of negatively charged Sn_{V} and the most stable positively charged vac_{O1} was considered. In other words, Sn replaced both V atom and the connected O1 atom (vanadyl group), instead of only V so-called Sn substitution for VO (Sn_{VO}). This is also consistent with experimental work done by Li *et al.* where they proposed the possibility of Sn substitutional defect incorporating with oxygen vacancy (Z. Y. Li *et al.*, 2016). The defect structure of neutral Sn_{VO} and its corresponding charge density are shown Figure 3.5(c). The Sn_{VO} contributes lattice distortion similar to the case of vac_{O1} where Sn moves downward to the underneath V-center and forms the apex-shared bipyramid of Sn-center and V-center. An electron polaron localized in the V-center below the Sn atom was found as shown in yellow isosurface. The DFE of Sn_{VO} is plotted as pink line in Figure 3.5(g). It can be formed in charge state +1 and 0. The neutral defect can be act as a single donor by giving the electron polaron to the system resulting in charge state +1. This single donor is more stable in wide range of Fermi energy with the CTL $\varepsilon(+1/0) = 1.49$ eV. Notably, among Sn-related defects, the DFE of Sn_{VO} donor is lower than that of the Sn_{i} and Sn_{V} in a middle region of Fermi energy, i.e., between 0.90 and 1.53 eV. Beyond, the Fermi energy of 1.53 eV, the acceptor Sn_{V} becomes more dominant.

D. Bader charge analysis

Furthermore, the Bader charge analysis was also carried out to study the charge transfer of Sn dopant to surrounding atoms. The basic concept of Bader

charge is originated from the dividing of molecules into atoms based on their electronic charge density so-called Bader partitioning as developed by Richard Bader. A zero flux surfaces, which is a 2D surface with a minimum charge density perpendicular to the surface, was used to separate atom from each other. The charge enclosed within this Bader volume is called Bader charge which can be a proper estimation for total electronic charge inside an atom. A grid based method was proposed to calculate Bader charge population (Tang *et al.*, 2009) which is also used in this work.

To estimate the oxidation number of Sn dopant in each defect, the Bader charge of Sn dopant in each defect system was calculated and compared to that in tin oxides as shown in Table 3.1. The Sn dopant in Sn_i should have oxidation number of +2 because of the similar Bader charges of $+1.55 e^-$ (Sn_i) compared to $+1.24 e^-$ (SnO). This agrees well with the calculated PDOS and charge density of neutral Sn_i . On the contrary, the Sn dopant in Sn_V and Sn_{VO} should have oxidation number of +4 because of the similar Bader charges of $+2.37 e^-$ (Sn_V) and $+2.45 e^-$ (Sn_{VO}) compared to $+2.42 e^-$ (SnO_2). It should be noted that the XAS result reveals the oxidation state of Sn in Sn-doped V_2O_5 to be 4+ (Y. W. Li *et al.*, 2013; Xing *et al.*, 2019). So that the lower Sn oxidation state like Sn_i with 2+ state might not be the dominant defect in the Sn-doped V_2O_5 .

Table 3.1 Bader charge analysis of Sn atom in Sn oxides and Sn-related defects.

Systems	SnO	SnO ₂	Sn _i	Sn _V	Sn _{VO}
Bader charge	+1.24	+2.42	+1.55	+2.37	+2.48

3.6 Discussion

By considering all possible intrinsic defects that can be occurred in V_2O_5 , the vac_{O1} has the lowest DFE in a wide range of Fermi energy which is mostly stable in single or double donor states. The donating electrons prefers to localize as electron polarons rather than free electron, and the polarons could be considered as charge carriers of the material. When the Fermi energy approaches to VBM, the highly charged V_i can be major donor defects. On the other hand, the highly charged vac_{VO} can be major acceptor defects when Fermi energy approaches to CBM. However, these highly charged defects are not likely to form because of lacking compensating defects.

For Sn-related defects, all three possibilities can be the most dominant defect depending on the Fermi energy of the system. At the Fermi energy lower than 0.90 eV, the highly charged Sn_i becomes dominant donor defects. While the single donor and neutral Sn_{VO} are stable when the Fermi energy ranging from 0.90 to 1.53 eV. Beyond this point the single acceptor of Sn_V turns into the dominant defects. However, these donors and acceptors may need other compensators which could be the dominant intrinsic defects, electrons, holes, or even the other Sn-related defects.

To identify the most stable defect, the specific position of Fermi energy should be known. In chapter IV, the Fermi energy was pinned, and the defect concentrations were calculated by using a statistical model based on constraint of charge neutrality.

3.7 References

Bachmann, H., Ahmed, F. and Barnes, W. (1961). The Crystal Structure of Vanadium Pentoxide. **Z. Kristallogr.** 115: 110.

- Basu, R., Prasad, A. K., Dhara, S. and Das, A. (2016). Role of Vanadyl Oxygen in Understanding Metallic Behavior of $V_2O_5(001)$ Nanorods. **J. Phys. Chem. C.** 120: 26539.
- Carrasco, J. (2014). Role of Van der Waals Forces in Thermodynamics and Kinetics of Layered Transition Metal Oxide Electrodes: Alkali and Alkaline-Earth Ion Insertion into V_2O_5 . **J. Phys. Chem. C.** 118: 19599.
- Cezar, A. B., Graff, I. L., Varalda, J., Schreiner, W. H. and Mosca, D. H. (2014). Oxygen-Vacancy-Induced Room-Temperature Magnetization in Lamellar V_2O_5 Thin Films. **J. Appl. Phys.** 116: 163904.
- Chakrabarti, A., Hermann, K., Druzinic, R., Witko, M., Wagner, F. and Petersen, M. (1999). Geometric and Electronic Structure of Vanadium Pentoxide: A Density Functional Bulk and Surface Study. **Phys. Rev. B.** 59: 10583.
- Choi, H., Kwon, Y. J., Paik, J., Seol, J.-B. and Jeong, Y. K. (2019). p-Type Conductivity of Hydrated Amorphous V_2O_5 and Its Enhanced Photocatalytic Performance in $ZnO/V_2O_5/rGO$. **ACS Applied Electronic Materials.** 1: 1881.
- De Francesco, R., Stener, M., Causà, M., Toffoli, D. and Fronzoni, G. (2006). Time Dependent Density Functional Investigation of the Near-Edge Absorption Spectra of V_2O_5 . **Phys. Chem. Chem. Phys.** 8: 4300.
- De Jesus, L. R., Horrocks, G. A., Liang, Y., Parija, A., Jaye, C., Wangoh, L., Wang, J., Fischer, D. A., Piper, L. F. J., Prendergast, D. and Banerjee, S. (2016). Mapping Polaronic States and Lithiation Gradients in Individual V_2O_5 Nanowires. **Nat. Commun.** 7: 12022.

- Devriendt, K., Poelman, H., Fiermans, L., Creten, G. and Froment, G. F. (1996). Angular Resolved XPS Applied to V₂O₅-Based Catalysts. **Surf. Sci.** 352-354: 750.
- Enjalbert, R. and Galy, J. (1986). A Refinement of the Structure of V₂O₅. **Acta Crystallogr., Sect. C.** 42: 1467.
- Eyert, V. and Höck, K. H. (1998). Electronic Structure of V₂O₅: Role of Octahedral Deformations. **Phys. Rev. B.** 57: 12727.
- Freysoldt, C., Grabowski, B., Hickel, T., Neugebauer, J., Kresse, G., Janotti, A. and Van de Walle, C. G. (2014). First-Principles Calculations for Point Defects in Solids. **Rev. Mod. Phys.** 86: 253.
- Fujikata, Y., Ota, F., Hatada, K. and Krüger, P. (2020). Many-Body and Anisotropy Effects in X-ray Absorption Spectra of Pristine and Defective Vanadium Pentoxide. **Phys. Rev. B.** 101: 125124.
- Ganduglia-Pirovano, M. V. and Sauer, J. (2004). Stability of Reduced V₂O₅ (001) Surfaces. **Phys. Rev. B.** 70: 045422.
- Goclon, J., Grybos, R., Witko, M. and Hafner, J. (2009). Relative Stability of Low-index V₂O₅ Surfaces: A Density Functional Investigation. **J. Phys.: Condens. Matter.** 21: 095008.
- Hermann, K., Witko, M., Druzinic, R., Chakrabarti, A., Tepper, B., Elsner, M., Gorschlüter, A., Kühlenbeck, H. and Freund, H. J. (1999). Properties and Identification of Oxygen Sites at the V₂O₅(010) Surface: Theoretical Cluster Studies and Photoemission Experiments. **J. Electron Spectrosc. Relat. Phenom.** 98-99: 245.

- Hermann, K., Witko, M., Druzinic, R. and Tokarz, R. (2001). Oxygen Vacancies at Oxide Surfaces: ab initio Density Functional Theory Studies on Vanadium Pentoxide. **Appl. Phys. A.** 72: 429.
- Hieu, N. V. and Lichtman, D. (1981). Bandgap Radiation Induced Photodesorption from V_2O_5 Powder and Vanadium Oxide Surfaces. **J. Vac. Sci. Technol.** 18: 49.
- Ioffe, V. A. and Patrino, I. B. (1970). Comparison of the Small-Polaron Theory with the Experimental Data of Current Transport in V_2O_5 . **Phys. Status Solidi B.** 40: 389.
- Kang, T. D., Chung, J. S. and Yoon, J.-G. (2014). Anisotropic Optical Response of Nanocrystalline V_2O_5 Thin Films and Effects of Oxygen Vacancy Formation. **Phys. Rev. B.** 89: 094201.
- Kobayashi, T., Gake, T., Kumagai, Y., Oba, F. and Matsushita, Y.-i. (2019). Energetics and Electronic Structure of Native Point Defects in α - Ga_2O_3 . **Appl. Phys. Express.** 12: 091001.
- Lambert, D. S., Murphy, S. T., Lennon, A. and Burr, P. A. (2017). Formation of Intrinsic and Silicon Defects in MoO_3 under Varied Oxygen Partial Pressure and Temperature Conditions: An ab initio DFT Investigation. **RSC Adv.** 7: 53810.
- Lambrech, W., Djafari-Rouhani, B. and Vennik, J. (1981). On the Origin of the Split-off Conduction Bands in V_2O_5 . **J. Phys. C: Solid State Phys.** 14: 4785.
- Lee, J. and Han, S. (2013). Thermodynamics of Native Point Defects in α - Fe_2O_3 : An ab initio Study. **Phys. Chem. Chem. Phys.** 15: 18906.

- Li, Y. W., Yao, J. H., Uchaker, E., Zhang, M., Tian, J. J., Liu, X. Y. and Cao, G. Z. (2013). Sn-Doped V_2O_5 Film with Enhanced Lithium-Ion Storage Performance. **J. Phys. Chem. C.** 117: 23507.
- Li, Z. Y., Zhang, C. K., Liu, C. F., Fu, H. Y., Nan, X. H., Wang, K., Li, X. Y., Ma, W. D., Lu, X. M. and Cao, G. Z. (2016). Enhanced Electrochemical Properties of Sn-Doped V_2O_5 as a Cathode Material for Lithium Ion Batteries. **Electrochim. Acta.** 222: 1831.
- Limpijumrong, S., Li, X., Wei, S.-H. and Zhang, S. B. (2005). Substitutional Diatomic Molecules NO, NC, CO, N_2 , and O_2 : Their Vibrational Frequencies and Effects on P Doping of ZnO. **Appl. Phys. Lett.** 86: 211910.
- Lutfalla, S., Shapovalov, V. and Bell, A. T. (2011). Calibration of the DFT/GGA plus U Method for Determination of Reduction Energies for Transition and Rare Earth Metal Oxides of Ti, V, Mo, and Ce. **J. Chem. Theory Comput.** 7: 2218.
- McColl, K., Johnson, I. and Cora, F. (2018). Thermodynamics and Defect Chemistry of Substitutional and Interstitial Cation Doping in Layered Alpha- V_2O_5 . **Phys. Chem. Chem. Phys.** 20: 15002.
- Momma, K. and Izumi, F. (2008). VESTA: A Three-Dimensional Visualization System for Electronic and Structural Analysis. **J. Appl. Crystallogr.** 41: 653.
- Murphy, S. T. and Hine, N. D. M. (2013). Anisotropic Charge Screening and Supercell Size Convergence of Defect Formation Energies. **Phys. Rev. B.** 87: 094111.

- Na-Phattalung, S., Smith, M. F., Kim, K., Du, M.-H., Wei, S.-H., Zhang, S. B. and Limpijumnong, S. (2006). First-Principles Study of Native Defects in Anatase TiO₂. **Phys. Rev. B.** 73: 125205.
- Pakeetood, P., Reunchan, P., Boonchun, A., Limpijumnong, S., Munprom, R., Ahuja, R. and T-Thienprasert, J. (2019). Hybrid-Functional Study of Native Defects and W/Mo-Doped in Monoclinic-Bismuth Vanadate. **J. Phys. Chem. C.** 123: 14508.
- Rajeshwari, S., Kumar, J. S., Rajendrakumar, R. T., Ponpandian, N. and Thangadurai, P. (2018). Influence of Sn ion doping on the photocatalytic performance of V₂O₅ nanorods prepared by hydrothermal method. **Mater. Res. Express.** 5: 13.
- Scanlon, D. O., Walsh, A., Morgan, B. J. and Watson, G. W. (2008). An ab initio Study of Reduction of V₂O₅ through the Formation of Oxygen Vacancies and Li Intercalation. **J. Phys. Chem. C.** 112: 9903.
- Shi, L., Vathonne, E., Oison, V., Freyss, M. and Hayn, R. (2016). First-Principles DFT+U Investigation of Charged States of Defects and Fission Gas Atoms in CeO₂. **Phys. Rev. B.** 94: 115132.
- Steffen, C., Thomas, K., Huniar, U., Hellweg, A., Rubner, O. and Schroer, A. (2010). TmoleX—A graphical user interface for TURBOMOLE. **J. Comput. Chem.** 31: 2967.
- Su, D. S. and Schlögl, R. (2002). Thermal Decomposition of Divanadium Pentoxide V₂O₅: Towards a Nanocrystalline V₂O₃ Phase. **Catal. Lett.** 83: 115.
- Sun, Y., Xie, Z. and Li, Y. (2018). Enhanced Lithium Storage Performance of V₂O₅ with Oxygen Vacancy. **RSC Adv.** 8: 39371.

- Suthirakun, S., Genest, A. and Rösch, N. (2018). Modeling Polaron-Coupled Li Cation Diffusion in V_2O_5 Cathode Material. **J. Phys. Chem. C.** 122: 150.
- Suthirakun, S., Jungthawan, S. and Limpijumnong, S. (2018). Effect of Sn-Doping on Behavior of Li-Intercalation in V_2O_5 Cathode Materials of Li-Ion Batteries: A Computational Perspective. **J. Phys. Chem. C.** 122: 5896.
- Tang, W., Sanville, E. and Henkelman, G. (2009). A grid-based Bader analysis algorithm without lattice bias. **J. Phys.: Condens. Matter.** 21: 084204.
- Wang, L., Maxisch, T. and Ceder, G. (2006). Oxidation Energies of Transition Metal Oxides within the GGA+U Framework. **Phys. Rev. B.** 73: 195107.
- Wang, Q., Brier, M., Joshi, S., Puntambekar, A. and Chakrapani, V. (2016). Defect-Induced Burstein-Moss Shift in Reduced V_2O_5 Nanostructures. **Phys. Rev. B.** 94: 245305.
- Wattthaisong, P., Jungthawan, S., Hirunsit, P. and Suthirakun, S. (2019). Transport Properties of Electron Small Polarons in a V_2O_5 Cathode of Li-ion Batteries: A Computational Study. **RSC Adv.** 9: 19483.
- Wu, Q.-H., Thissen, A., Jaegermann, W. and Liu, M. (2004). Photoelectron Spectroscopy Study of Oxygen Vacancy on Vanadium Oxides Surface. **Appl. Surf. Sci.** 236: 473.
- Xiao, Z. R. and Guo, G. Y. (2009). Structural, Electronic and Magnetic Properties of V_2O_{5-x} : An ab initio Study. **J. Chem. Phys.** 130: 214704.
- Xing, L., Yu, Q., Bao, Y., Chu, J., Han, K., Chong, S., Lao, C.-Y., Lai, F., Li, P., Xi, K. and Wang, W. (2019). Strong (001) Facet-Induced Growth of Multi-Hierarchical Tremella-Like Sn-Doped V_2O_5 for high-performance potassium-ion batteries. **J. Mater. Chem. A.** 7: 25993.

Zhang, S. B. and Northrup, J. E. (1991). Chemical Potential Dependence of Defect Formation Energies in GaAs: Application to Ga Self-Diffusion. **Phys. Rev. Lett.** 67: 2339.



CHAPTER IV

DEFECT CONCENTRATIONS

4.1 Introduction

The aim of this chapter is to identify the most dominant defect and to study the charge compensation mechanism by considering defect and carrier concentrations under constraint of charge neutrality. In fact, a statistical model was applied to estimate the concentration of each defect specie based on its DFE. The equilibrium Fermi energy was pinned, in which satisfies the constraint of charge neutrality. The details of the statistical model to pin Fermi energy and to estimate defect and carrier concentrations were explained in section 4.2. This procedure was utilized to explain the defect formation of V_2O_5 in the absence of Sn doping (section 4.3) and in the presence of Sn doping (section 4.4) to realize the effect of Sn doping on the formation of defects and carriers.

4.2 Computational methods

4.2.1 Defect concentrations at annealing

Previously, the formation energies of point defects as well as the lowest-energy species are depending on the position of Fermi energy. In order to pin the position of Fermi energy under thermodynamic equilibrium, the procedure as proposed recently was used (Buckeridge, 2019). In fact, the equilibrium Fermi

energy and defect concentration at a given experimental condition can be estimated by imposing the constraint of charge neutrality when the total concentration of electrons, from both donors and thermal excitation, is equaled to the total concentration of holes, from both acceptors and thermal excitation, i.e.

$$n_e - n_h + \sum_i N_i \cdot q_i = 0. \quad (4.1)$$

Here, n_e (n_h) is the concentration of electron (hole) generated from thermal excitation which can be expressed by using the statistical equations:

$$n_e = \int_{E_g}^{\infty} f_e(E) D(E) dE, \quad (4.2)$$

$$n_h = \int_{-\infty}^0 (1 - f_e(E)) D(E) dE, \quad (4.3)$$

where $f_e(E) = \left[1 + \exp\left(\frac{E_F - E}{kT}\right)\right]^{-1}$ is the Fermi-Dirac distribution. E_g is energy band gap, and $D(E)$ is the density of state per unit volume. The zero of energy scale is set at VBM. In addition, the concentration of a point defect specie X_i at charge stage q denoted as $N_i(X_i^q)$ for both donors and acceptors can be estimated by

$$N_i(X_i^q) = N_i^0 \exp\left(-\frac{E^f(X_i^q)}{kT}\right), \quad (4.4)$$

when N_i^0 is the concentration of possible sites that the defect can be incorporated.

From above equations, the concentration of each point defect depends on formation energy with respect to Fermi energy E_F . Thus, one can use a numerical method to self-consistently solve the position of equilibrium Fermi energy that satisfy the constraint of charge neutrality. As a result, one can achieve the equilibrium Fermi energy and defect concentrations under thermodynamic equilibrium at a given

temperature and experimental condition. In this case, the effect of temperature on energy band gap and volumetric expansion of the material can be neglected for simplicity. In fact, the experiment proposed the indirect band gap that can be varied between 2.14 eV (300 K) and 2.07 (650 K) (Basu *et al.*, 2016).

It is noted for Sn-related defects, the DFE of Sn-related defects are relatively high compared to the dominant intrinsic defects under thermodynamic equilibrium of μ_{Sn} . As a result, the calculated doping limit is dramatically small in the magnitude of 10^{12} cm^{-3} or $10^{-8} \%$. This finding is contrast to experiments where Sn can be normally doped around 1-5% even up to 10% or in the order of 10^{20} cm^{-3} (Rajeshwari *et al.*, 2018). However, Sn atoms are proposed to serve as nucleation center of V_2O_5 formation (Li *et al.*, 2013). This might be the reason why Sn atoms can be incorporated more than the calculated doping limit. Therefore, the concentrations of Sn-related defects were estimated in different way by controlling and varying the Sn doping concentrations. The concentrations of all Sn-related defects in various charge state are first calculated normally based on their DFE. Then, they are normalized with a given Sn doping concentration. It should be emphasized that the normalization was applied to achieve the desired doping concentration related to experiments. Note that the method implemented in a previous study (Komsa and Krasheninnikov, 2015) was followed.

In the calculation of defect and carrier concentration, the temperature is a key parameter which was defined as the experimental growth condition. As previously mentioned, the temperature of 723 K was set for all calculations to reproduce the annealing temperature in conventional growth of Sn-doped V_2O_5 . The defect and carrier concentrations were reached thermodynamic equilibrium at 723 K.

4.2.2 Defect concentrations after quenching

Although V_2O_5 is annealed at high temperature e.g. 723 K, the material is normally operated under an ambient condition. After quenching to the operating temperature e.g. 300 K, the populations of defect and carrier are redistributed into new equilibrium. In fact, the numbers of h^+ , e^- and even η^- from thermal excitation are decreasing with temperature. Whereas the total summation of all charge states for each defect specie was assumed to be fixed at the annealing temperature because the required kinetic energy for defect reorganization are usually large. However, the ratio between different charge states should be renormalized by the new DFE after shifting of Fermi energy. To renormalize, the concentration of defect X at charge state q , $N(X^q)$, is derived by

$$N(X^q) = \frac{\exp\left(-\frac{E^f(X^q)}{kT}\right)}{\sum \exp\left(-\frac{E^f(X^{q'})}{kT}\right)} N(X) \quad (4.5)$$

where $N(X)$ is total concentration of defect X and q' runs over all possible charges.

4.3 Defect concentrations in the absence of tin doping

To realize the effect of Sn doping on the formation of defects and carriers, the defect concentration occurring in the system without Sn doping compared that with Sn doping were therefore calculated. In this section, the system without Sn doping was first have a look. The calculated DFE of all considering intrinsic defects were used as inputs for the statistical model, and then solved for the concentration together with equilibrium Fermi energy using the procedure as mentioned in previous section. The temperature was set to be 723 K and 300 K for the annealed and quenched

conditions, respectively. The calculated Fermi energy and concentration of several intrinsic defects at different charge states under thermodynamic equilibrium at annealed and quenched conditions are reported as a bar chart in Figure 4.1.

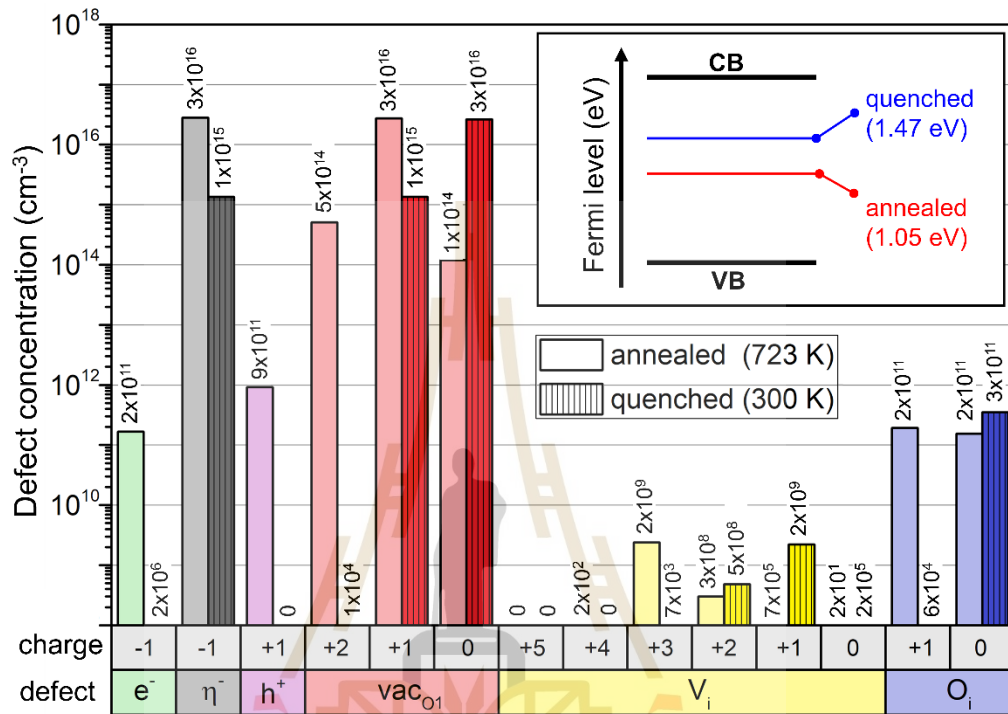


Figure 4.1 Illustration of the concentrations of some selected defects and carriers at different charge states occurred under thermodynamic equilibrium in the material without Sn doping at annealing temperature of 723 K (unfilled bars) and quenching into 300 K (filled bars). The inset shows equilibrium Fermi energy of the system under annealed and quenched conditions.

At the annealing temperature, the equilibrium Fermi energy around 1.05 eV above VBM is satisfied the constraint of charge neutrality. The unfilled bars in Figure 4.1 show the concentrations of selected defects and carriers in various charge states at annealed condition. Among all considering defects, vac_{O1} shows the highest concentration especially in charge state +1 with the concentration around $3 \times 10^{16} \text{ cm}^{-3}$.

The concentrations of charge state +2 and 0 are slightly smaller at the level of 5×10^{14} and $1 \times 10^{14} \text{ cm}^{-3}$, respectively. Since the constraint of total charge, these positive charged defects, mostly contributed from $\text{vac}_{\text{O}1}$ at charge +1, are totally compensated by η^- . As a result, the concentration of η^- is equaled to that of $\text{vac}_{\text{O}1}$ at charge state +1. In addition, the concentrations of other intrinsic defects are significantly lower than $\text{vac}_{\text{O}1}$ and η^- . The concentrations of O_i and V_i are moderately low at the magnitude of 10^{11} and 10^9 cm^{-3} , whereas those of other vacancies, i.e., $\text{vac}_{\text{O}2}$, $\text{vac}_{\text{O}3}$, vac_{V} and $\text{vac}_{\text{V}0}$ are negligible. Also, the concentrations of free carriers like h^+ and e^- are not comparable to η^- . Thus, the $\text{vac}_{\text{O}1}$ and the compensating η^- are indicated as the dominant defects in the system without impurity.

During quenching, the charge states of each defect specie are redistributed when the temperature is rapidly decreased to the ambient temperature (300 K) in order to approach into new equilibrium. In this case, the new equilibrium is reached at Fermi energy of 1.47 eV above VBM, which is considered as *n*-type semiconductor. The increase in Fermi energy is lowering the charge states of $\text{vac}_{\text{O}1}$. In fact, almost $\text{vac}_{\text{O}1}$ are stable in neutral charge state with the concentration of $3 \times 10^{16} \text{ cm}^{-3}$ as shown in the filled bar in Figure 4.1. The concentrations of single donor $\text{vac}_{\text{O}1}$ and the compensating η^- are dropped to $1 \times 10^{15} \text{ cm}^{-3}$, while the double donor $\text{vac}_{\text{O}1}$ is totally disappeared. In addition, the concentration of h^+ and e^- after quenching is negligibly small. Thus, it can be implied that the electrical conductivity in V_2O_5 is not contributed by the conduction of neither h^+ nor e^- . Instead, the unbound η^- or the bound polaron in neutral $\text{vac}_{\text{O}1}$ with higher concentration has more potential to be the prominent charge carriers for this *n*-type semiconducting V_2O_5 .

4.4 Defect concentrations in the presence of tin doping

In this section, the formation of point defects and charge compensation mechanism in Sn-doped V_2O_5 were studied. Like the previous section, the calculated DFE of all considering intrinsic defects and Sn-related defects were used as inputs for the statistical model in order to solve for the defect concentrations and equilibrium Fermi energy. In addition, the Sn concentration was controlled and varied up to 8% (more than 10^{21} cm^{-3}). The equilibrium Fermi energy and concentration of dominant intrinsic defects and Sn-related defects under thermodynamic equilibrium at annealed and quenched conditions are illustrated in Figure 4.2.

The explanation is divided into three scenarios based on the Sn doping concentration. Firstly, at diluted limit, Sn doping does not affect vac_{O1} and η^- formation when Sn concentration is less than 10^{16} cm^{-3} which is the concentration of vac_{O1} . The concentration and equilibrium Fermi energy is similar to the material without doping as shown in Figure 4.2(a-b). Almost Sn dopants are formed as Sn_{VO} with charge state +1 under annealing temperature. However, the neutral Sn_{VO} becomes more stable after quenching due to shifting of equilibrium Fermi energy from 1.05 to 1.47 eV. Secondly, when Sn doping concentration is in range of 10^{16} and 10^{20} cm^{-3} , the Fermi energy is gradually increasing with doping concentration from 1.05 to 1.50 eV. The positively charged Sn_{VO} is dominant donor which can be compensated by η^- . However, the concentration of negatively charged Sn_V rapidly increases, becoming the charge compensators instead of η^- when Sn doping concentration more 10^{19} cm^{-3} , resulting in the calculated concentration of Sn_{VO} in charge state +1 equals to that of Sn_V in charge state -1 as shown in Figure 4.2(d). Lastly, when the doping concentration is more than 10^{20} cm^{-3} (1%), the equilibrium

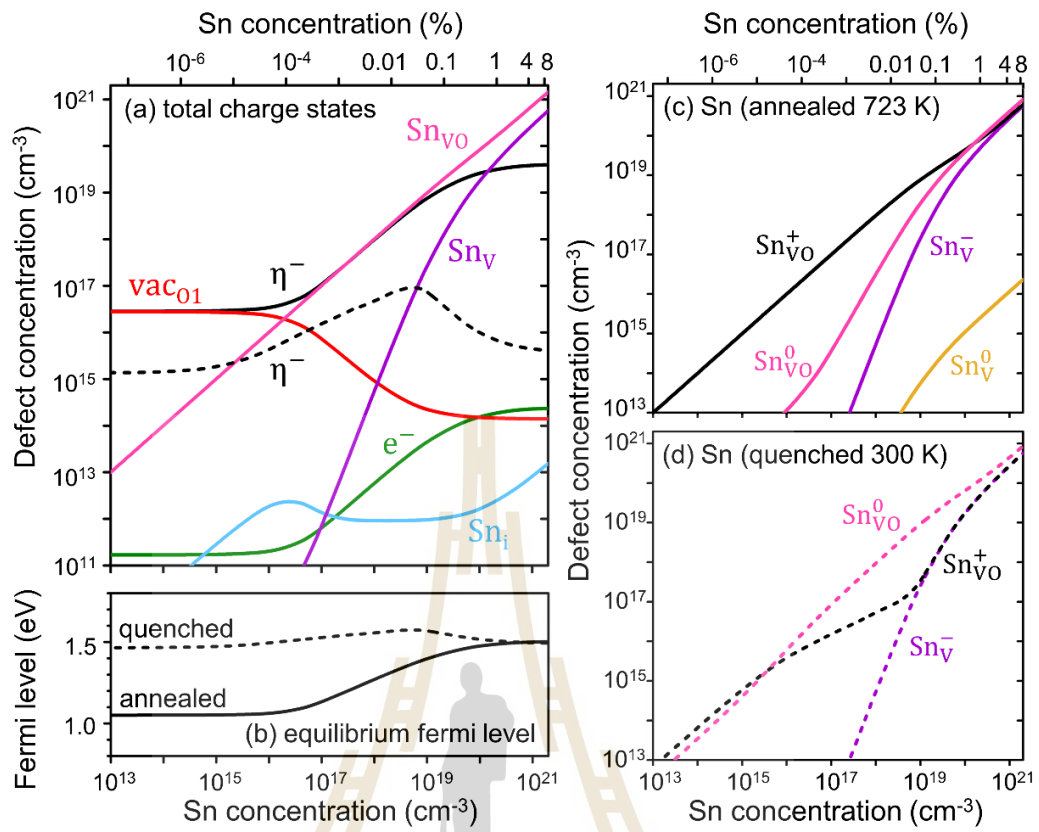


Figure 4.2 Illustrations of equilibrium defect concentration and Fermi energy as a function of Sn doping concentration under annealed (solid line) and quenched (dashed line) conditions. (a) all charged states concentration of selected defects and carriers. (b) equilibrium Fermi energy. (c-d) concentration of dominant Sn-related defects at various charge states under annealing (c) and quenching (d) temperature.

Fermi energy reaches the plateau at 1.50 eV. This Fermi energy is equivalent to the crossing point between DFE of positively charged Sn_{VO}^+ and negatively charged Sn_{V}^- as plotted in Figure 3.5(g). So that, all of Sn_{VO} in charge state +1 are self-compensated by Sn_{V} in charge state -1. In addition, the concentrations of both defects are more comparable to the neutral Sn_{VO}^0 after quenching. This is because the pinned Fermi energy approaches to the charge transition level between +1 and 0 state of Sn_{VO} as also shown in Figure 3.5(g).

Since the positively charged Sn_{VO} is compensated by the negatively charged Sn_{V} , the complex of both defects due to the electrostatic attraction was also considered, denoted as $[\text{Sn}_{\text{VO}} - \text{Sn}_{\text{V}}]$. In other words, this defect is equivalent to two single acceptors of Sn_{V} , and one double donor of vac_{O1} . The defect structure of $[\text{Sn}_{\text{VO}} - \text{Sn}_{\text{V}}]$ is shown in Figure 4.3. The lattice distortion around the defect is similar to the case of vac_{O1} and Sn_{VO} , but both apex-shared pyramids are Sn-centers instead of V-centers. The calculated PDOS shows electrically inactive behavior because there is no extra charge state inside the band gap, which is difficult to generate charge carriers. The DFE of this complex $[\text{Sn}_{\text{VO}} - \text{Sn}_{\text{V}}]$ is plotted as gray solid line in Figure 4.3[right]. This defect is stable only in the neutral charge state, which is consistent with the electrically inactive behavior. In addition, the complex formation can be claimed by the positive energy gain for the formation of defect pair compared to the isolated defects (i.e. $\text{Sn}_{\text{VO}} + \text{Sn}_{\text{V}} \rightarrow [\text{Sn}_{\text{VO}} - \text{Sn}_{\text{V}}]$) in the entire range of Fermi energy as shown in the dashed gray line. Moreover, this defect might be the origin of the Sn-O-Sn vibration peak with wavenumber around 600 cm^{-1} as reported in Fourier transform infrared spectroscopy (FTIR) of Sn-doped V_2O_5 material (Xing *et al.*, 2019). Moreover, this complex might accelerate the Li diffusion in the material due to the open up of the Li tunnel along b direction and the zero net charge without formation of polaron which do not interact with the intercalated Li-ion or coupled polaron. Although, the complex defect is thermodynamically more favorable than the isolated Sn_{VO} and Sn_{V} , the kinetics of the defect formation is not considered. Indeed, it is possible to find the isolated defects due to the configurational entropy or the possibility of both defects interacting with each other.

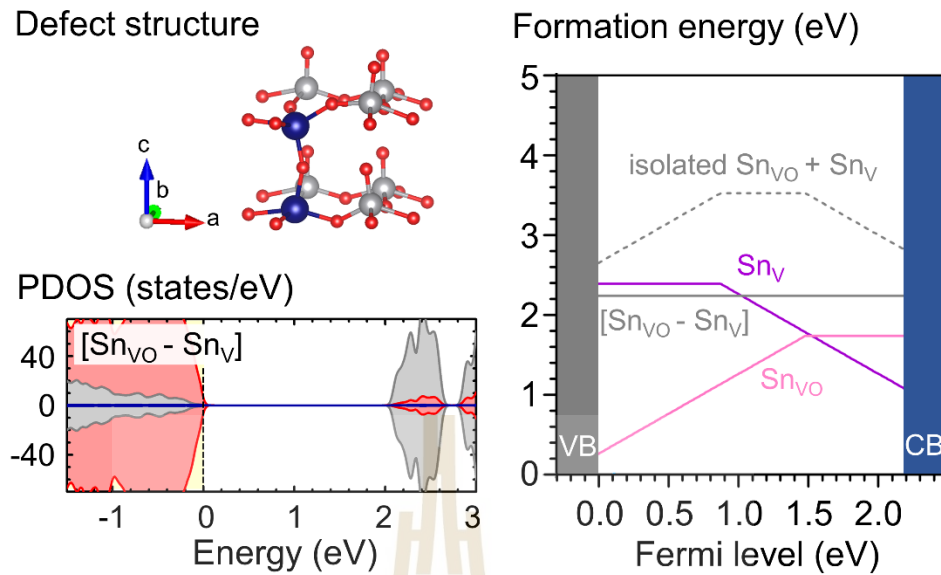


Figure 4.3 Defect structure (near defect region) of neutral complex defect between Sn substitution for V and Sn substitution for VO denoted as $[\text{Sn}_{\text{VO}} - \text{Sn}_{\text{V}}]$. The corresponding PDOS and defect formation energy of the complex are also plotted.

We noticed that the Sn_i is not likely to occur due to lack of the charge compensating defects. The concentration of Sn_i is less than 10^{13} cm^{-3} even in the high Sn doping content. In general, Sn doping concentration is around 0.1 up to 8%. With this significantly high doping concentration, Sn dopant are formed as the third scenarios where neutral Sn_{VO} is the main contribution. The positively charged Sn_{VO} , the compensating Sn_{V} and their complex are also occurred in the significantly high concentration. Moreover, the concentration of h^+ and e^- after quenching is negligibly small. Thus, it can be implied that the electrical conductivity in Sn-doped V_2O_5 should be contributed by the unbound η^- or the bound polaron in neutral Sn_{VO} with higher concentration. The positively charged Sn_{VO} , the negatively charge Sn_{V} and their complex are electrically inactive and cannot contribute the charge carriers.

4.5 Discussion

In this chapter, the statistical model was employed to estimate the equilibrium Fermi energy and concentration of defect based on the calculated DFE for the V_2O_5 materials in the absence and presence of Sn doping. In both cases, the concentrations of h^+ and e^- are negligible, which could be implied that the electron conduction is contributed by the unbound η^- or the bound polarons with significantly high concentration. In the absence of Sn doping, the concentration of bound polarons is around $3 \times 10^{16} \text{ cm}^{-3}$, in which the polarons are bound in neutral vac_{O1} . While the concentration of bound polarons in the presence of Sn doping is roughly Sn doping concentration, e.g., $1 \times 10^{20} \text{ cm}^{-3}$ for 1% of Sn doping, in which the polarons are bound in neutral Sn_{VO} . To emphasize, the Sn doping can control and increase the concentration of bound polarons in the V_2O_5 material. To contribute the electron conduction, these bound polarons must be escaped the defect center, resulting in unbound polaron and further hop throughout the materials. However, it is possible that the reaction occurred in the reverse direction where the unbound polaron is trapped by the defect center, vac_{O1} or Sn_{VO} in charge state +1, resulting in the neutral defect with bound polaron. In chapter V, the escaping of these bound polarons from defect centers and polaron hopping were investigated to explore the effect of Sn doping on electronic conductivity contributed from these bound polarons.

4.6 References

- Basu, R., Prasad, A. K., Dhara, S. and Das, A. (2016). Role of Vanadyl Oxygen in Understanding Metallic Behavior of $V_2O_5(001)$ Nanorods. **J. Phys. Chem. C.** 120: 26539.

- Buckeridge, J. (2019). Equilibrium Point Defect and Charge Carrier Concentrations in a Material Determined through Calculation of the Self-Consistent Fermi Energy. **Comput. Phys. Commun.** 244: 329.
- Komsa, H.-P. and Krasheninnikov, A. V. (2015). Native defects in bulk and monolayer MoS₂ from first principles. **Phys. Rev. B.** 91: 125304.
- Li, Y. W., Yao, J. H., Uchaker, E., Zhang, M., Tian, J. J., Liu, X. Y. and Cao, G. Z. (2013). Sn-Doped V₂O₅ Film with Enhanced Lithium-Ion Storage Performance. **J. Phys. Chem. C.** 117: 23507.
- Rajeshwari, S., Kumar, J. S., Rajendrakumar, R. T., Ponpandian, N. and Thangadurai, P. (2018). Influence of Sn ion doping on the photocatalytic performance of V₂O₅ nanorods prepared by hydrothermal method. **Mater. Res. Express.** 5: 13.
- Xing, L., Yu, Q., Bao, Y., Chu, J., Han, K., Chong, S., Lao, C.-Y., Lai, F., Li, P., Xi, K. and Wang, W. (2019). Strong (001) Facet-Induced Growth of Multi-Hierarchical Tremella-Like Sn-Doped V₂O₅ for high-performance potassium-ion batteries. **J. Mater. Chem. A.** 7: 25993.

CHAPTER V

POLARON CONDUCTION

5.1 Introduction

As briefly discussed in previous chapter, the electron conduction in V_2O_5 material in the absence and presence of Sn impurity could be originated the electron polaron rather than free electrons. This chapter dedicates on investigating and comparing the polaron conduction in the materials with and without Sn doping, which can be further implied to the role and effect of Sn dopant on the electron conduction. In section 5.2, the details about electron polarons as charge carriers for the polaron transport in the materials were discussed. Then, the computational method for polaron transport calculations are introduced in section 5.3. To identify the effect of Sn doping, the polaron transport in the pristine system, in the absence of Sn doping system, and in the presence of Sn doping system were explored in section 5.4 – 5.6. Subsequently, the discussion and comparison of these transport and associated electron conductivity are subjected in section 5.7.

5.2 Polarons as charge carriers

Electron transport in solids can be classified into two possible scenarios, which are i) the free diffusion of delocalized electrons as a band-like conduction and ii) the hop of localized electrons as a polaron conduction, or the combination of both

processes (Natanzon *et al.*, 2020). The first case can be approximately described by non-interacting electron transport in metals. On the other hand, the second case, the electrons are strongly interacted with their surrounding lattice vibrations, becoming localized electrons occupied in the trapped states near a potential well of cations so-called polarons. The polaron can be thermal excited leading to polaron hopping to the potential well of neighbor cations.

Based on the thermodynamic calculations of the defect formation in chapter III and IV, the band-like conduction is not dominant process for electron transport in both V_2O_5 and Sn-doped V_2O_5 . This is because the formation of free electrons is less favorable compared to that of electron polaron as shown in positive self-trapped energy in Figure 3.3(n). In addition, the dominant defects (neutral vac_{O1} and Sn_{VO} for the absence and presence of Sn doping system) in the materials are deep donor defects. In fact, the calculated CTL $\epsilon(+1/0)$ of vac_{O1} and Sn_{VO} $\epsilon(+1/0)$ are 1.40 and 1.49 eV, respectively. As a result, the concentration of free electron from the thermal excitation is negligibly low at 300 K. In contrast, the concentration of polarons are significantly high, in which the polarons are bound to the defect centers, i.e., vac_{O1} and Sn_{VO} . Therefore, it is expected that the charge transport mechanism of V_2O_5 is mainly occurred via polaron conduction based on thermally activated polaron hopping, as also reported in previous experiments and computations (Giannetta *et al.*, 2015; Ioffe and Patrino, 1970; Parija *et al.*, 2016; Prześniak-Welenc *et al.*, 2015; Suthirakun *et al.*, 2018; Watthaisong *et al.*, 2019).

Although the polarons are trapped to the defect centers, these polarons could be activated to overcome the attractive interaction, leading to the unbound polarons and the remaining single donors, i.e. positively charged vac_{O1} and Sn_{VO} . In other

words, the polaron in the lowest energy configuration could hop away from defect center and yield a donor vacancy and an unbound polaron. These unbound polarons are charge carriers for the polaron conduction. To account for the contribution of these bound polaron to the electronic conductivity in V_2O_5 with the absence and presence of Sn doping, the required energy for polaron transport was calculated in three different systems including pristine system, system without doping, and system with Sn doping.

5.3 Polaron transport calculations

Starting from the initial polaron configuration, which is the lowest energy configuration, the polaron can migrate to neighboring site in various crystallographic directions. Apart from the initial configuration, the other inequivalent configurations were constructed by creating the lattice distortion around the desired position (V-centers). The kinetics of polaron transport from the one site to the other neighboring site can be evaluated in term of energy barrier. In this work, the linear interpolation (LE) method, the simplest one, was used to estimate the barrier for all polaron migrations. Since, the LE method was employed to study the small polaron hopping in several oxides such as TiO_2 (Deskins and Dupuis, 2007), $LiFePO_4$ (Maxisch *et al.*, 2006), $BiVO_4$ (Pasumarthi *et al.*, 2019), CeO_2 (Sun *et al.*, 2017), and V_2O_5 (Suthirakun *et al.*, 2018; Watthaisong *et al.*, 2019).

In particular, the atomic coordinates are linearly interpolated between the initial and final configurations. Then, the energy profile along the hopping path is obtained through a set of single-point calculations as shown in Figure 5.1. In

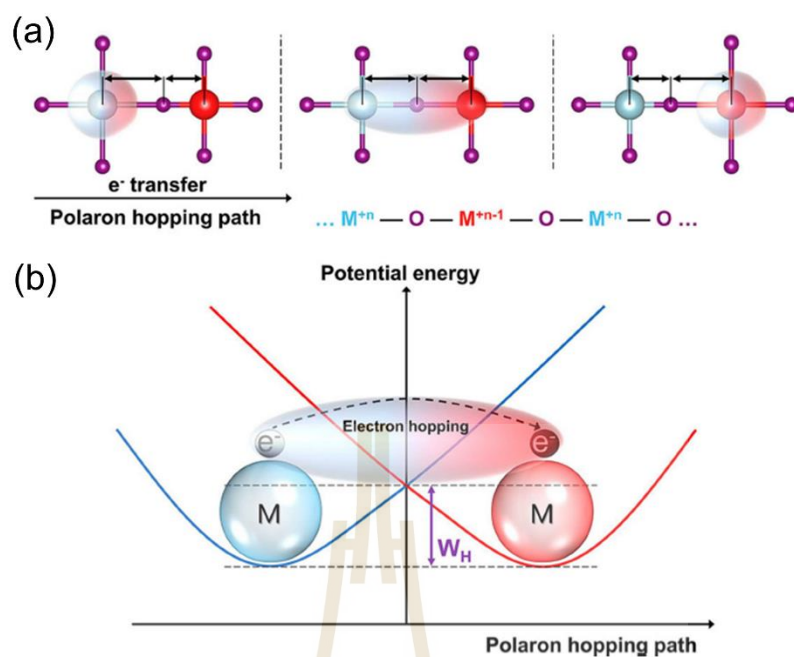


Figure 5.1 A schematic illustration of polaron transport in metal oxides. (a) lattice reorganization along the polaron hopping path from a M site to a neighboring M site, illustrating the change of bond length due to Coulombic force induced by electron charge. (b) Energy profile of the polaron hopping process between two M sites with respect to geometric configuration. W_H represents the energy required to generate the geometric configuration that suitable for hopping, i.e., transition state (Natanzon *et al.*, 2020).

nonadiabatic hopping, the hopping barrier is defined at the crossing point of two parabola energy curves where polaron located at initial and final sites as reported in the previous work (Pasumarthi *et al.*, 2019). Note that the LE method provides estimations of the hopping barriers that neglects the corrections due to electronic coupling constant (Liao *et al.*, 2011). Nevertheless, this work mainly focuses on qualitative trends rather than quantitative predictions. In fact, the purpose of this work is to compare hopping barriers of equivalent paths between three systems. In this

regard, the LE method could capture the major changes of lattice distortion along the reaction coordinate of polaron transfer, which is good enough for comparative studies of the polaron transport.

5.4 Polaron transport in pristine system

Various polaron migration paths and their barriers in pristine V_2O_5 was extensively elucidated in a previous work (Wattthaisong *et al.*, 2019). Nevertheless, in this thesis, all hopping barriers were revisited to consistently compare the calculated barriers with those of other systems. A $1 \times 3 \times 3$ supercell of V_2O_5 containing one electron polaron was utilized as a model to examine the polaron transport in pristine system. As shown in Figure 5.2, the polaron hopping from the initial site (I) to the four inequivalent nearest neighboring sites (A-D) along [100], [010], [001], and [110] directions are considered, denoted as *a*-, *b*-, *c*-, and *ab*-directions. The hopping barriers of the polaron toward A, B, C, and D sites are 0.10, 0.22, 0.28, and 0.21 eV, respectively. Although the hopping barriers in *a*-direction (A site) is significantly lower than that of the other directions, the next hopping must overcome the higher hopping barriers along *ab*- or *b*-direction due to the discontinuity of the structure in *a*-direction. Overall, the most favorable migration path is in-plane and along the *b*-direction which can either be i) consecutive hopping in *ab*-direction (0.21 eV) in a zigzag manner or ii) direct hopping in the *b*-direction (0.22 eV), as shown in Figure 5.2. Noted that Climbing Image Nudge Elastic Band (CI-NEB) method was also employed to calculate the energy barriers of some hopping path compared to the LE method. Computations reveal that the LE method provides quite good agreement with the CI-NEB-calculated barriers in the *a*-direction (0.10 vs. 0.09 eV) and *b*-direction

(0.22 vs. 0.24 eV). In this regard, it can be implied that the LE method could capture the major changes of lattice distortion along the reaction coordinate of polaron transfer, e.g. the changes of V-O bond lengths of the polaronic sites. These results agree very well with the previous computational work (Wattthaisong *et al.*, 2019) and experimentally obtained values of 0.28 and 0.23 eV (Giannetta *et al.*, 2015; Przeźniak-Welenc *et al.*, 2015).

In addition, the electron occupations of the two V-centers involving in the hopping process were considered. For the hopping in *a*-direction, the electron occupations of the two V centers gradually changes along the hopping coordinate which imply strong electronic coupling between initial and final polaronic sites via bridging O2. Such hopping behavior is considered an adiabatic process (Sun *et al.*, 2017). In contrast, for the hopping in other directions, the electron occupies either initial or final polaronic site along the reaction coordinate indicating the nonadiabatic behavior of electron transfer (Sun *et al.*, 2017). The nonadiabatic hopping in V₂O₅ is also reported elsewhere (Giannetta *et al.*, 2015; Suthirakun *et al.*, 2018).

Table 5.1 The reaction energy (ΔE), the associated energy barriers for forward direction (E_a) and reverse direction (E_r) of polaron migration in pristine system.

Path	ΔE (eV)	E_a (eV)	E_r (eV)	Direction
I - A	0.00	0.10	0.10	[100]
I - B	0.00	0.22	0.22	[010]
I - C	0.00	0.28	0.28	[001]
I - D	0.00	0.21	0.21	[110]

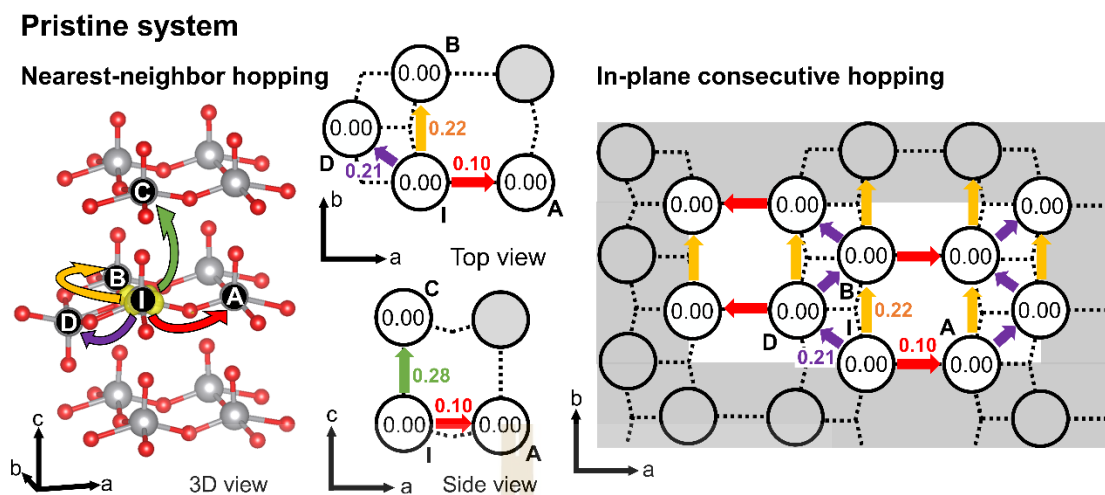


Figure 5.2 A schematic illustration of polaron migration paths in pristine system. The diagrams display the [left] nearest-neighbor and [right] in-plane consecutive hopping. The numbers in circles are energies relative to the configuration I where the polaron located at initial site (I site). The numbers next to arrow indicate the hopping barriers. These numbers are equivalent to those in Table 5.1, and all energies are shown in eV.

5.5 Polaron transport in the absence of tin doping system

In this case, a supercell of V_2O_5 containing one neutral O1 vacancy (vac_{O1}) was utilized as a model to examine the polaron transport in the absence of Sn doping system. The initial configuration includes two polarons bound to the vac_{O1} defect site. To determine which polaron, the upper or lower one, is likely to hop away from the defect site, their hopping barriers and reaction energies were calculated when one polaron hops to the nearest-neighbor site while the other polaron remains intact. As shown in Figure 5.3(a-b) the lower polaron exhibits higher hopping barriers and reaction energies than those of the upper one in all considered directions. The calculated results indicate that it is energetically and kinetically more favorable for the upper polaron to hop away from the defect site. This result agrees with the calculated

PDOS of neutral $\text{vac}_{\text{O}1}$ as shown in Figure 3.3(m), where the upper polaron is at the higher energy state which is more activated and likely to become an unbound polaron.

The polaron hopping barriers of the upper polaron in this system are significantly higher than those in the pristine system. In particular, the migration to the D site, kinetically favorable in the pristine system, is least favorable in the $\text{vac}_{\text{O}1}$ system with the barrier of 0.47 eV. In the presence of $\text{vac}_{\text{O}1}$, the hopping barriers to B and C sites also increase to 0.43 and 0.36 eV, respectively. Among these migration paths, hopping along *a*-direction (A site) exhibits the lowest barrier of 0.19 eV. In addition, the subsequent steps of the in-plane hopping away from the defect region were considered. In Figure 5.3, the consecutive hopping diagram reveals the required energy for each migration and relative energy compared to defect site. For example, the migration from site I to site E could start with the hopping from the site I to site A with a small barrier of 0.19 eV. Then, the migration needs to overcome a second barrier of 0.34 eV to site E. Accounting for the relative energy between site I and site A of 0.15 eV, the effective barrier for the migration from site I to site E is $0.15 + 0.34 = 0.49$ eV. Likewise, the effective barrier for migration from site I to site F through site B is $0.33 + 0.13 = 0.46$ eV. The effective barrier for the hopping to other sites, e.g., H (B to H, $0.33 + 0.26 = 0.59$ eV) and G (F to G, $0.39 + 0.22 = 0.61$ eV) is around 0.6 eV. When the polaron locates at site D, E, F, G and H, its hopping barriers outward defect region resemble to those of the pristine system. In other word, if the polaron can overcome such a high barrier around 0.60 eV, it could leave the defect center and further migrate to the pristine region. Noted that the events of consecutive polaron hopping in the other V_2O_5 layer or across the layers are not considered due to the supercell-size limitation. The system includes three layers of V_2O_5 that the

polaron may spuriously interact with the defect of the periodic image which could lead to incorrectly calculated barriers.

Furthermore, the lower polaron binding with the defect center when the upper polaron is out of range, was also considered. The calculated binding energy of 1.09 eV indicates immobilization of the lower polaron. In addition, migration of polarons- vac_{O1} complex where two polarons and vac_{O1} moves in a coupled fashion were also studied. The CI-NEB method was employed to calculate minimum energy path for this complex migrated along each direction. As a result, the hopping barriers along a - (2.0 eV), b - (2.50 eV), and c - (1.80 eV) directions are extremely high, implying the sluggish kinetics of the defect complex. Thus, only one of the two polarons originated from vac_{O1} can escape from the trapping defect center to become an unbound polaron and be able to contribute the carrier concentrations in the material.

Table 5.2 The reaction energy (ΔE), the associated energy barriers for forward direction (E_a) and reverse direction (E_r) of polaron migration in the absence of Sn doping system which is modeled as the supercell containing a neutral O1 vacancy.

The lower polaron in O1-vacancy system

path	ΔE (eV)	E_a (eV)	E_r (eV)	direction
I - A	0.33	0.39	0.06	[100]
I - B	0.52	0.54	0.02	[010]
I - C	0.44	0.52	0.08	[001]
I - D	0.59	0.61	0.02	[110]

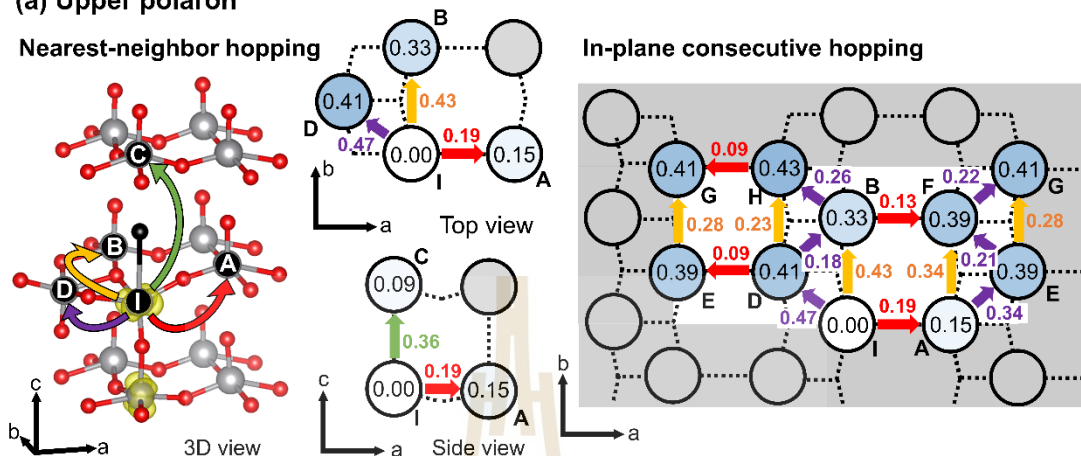
Table 5.2 (cont.) The reaction energy (ΔE), the associated energy barriers for forward direction (E_a) and reverse direction (E_r) of polaron migration in the absence of Sn doping system which is modeled as the supercell containing a neutral O1 vacancy.

The upper polaron of O1-vacancy system

path	ΔE (eV)	E_a (eV)	E_r (eV)	direction
I - A	0.15	0.19	0.04	[100]
I - B	0.33	0.43	0.10	[010]
I - C	0.09	0.36	0.27	[001]
I - D	0.41	0.47	0.06	[110]
A - E	0.24	0.34	0.10	[110]
A - F	0.24	0.34	0.10	[010]
B - F	0.06	0.13	0.07	[100]
B - H	0.10	0.26	0.16	[110]
D - B	-0.08	0.18	0.26	[110]
D - E	-0.02	0.09	0.11	[100]
D - H	0.01	0.23	0.22	[010]
E - F	0.00	0.21	0.21	[110]
E - G	0.02	0.24	0.22	[010]
F - G	0.02	0.22	0.20	[110]
H - G	-0.01	0.09	0.10	[100]

Oxygen vacancy system

(a) Upper polaron



(b) Lower polaron

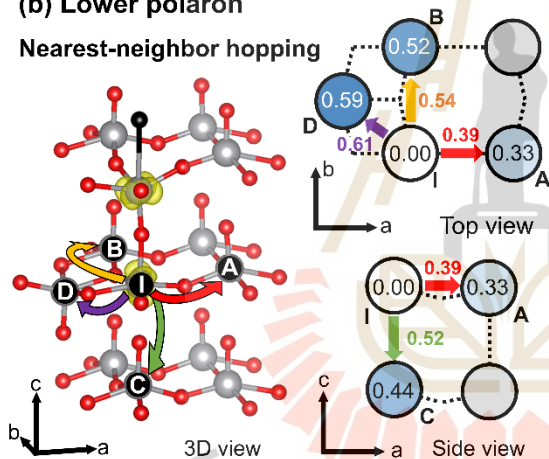


Figure 5.3 A schematic illustration of polaron migration paths in the absence of Sn doping system which is modeled as the supercell containing a neutral O1 vacancy. The diagrams display the [left] nearest-neighbor and [right] in-plane consecutive hopping. The numbers in circles are energies relative to the configuration I where the polaron located at initial site (I site). The numbers next to arrow indicate the hopping barriers. These numbers are equivalent to those in Table 5.2, and all energies are shown in eV.

5.6 Polaron transport in the presence of tin doping system

The analogous calculation for the presence of Sn doping system was investigated where a supercell of V_2O_5 containing one neutral Sn substitution for VO (Sn_{VO}) was utilized as a model to examine the polaron transport. To simplify the model, only the neutral Sn_{VO} which is the most dominant defect was considered and the others were neglected. Although the positively charged Sn_{VO} , the negatively charged or even their complex can be occurred in significantly high concentration, only neutral Sn_{VO} can generate the polaron to the system.

The calculated polaron hopping barriers of the polaron in this system are shown in Figure 5.4. In case of the polaron transport from the initial (I site) to the neighboring sites, the computation shows the similar trend of barriers of the system containing oxygen vacancy. In particular, the hopping along a -direction (A site) exhibits the lowest barrier of 0.20 eV. In the presence of Sn_{VO} , the energy barriers for the migration to the B and D sites are slightly lower by 0.03 eV compared to those in the vac_{O1} system. However, the downward polaron transport along c -direction shows the least favorable, which the energy barrier of 0.43 eV. In case of the upward hopping to Sn site, the migration barrier of 1.79 eV and relative energy of 0.78 eV are seriously large compared to other paths, so they are not included in Figure 5.4.

Furthermore, subsequent steps of the in-plane hopping away from the defect region were considered. In Figure 5.4, the consecutive hopping diagram reveals the required energy for each migration and relative energy compared to defect site similar to the case of vac_{O1} system. Compared to the vac_{O1} system, the energy barrier is generally lower by 0.03 eV for the hopping nearby defect region (from I and A sites) and by 0.01 eV for the farther region (from other sites). To calculate the effective

barrier of polaron hopping to consecutive sites, the analogous analysis was adopted. For instances, the effective barrier of the polaron hopping from initial site I to site E through site A is $0.16 + 0.30 = 0.46$ eV. Similarly, the effective barriers for hopping to other sites are 0.42 eV for F site (B to F), 0.56 eV for G (F to G), and 0.55 for H (B to H). If the polaron can overcome such a high barrier around 0.55 eV, it could leave the defect center and further migrate to the pristine region. It should be noted that the required energy for polaron escaping from the defect region to bulk region of the system with Sn doping is slightly lower than that of the system without doping.

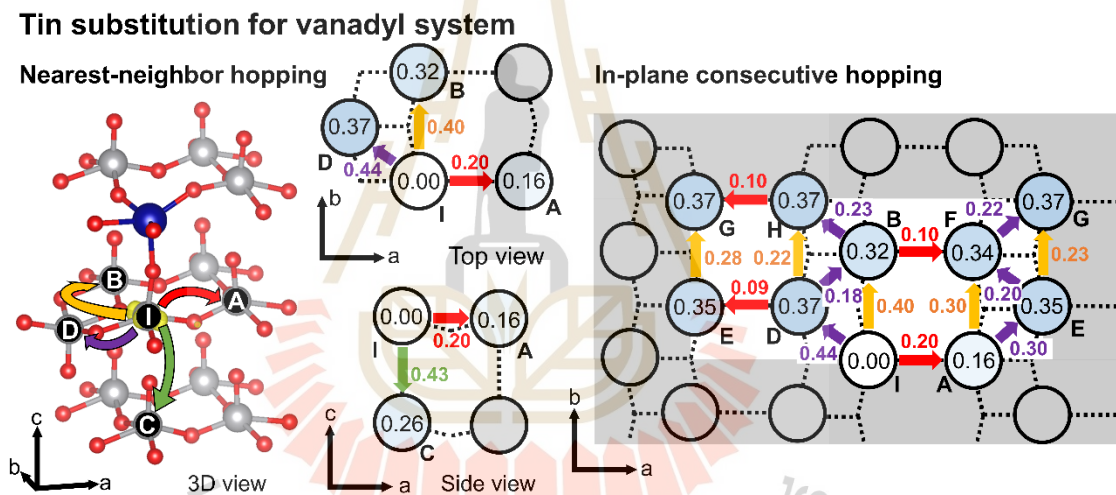


Figure 5.4 A schematic illustration of polaron migration paths in the presence of Sn doping system which is modeled as the supercell containing a neutral Sn substitution for VO. The diagrams display the [left] nearest-neighbor and [right] in-plane consecutive hopping. The numbers in circles are energies relative to the configuration I where the polaron located at initial site (I site). The numbers next to arrow indicate the hopping barriers. These numbers are equivalent to those in Table 5.3, and all energies are shown in eV.

Table 5.3 The reaction energy (ΔE), the associated energy barriers for forward direction (E_a) and reverse direction (E_r) of polaron migration in the absence of Sn doping system which is modeled as the supercell containing a neutral Sn substitution for VO.

path	ΔE (eV)	E_a (eV)	E_r (eV)	direction
O-A	0.16	0.20	0.04	[100]
O-B	0.32	0.40	0.08	[010]
O-C	0.26	0.43	0.17	[001]
O-D	0.37	0.44	0.07	[110]
A-E	0.19	0.30	0.11	[110]
A-F	0.18	0.30	0.12	[010]
B-F	0.02	0.10	0.08	[100]
B-H	0.05	0.23	0.18	[110]
D-B	-0.05	0.18	0.23	[110]
D-E	-0.02	0.09	0.11	[100]
D-H	0.00	0.22	0.22	[010]
E-F	0.00	0.20	0.20	[110]
E-G	0.02	0.23	0.21	[010]
F-G	0.03	0.22	0.19	[110]
H-G	0.00	0.10	0.10	[100]

5.7 Discussion

As stated in chapter IV, the material in the absence of Sn doping is dominant by neutral vac_{O1} with the concentration around $3 \times 10^{16} \text{ cm}^{-3}$. One neutral vac_{O1} provides two polarons strongly trapped by the defect center. The upper polaron, which is closer to oxygen vacancy site, has the potential to escape the potential well and become an unbound polaron. From the illustration in Figure 5.3, the energy of polaron located in the farthest V-center is higher than the lowest energy configuration by 0.41 eV. This value represents the depth of potential well that confine the polaron in the defect region, which can be implied to thermodynamics of polaron hopping away from defect center. In addition, if the polaron can overcome such a high barrier around 0.60 eV, it could leave the defect center and further migrate to the bulk region, becoming a charge carrier for polaron conduction. The illustration of these process and related parameters are demonstrated in Figure 5.5. The associated numbers, i.e., the polarons concentration (C_0), the depth of potential well (V), and the effective barrier for being unbound polaron (E_a) are also summarized in Table 5.4. Although the effective barrier of 0.60 eV is quite high, the moderate concentrations of vac_{O1} ($3 \times 10^{16} \text{ cm}^{-3}$) could provide a sufficient carrier concentration even at 300 K, as compared to the intrinsic polaron concentrations of $4.2 \times 10^4 \text{ cm}^{-3}$ generated from thermal activation. As a result, these carriers contribute the electron conduction in the V_2O_5 .

The material in the presence of Sn doping is dominant by neutral Sn_{VO} with the concentration around $1 \times 10^{20} \text{ cm}^{-3}$ for 1% doping concentration as example. In this case, there is only one bound polaron trapped by the defect center of Sn_{VO} . Similarly, the bound polaron is confined by the potential well depth of around 0.37 eV as shown

in Table 5.4. It can leave the defect center and further hop to the bulk region, if it overcomes the effective barrier of 0.55 eV, approximately. In the presence of Sn doping, not only that the concentration of bound polarons can be controlled and increased, but these polarons also have higher chances to escape from the trapped region as shown in the shallower of potential well and the smaller of effect barrier compared to the material in absence of Sn doping. In other words, Sn doping slightly weaken the interaction between the defect center and the bound polarons, and these polarons can leave out more easily. As a result, the number of charge carriers increase, and the electronic conductivity of the material can be improved by doping with Sn.

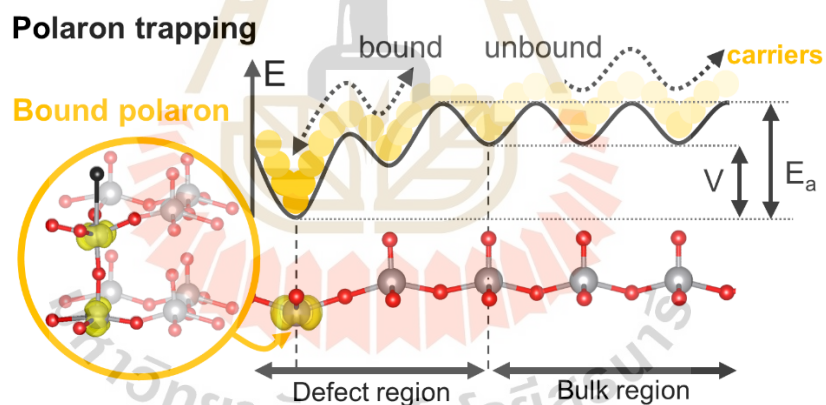


Figure 5.5 A schematic illustration of a bound polaron hop away from the defect center leads to an unbound polaron and a single donor. E_a represents the effective energy barrier for bound polaron hopping from the defect region to the bulk region. V represents the potential well of the defect region which is defined by the energy difference between polaron located in the defect center and polaron in the bulk region.

Table 5.4 The summary of important numbers, i.e., the polarons concentration (C_0), the depth of potential well (V), and the effective barrier for being unbound polaron (E_a) for the polaron transport in each system.

System	C_0 (cm ⁻³)	V (eV)	E_a (eV)
Pristine	4×10^4	0.00	0.21
Material in the absence of Sn doping	3×10^{16}	0.41	0.60
Material in the presence of Sn doping	1×10^{20}	0.37	0.55

5.7 References

- Deskins, N. A. and Dupuis, M. (2007). Electron Transport via Polaron Hopping in Bulk TiO₂: A Density Functional Theory Characterization. **Phys. Rev. B.** 75: 195212.
- Giannetta, H. M. R., Calaza, C., Lamas, D. G., Fonseca, L. and Fraigi, L. (2015). Electrical Transport Properties of V₂O₅ Thin Films Obtained by Thermal Annealing of Layers Grown by RF Magnetron Sputtering at Room Temperature. **Thin Solid Films.** 589: 730.
- Ioffe, V. A. and Patrino, I. B. (1970). Comparison of the Small-Polaron Theory with the Experimental Data of Current Transport in V₂O₅. **Phys. Status Solidi B.** 40: 389.
- Liao, P., Toroker, M. C. and Carter, E. A. (2011). Electron Transport in Pure and Doped Hematite. **Nano Lett.** 11: 1775.

- Maxisch, T., Zhou, F. and Ceder, G. (2006). Ab initio Study of the Migration of Small Polarons in Olivine LiFePO_4 and Their Association with Lithium Ions and Vacancies. **Phys. Rev. B.** 73: 104301.
- Natanzon, Y., Azulay, A. and Amouyal, Y. (2020). Evaluation of Polaron Transport in Solids from First-principles. **Isr. J. Chem.**: 20.
- Parija, A., Liang, Y., Andrews, J. L., De Jesus, L. R., Prendergast, D. and Banerjee, S. (2016). Topochemically De-Intercalated Phases of V_2O_5 as Cathode Materials for Multivalent Intercalation Batteries: A First-Principles Evaluation. **Chem. Mater.** 28: 5611.
- Pasumarthi, V., Liu, T., Dupuis, M. and Li, C. (2019). Charge Carrier Transport Dynamics in W/Mo-Doped BiVO_4 : First Principles-Based Mesoscale Characterization. **J. Mater. Chem. A.** 7: 3054.
- Przeźniak-Welenc, M., Szreder, N. A., Winiarski, A., Łapiński, M., Kościelska, B., Barczyński, R. J., Gazda, M. and Sadowski, W. (2015). Electrical Conductivity and Relaxation Processes in V_2O_5 Nanorods Prepared by Sol-Gel Method. **Phys. Status Solidi B.** 252: 2111.
- Sun, L., Huang, X., Wang, L. and Janotti, A. (2017). Disentangling the Role of Small Polarons and Oxygen Vacancies in CeO_2 . **Phys. Rev. B.** 95: 245101.
- Suthirakun, S., Genest, A. and Rösch, N. (2018). Modeling Polaron-Coupled Li Cation Diffusion in V_2O_5 Cathode Material. **J. Phys. Chem. C.** 122: 150.
- Wattthaisong, P., Jungthawan, S., Hirunsit, P. and Suthirakun, S. (2019). Transport Properties of Electron Small Polarons in a V_2O_5 Cathode of Li-ion Batteries: A Computational Study. **RSC Adv.** 9: 19483.

CHAPTER VI

CONCLUSIONS

In this thesis, the role of the Sn doping on the improved conductivity of V_2O_5 based cathode for Li-ion batteries was examined. The computational tools based on the DFT+U method coupled with the statistical model was utilized to explore impact of Sn dopant on (i) the formation and properties of point defect as well as charge carriers (ii) the transport of charge carriers implying to electronic conductivity of the material. The corresponding results in case of Sn-doped system was compared to those of the system without impurity, to indicate the effect of Sn dopant.

Firstly, the geometric, electronic, and thermodynamic properties of each individual point defects, including intrinsic and Sn-related defects, were investigated in systematic manner. The defect formation energy reveals that electron prefers to be localized so-called the electron polaron (η^-) rather than being a free particle. A deep donor defect of vanadyl oxygen vacancy (vac_{O1}) and the compensating electron polarons are the most dominant intrinsic defects in a wide range of Fermi energy. In the presence of Sn doping, three possibilities for Sn incorporation, i.e., Sn interstitial (Sn_i), Sn substitution for V (Sn_V), and Sn substitution for VO (Sn_{VO}), can be occurred depending on the position of Fermi energy. Note that the related parameters, e.g. chemical potentials, annealing temperature, and O_2 pressure, were set as a conventional growth condition of Sn-doped V_2O_5 .

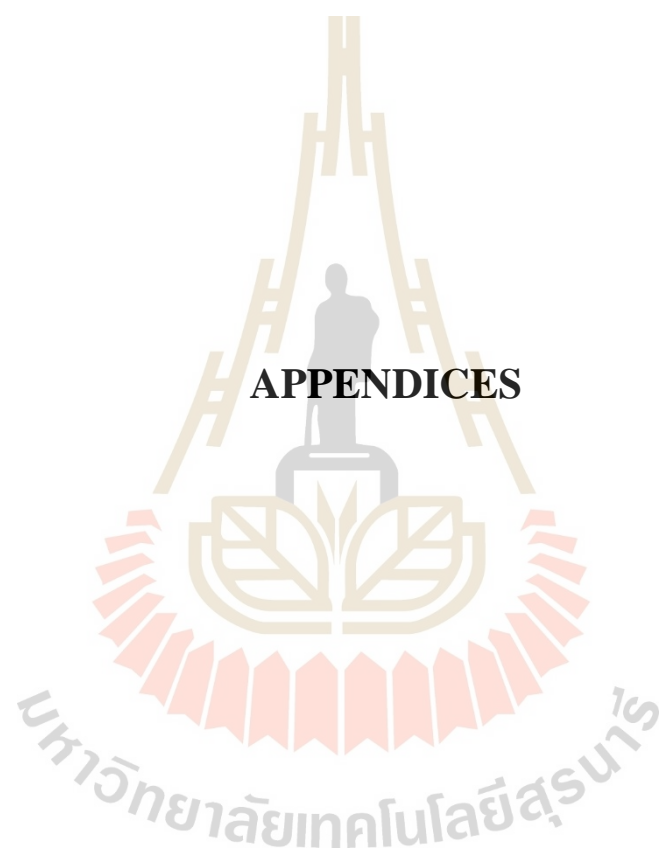
Next, the statistical model of defect and carrier concentrations with the constraint of charge neutrality was applied to pin the equilibrium Fermi energy and to estimate the defect and carrier concentration under thermodynamic equilibrium. As expected, neutral charge vac_{O1} is the most dominant defect with the concentration of $3 \times 10^{16} \text{ cm}^{-3}$, for the system in the absence of doping. Likewise, the neutral charge Sn_{VO} is the most dominant defect in the presence of Sn doping. For example, its concentration is $1 \times 10^{20} \text{ cm}^{-3}$ for 1% Sn doping. In both cases, the neutral charge defect also includes the positively charged defect center and the trapping polarons. To contribute the electron conduction, these bound polarons must hop away from the defect center, resulting in unbound polarons or charge carriers.

Finally, the polaron transport in the absence and presence of Sn doping system were therefore investigated. Starting from the initial configuration (defect center), the second or third step of outward polaron hopping resembles the polaron transport in the pristine, indicating the boundary of defect interaction. In the former case, only one of two bound polarons in vac_{O1} can escape the defect region by overcoming the energy of 0.60 eV to achieve the unbound polaron, whereas the polaron in Sn_{VO} require a slightly lower energy to conquer the barrier 0.55 eV for the latter case. Although the effective barriers of both cases are quite high, the material could provide sufficient carrier concentration due to the moderate or high concentration of the starting bound polarons. As a result, these carriers contribute the electron conduction in the V_2O_5 and Sn doped system.

In the presence of Sn doping, not only that the concentration of bound polarons can be controlled and increased, but these polarons also have higher chances to escape from the trapped region as shown in the shallower of potential well and the smaller of

effect barrier compared to the material in absence of Sn doping. In other words, Sn doping slightly weaken the interaction between the defect center and the bound polarons, and these polarons can leave out more easily. As a result, the number of charge carriers increase, and the electronic conductivity of the material can be improved by doping with Sn.

These findings can imply that the Sn doping plays a significant role in the increase in the concentration of bound polarons via the formation of neutral Sn_{VO} . In addition, these bound polaron can escape from the defect center more easily since the shallower potential well and smaller effective energy barrier for the hopping away from defect region compared to the material without doping. In other words, Sn substitution for V in O1 vacancy system slightly weaken the interaction between the defect center and the bound polarons. As a result, the number of charge carriers increase as well as the electronic conductivity of the Sn-doped material. This conclusion can explain the experimentally observed higher electronic conductivity of Sn-doped sample. This work provides the fundamental knowledge about formation of point defects and transport of charge carriers which could be helpful to the design of high-performance V_2O_5 based cathode for metal-ion batteries application.



APPENDICES

มหาวิทยาลัยเทคโนโลยีสุรนารี

APPENDIX A

TUNING U PARAMETER

Due to an imperfection of the standard DFT with an approximated exchange-correlation functional, a well-known self-interaction error causes the failure in predicting some properties of materials especially in transition metal oxides. The DFT+U method could provide more accurate results by including the strong on-site Coulomb interaction between the localized electrons. However, the calculated results are quite sensitive to the strength of U, so that it must be chosen carefully in order to properly describe the electronic structure and properties of native point defects. In practice, U parameter could be chosen by calibrating the calculated results with the experimental ones, and it would be differed for such a property.

For V₂O₅, a wide range of U (2.0 - 6.6 eV) was utilized for V-3d orbitals depending on the difference of interest properties (Das *et al.*, 2019; Lutfalla *et al.*, 2011; Scanlon *et al.*, 2008; Wang *et al.*, 2006). For instance, U = 2.0 and 3.1 eV was proposed by calibrating with overall reduction energy of vanadium oxides (Lutfalla *et al.*, 2011; Wang *et al.*, 2006). Similarly, U = 3.5 eV was nominated to provide a uniform description in overall structural parameters, band-gap energy, dielectric constant, and heat of enthalpy (Das *et al.*, 2019). In addition, Scanlon *et al.* (Scanlon *et al.*, 2008) suggested U of 4.0 eV for investigating the polaron formation of the reduced V₂O₅ via thermal reduction (oxygen vacancy) and chemical reduction

(lithium intercalation). In particular, the strength of U was calibrated with the position of polaronic state to band-gap energy ratio in experiment. This ratio might be an appropriate criterion for describing the polaronic behavior properly. However, their model does not concern about van der Waals interaction resulting in 10% error of c parameter, which might lead to an inaccuracy in polaron behavior and lithium intercalation due to the narrower of interlayer spacing. This error can be reduced to only 1.8% by the introducing the optPBE-vdw functional (Carrasco, 2014; Suthirakun, Genest, *et al.*, 2018; Suthirakun, Jungthawan, *et al.*, 2018).

In this work, the U value was parameterized by Scanlon's criteria with the implementation of van der Waals interaction based on the experimental data. Wu *et al.* (Wu *et al.*, 2005) studied the Li intercalation reaction in thin film V_2O_5 . When one intercalated Li atom is fully ionized and donates one electron to a neighboring V center, resulting in the reduction of V (V^{5+} becomes V^{4+}), becoming the electron polaron and producing a gap state. The polaronic state can be observed by ultraviolet photoemission spectroscopy (UPS) (Wu *et al.*, 2005). At the initial process i.e. low Li content, the polaronic state is found at around 1.2 eV above valence band maximum (VBM). This result leads us to the position of polaronic state to energy gap ratio around 0.5 for the experimental band gap of 2.4 eV (Hieu and Lichtman, 1981). This ratio was set for the criteria of parameterizing U in this work.

In order to calibrate U parameter, PBE+ U where U ranging from 2.0 – 6.0 eV was used for optimizing the crystal structure and calculating DOS of pristine and Li-intercalated V_2O_5 ($Li_{0.056}V_2O_5$). From the calculated DOS of Li-intercalated V_2O_5 , the position of the mid gap state dramatically decreases as an increase in U whereas the band-gap energy from the pristine DOS steadily increases. Table A.1 shows the trend

of calculated results compared to previous calculations and experiment. Also, the positions of polaronic state and band gap energies as well their ratios are plotted as a function of U as shown in Figure A.1. The experimental ratio around 0.5 is matched to the calculated one at U around 3.5 eV. So, the appropriate U of 3.5 eV was selected to properly describe the polaronic states in this work. It should be noted that this number of U is also reported to be a better choice for explaining the structural parameters, band-gap energy, dielectric constant, and heat of enthalpy of V_2O_5 (Das *et al.*, 2019).

Table A.1 The calculated structural parameters (lattice constants and bond lengths), band gap energy, and the position of polaronic state position compared with the experimental result.

U (eV)	This work PBE+U/optPBE					Scanlon PBE+U	Carrasco PBE+U/ optPBE	Das PBE+U/ D3	Exp.
	2.0	3.0	3.5	4.0	6.0	4.0	4.0	3.5	
a	11.667	11.666	11.665	11.669	11.675	11.496	11.690	11.628	11.510
b	3.598	3.613	3.621	3.629	3.656	3.630	3.628	3.615	3.563
c	4.447	4.446	4.447	4.435	4.454	4.804	4.423	4.359	4.369
V-O ₁	1.606	1.609	1.610	1.611	1.616	1.602	1.620	1.602	1.585
V-O ₂	1.800	1.804	1.806	1.808	1.817	1.805	1.810	1.798	1.780
V-O ₃	1.900	1.906	1.909	1.912	1.924	1.915	1.912	1.902	1.878
	2.049	2.045	2.043	2.041	2.036	2.018	2.046	2.034	2.021
E _g (eV)	1.98	2.11	2.18	2.25	2.58	2.26	2.26	2.18	2.4
polaronic state(eV)	1.89	1.31	1.09	0.85	0.20	0.91	-	-	1.2
ratio	0.95	0.62	0.50	0.38	0.08	0.41	-	-	0.5

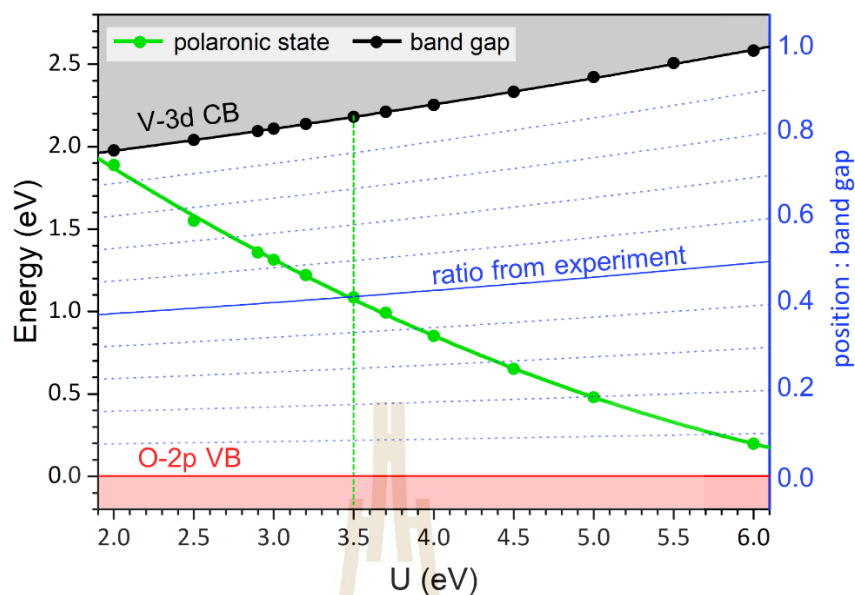


Figure A.1 Illustration of the position of polaronic state of Li-intercalated V_2O_5 and band gap energy of pristine V_2O_5 as a function of U parameters ranging from 2.0 to 6.0 eV. The calculated position of state to band gap ratio is also plotted with the experimental ratio (dotted line) in order to calibrate the appropriate U parameter.

References

- Carrasco, J. (2014). Role of Van der Waals Forces in Thermodynamics and Kinetics of Layered Transition Metal Oxide Electrodes: Alkali and Alkaline-Earth Ion Insertion into V_2O_5 . **J. Phys. Chem. C.** 118: 19599.
- Das, T., Tosoni, S. and Pacchioni, G. (2019). Structural and Electronic Properties of Bulk and Ultrathin Layers of V_2O_5 and MoO_3 . **Comput. Mater. Sci.** 163: 230.
- Hieu, N. V. and Lichtman, D. (1981). Bandgap Radiation Induced Photodesorption from V_2O_5 Powder and Vanadium Oxide Surfaces. **J. Vac. Sci. Technol.** 18: 49.
- Lutfalla, S., Shapovalov, V. and Bell, A. T. (2011). Calibration of the DFT/GGA plus U Method for Determination of Reduction Energies for Transition and Rare

- Earth Metal Oxides of Ti, V, Mo, and Ce. **J. Chem. Theory Comput.** 7: 2218.
- Scanlon, D. O., Walsh, A., Morgan, B. J. and Watson, G. W. (2008). An ab initio Study of Reduction of V_2O_5 through the Formation of Oxygen Vacancies and Li Intercalation. **J. Phys. Chem. C.** 112: 9903.
- Suthirakun, S., Genest, A. and Rösch, N. (2018). Modeling Polaron-Coupled Li Cation Diffusion in V_2O_5 Cathode Material. **J. Phys. Chem. C.** 122: 150.
- Suthirakun, S., Jungthawan, S. and Limpijumnong, S. (2018). Effect of Sn-Doping on Behavior of Li-Intercalation in V_2O_5 Cathode Materials of Li-Ion Batteries: A Computational Perspective. **J. Phys. Chem. C.** 122: 5896.
- Wang, L., Maxisch, T. and Ceder, G. (2006). Oxidation Energies of Transition Metal Oxides within the GGA+U Framework. **Phys. Rev. B.** 73: 195107.
- Wu, Q. H., Thißen, A. and Jaegermann, W. (2005). Photoelectron Spectroscopic Study of Li Intercalation into V_2O_5 Thin Films. **Surf. Sci.** 578: 203.

APPENDIX B

PUBLICATION AND PRESENTATIONS

B.1 List of publications

Ngamwongwan, L., Fongkaew, I., Jungthawan, S., Hirunsit, P., Limpijumnong, S., and Suthirakun, S. (2021). Electronic and Thermodynamic Properties of Native Point Defects in V_2O_5 : A First-Principles Study. **Phys. Chem. Chem. Phys.** (accepted on 21st February 2021).

Ngoipala, A., Ngamwongwan, L., Fongkaew, I., Jungthawan, S., Hirunsit, P., Limpijumnong, S., and Suthirakun, S. (2020). On the Enhanced Reducibility and Charge Transport Properties of Phosphorus-Doped $BiVO_4$ as Photocatalysts: A Computational Study. **J. Phys. Chem. C.** 124: 4352.

มหาวิทยาลัยเทคโนโลยีสุรนารี

B.2 List of presentations (poster)

Ngamwongwan, L., Jungthawan, S., and Suthirakun, S. (January 2019). First-Principles Study of the Defect Formation in Sn-Doped V_2O_5 for Li-ion Batteries. **The 2nd Taiwan-Thailand-Vietnam Workshop on Theoretical and Computational Chemistry (TTV2)**. Sirindhorn Science Home, Thailand Science Park, Pathum Thani, Thailand.

Ngamwongwan, L., Fongkaew, I., Jungthawan, S., Limpijumnong, S., and Suthirakun, S. (November 2019). Effect of Dopant in Sn-doped V_2O_5 for Li-ion Batteries: A First-principles Calculation. **The International Centre for Theoretical Physics (ICTP) Asian Network School and Workshop on Complex Condensed Matter Systems 2019**. National Institute of Physics, University of Philippines Diliman, Quezon city, Philippines.

PCCP



PAPER

View Article Online
View Journal

Check for updates

Cite this: DOI: 10.1039/d0cp06002j

Electronic and thermodynamic properties of native point defects in V_2O_5 : a first-principles study†

Lappawat Ngamwongwan,^{abc} Ittipon Fongkaew,^{abc} Sirichok Jungthawan,^{abc} Pussana Hirunsit,^d Sukit Limpijumnong^{ef} and Suwit Suthirakun^{fg} *^{eg}

The formation of native point defects in semiconductors and their behaviors play a crucial role in material properties. Although the native defects of V_2O_5 include vacancies, self-interstitials, and antisites, only oxygen vacancies have been extensively explored. In this work, we carried out first-principles calculations to systematically study the properties of possible native defects in V_2O_5 . The electronic structure and the formation energy of each defect were calculated using the DFT+ U method. Defect concentrations were estimated using a statistical model with a constraint of charge neutrality. We found that the vanadyl vacancy is a shallow acceptor that could supply holes to the system. However, the intrinsic p-type doping in V_2O_5 hardly occurred because the vanadyl vacancy could be readily compensated by the more stable donor, i.e., the oxygen vacancy and oxygen interstitial, instead of holes. The oxygen vacancy is the most dominant defect under oxygen-deficient conditions. However, under extreme O-rich conditions, a deep donor of oxygen interstitial becomes the major defect species. The dominant oxygen vacancy under synthesized conditions plays an important role in determining the electronic conductivity of V_2O_5 . It induces the formation of compensating electron polarons. The polarons are trapped at V centers close to the vacancy site with the effective escaping barriers of around 0.6 eV. Such barriers are higher than that of the isolated polaron hopping (0.2 eV). The estimated polaron mobilities obtained from kinetic Monte Carlo simulations confirmed that oxygen vacancies act as polaron-trapping sites, which diminishes the polaron mobility by 4 orders of magnitude. Nevertheless, when the sample is synthesized at elevated temperatures, a number of thermally activated polarons in samples are quite high due to the high concentrations of oxygen vacancies. These polarons can contribute as charge carriers of intrinsic n-type semiconducting V_2O_5 .

Received 19th November 2020,
Accepted 21st February 2021

DOI: 10.1039/d0cp06002j

rsc.li/pccp

1. Introduction

Vanadium pentoxide (V_2O_5) has attracted significant attention from researchers due to its unique structural and electrochemical

properties. It has been used in a wide range of applications such as oxidation catalysts,^{1,2} metal-ion batteries,^{3–6} supercapacitors,^{7,8} gas sensors,^{9–12} electrochromic devices,^{13,14} and thermoelectric materials.^{8,15} Its stable layered structure with possible multi-valent vanadium has a large affinity for accommodating the various kinds of defects. In particular, native defects created under the synthesized environment play an important role in determining the properties and activities of V_2O_5 hosts. For example, the presence of oxygen vacancies can alleviate the sluggish electrical conductivity and low Li-ion diffusivity of V_2O_5 -based cathode for Li-ion batteries.^{16,17} The cation vacancy in V_2O_5 can also improve the Li-ion capacity.¹⁸ One report suggests that oxygen vacancy improves the sensitivity of NO_2 gas sensors because it generates lower valence vanadium (V^{4+}), which is the active species in the sensing mechanism.¹² In the case of metal oxide catalysts, the ease of oxygen vacancy formation can be attributed to the more aggressive oxidant.¹⁹ Hence, understanding the formation of native point defects, in particular, oxygen vacancies and their behaviors is of crucial importance for designing promising V_2O_5 -based functional materials.

^a School of Physics, Institute of Science, Suranaree University of Technology, Nakhon Ratchasima 30000, Thailand

^b Center of Excellence in Advanced Functional Materials, Suranaree University of Technology, Nakhon Ratchasima 30000, Thailand

^c Thailand Center of Excellence in Physics, Ministry of Higher Education, Science, Research and Innovation, Bangkok 10400, Thailand

^d National Nanotechnology Center (NANOTEC), National Science and Technology Development Agency (NSTDA), 111 Thailand Science Park, Pathum Thani 12120, Thailand

^e Research Network NANOTEC – SUT on Advanced Nanomaterials and Characterization, Suranaree University of Technology, Nakhon Ratchasima 30000, Thailand. E-mail: suthirak@sut.ac.th

^f The Institute for the Promotion of Teaching Science and Technology (IPST), Bangkok 10110, Thailand

^g School of Chemistry, Institute of Science, Suranaree University of Technology, Nakhon Ratchasima 30000, Thailand

† Electronic supplementary information (ESI) available. See DOI: 10.1039/d0cp06002j

Native defects of V_2O_5 include vacancies, self-interstitials, and antisites. However, only oxygen vacancies have been extensively explored in both experimental and computational studies. Oxygen vacancies generated from a thermal reduction process were observed by several experimental techniques,^{20–23} where the magnetic,²⁴ optical,²³ and electronic²⁵ properties of V_2O_5 upon oxygen vacancy formation were studied. From the computational viewpoint, geometric and electronic structures induced by oxygen vacancies were extensively explored on both surface^{26–28} and bulk²⁹ models. The formation of an oxygen vacancy generated two extra electrons localized at the two neighboring vanadium centers.²⁹ The X-ray photoemission spectra (XPS) exhibited the gap state above the valence band, indicating the localization of electron polarons at particular vanadium centers where V^{5+} was then reduced to V^{4+} .³⁰ These localized electrons are accompanied by local lattice distortion, *i.e.*, the V–O bond lengthening of the polaronic center, which is of the reduced vanadium center as evidenced in the recent work.³¹ The electronic conductivity of the material originated from the thermally activated hopping of these polarons between vanadium centers, which is generally slower than that of the band conduction.^{23,32,33} It is generally believed that increasing the concentration of the reduced V^{4+} species can improve the electronic conductivity of materials.^{33,34}

As stated above, various experimental and computational approaches have been employed to study the nature of defects in several metal oxides including V_2O_5 .^{23,29,35–40} Among these methods, a first-principles approach based on density functional theory (DFT) has been considered a powerful tool to provide insight into the behavior of point defects in these materials.^{41–46} The DFT method can be used to obtain structural and electronic properties of several point defects and determine their relative stabilities under different environmental conditions.⁴⁰ For instance, one study examined the relative stabilities and electronic structures of defects in $\alpha\text{-Fe}_2\text{O}_3$. The computations showed that Fe at the interstitial site is responsible for electron donors, whereas the oxygen vacancy is mostly stable as a neutral charge defect.⁴¹ The other study calculated energies of defect formation in $\alpha\text{-Al}_2\text{O}_3$, suggesting that the Schottky defects are the most stable defect type, which can be used to support the experimental report.⁴² Remarkably, the DFT-calculated results are consistent with the experimental electron paramagnetic resonance (EPR) data that oxygen vacancies and titanium interstitials exhibit deep-donor characteristics that trap electrons and lead to the formation of small polarons in TiO_2 .⁴³ The first-principles approach was employed to explore the behavior of native defects in monoclinic VO_2 . It was found that oxygen vacancies and oxygen interstitials are readily formed under oxygen-deficient and oxygen-rich conditions, respectively. Both defects generate free carriers in the material.⁴⁴

Besides the extensively studied oxygen vacancy defects, the fundamental understanding of other native defects in V_2O_5 is still not satisfied. It is therefore the objective of this work to utilize the first-principles method to systematically study the behavior of intrinsic point defects in V_2O_5 at synthesized and operating conditions. In particular, we first calculated the electronic structure and charge localization of electronic defects and neutral

native defects. Then, we determined their thermodynamic stabilities and charge transition levels in terms of defect formation energies under different experimental conditions. The statistical model with the constraint of charge neutrality was employed to estimate the concentration of defects and carriers under thermodynamic equilibrium. We found that while the cation vacancies could provide holes to a system, their stabilities were much lower than the other defects. Indeed, the most stable defect is the vacancy of vanadyl oxygen, which is compensated by small electron polarons at the nearby V centers. The transport kinetics of these polarons, in the pristine and oxygen vacancy systems, were determined by calculating their hopping barriers where the polaron mobilities were estimated using the kinetic Monte Carlo simulations.

2. Computational details

All calculations were carried out using the spin-polarized DFT approach as implemented in the Vienna Ab initio Simulation Package (VASP).^{47–49} The projector augmented-wave method was employed to resolve the highly oscillated wavefunction near the core when using pseudopotential.^{50,51} The valence electron, *i.e.*, V 3s3p3d4s and O 2s2p wavefunctions were expanded in the plane wave basis with a cut-off energy of 500 eV. The exchange–correlation functional was approximated by the modified Perdew–Burke–Ernzerhof (PBE) approach called optPBE-vdW, in which van der Waals interactions are also included.^{52–54} This implementation has been proposed to be an efficient and accurate dispersion interaction for correcting the error in determining the interlayer spacing and behavior of ion intercalation in V_2O_5 .⁵⁵ We applied the U parameter to account for spurious self-interaction errors that occurred upon using conventional DFT when treating the highly correlated electron materials such as V_2O_5 .^{29,56} In particular, we are most interested in the behavior of charge localization upon the creation of native defects. Therefore, we carefully tuned the U value of the V-3d electrons (3.5 eV) to reproduce the localization behavior of the extra electrons obtained from ultraviolet photoelectron spectroscopy (UPS)⁵⁷ as detailed in the ESI,† Section S1.^{29,55,57–63} We used the Gaussian smearing method ($\sigma = 0.05$ eV) with the self-consistent field convergence criteria of 10^{-6} eV.

The $1 \times 3 \times 3$ supercell (18 formula units or $V_{36}O_{90}$) of orthorhombic V_2O_5 , the most stable phase, with periodic boundary conditions was used as our model for all calculations. The supercell size is sufficiently large to reach the convergence of oxygen vacancy formation energy³⁹ and to accommodate the lattice distortion of the polaron.⁶¹ The Brillouin zone integration was adopted by $2 \times 2 \times 2$ k -mesh sampling using the Monkhorst–Pack scheme.⁶⁴ To obtain the optimized structures of pristine and defective supercells, all atoms were allowed to relax to minimize the Hellmann–Feynman force acting on each atom until the forces were less than 0.02 eV \AA^{-1} . Notably, we aimed to model the defect formation in the dilute limit, therefore, the supercell geometry of the defective system could remain the same as the pristine during the structural optimization.

The calculations of the projected density of states (PDOS) were employed using the same setting parameters with structural optimization to study the electronic properties. The band-decomposed charge densities of defective states lying inside the bandgap were also calculated to explore charge localization.

3. Results and discussion

3.1 Geometric and electronic structures of pristine V_2O_5

The crystal structure of orthorhombic V_2O_5 has been well-reported in previous experimental and theoretical studies.^{65,66} For the sake of completeness, we briefly discuss its crystal structure here. Fig. 1(a) shows the unit cell containing two formula units (V_2O_{10}) with the calculated lattice constants of $a = 11.665$ Å, $b = 3.621$ Å, and $c = 4.447$ Å, in agreement with the experimental values ($a = 11.510$ Å, $b = 3.563$ Å, and $c = 4.369$ Å).⁶⁵ Each vanadium ion is surrounded by five oxygen ions forming a distorted square pyramid (VO_5) with the calculated V–O bond lengths depicted in Fig. 1(b). Three inequivalent oxygen atoms can be identified: vanadyl-oxygen (O1) pointing in the normal direction, bridge-oxygen (O2) at the corner-sharing polyhedra, and chain-oxygen (O3) at the edge-sharing polyhedra. The monolayer V_2O_5 is formed by connecting the VO_5 pyramids *via* edge-sharing and corner-sharing polyhedra in the *ab*-plane to form zigzag double chains along the *b*-direction. These layers are stacked together along the *c*-direction with weak van der Waals interactions to form a quasi-2D structure like graphite.^{65,67} Note that the

calculated lattice constant c with dispersion energy correction (4.447 Å), is closer to the experimental value as compared to that without the correction (4.804 Å).²⁹

Likewise, the electronic structure of V_2O_5 has been extensively explored computationally and experimentally. It is an n-type semiconductor with an experimental band gap of 2.35 eV.⁶³ In this work, within the DFT+ U description of $U_{3d}(V) = 3.5$ eV, the calculated PDOS exhibits similar band-gap energy (2.18 eV) and DOS features to those of the previous computational works, Fig. 1(c).^{68,69} The top of the valence band (VB) is predominantly composed of O-2p, while the V-3d mainly contributes to the states at the conduction band (CB). Due to a large distortion of VO_5 pyramids from the octahedral symmetry, the interactions between V atoms are strong, resulting in the split-off of V-3d orbitals with a low-lying d_{xy} orbital.^{66,68,70,71}

Table S1 (ESI[†]) summarizes our calculated values related to the structural and electronic properties, *i.e.*, lattice constants, bond lengths, and band-gap energy, as compared to previous computations and experiments. The systematic agreement indicates that the inclusion of the U parameter and van der Waals interaction in our model study is reliable. Note that the inclusion of vdW interactions mainly affects the structural properties, *i.e.*, the interlayer spacing, whereas the U correction mostly changes the electronic structure, *i.e.*, the band-gap energy.

3.2 Structural and electronic properties of native point defects

In this section, we examine the properties of various native point defects in V_2O_5 including electronic defects (electron and hole), vacancies, and self-interstitials. The antisite disorders were neglected due to the mismatch in the ionic radius and the strong ionicity of V_2O_5 , similar to the case of TiO_2 .⁷³ The structural and electronic properties of the accompanying point defects in the V_2O_5 are reported and discussed. In particular, the calculated PDOS and charge localization of each defect shed light on various possible charge compensation mechanisms upon the defect formation. Understanding such mechanisms can help to explain the behavior of electron conduction.

A. Electronic defects. The electron-doped system was obtained by manually adding one extra electron to the supercell. The details of the local structure distortion and the electronic structure of the electron-doped system have been extensively discussed in our previous work.³² On the one hand, the added electron localized at a V-center induces a small distortion around the VO_5 unit where the V–O bonds are slightly lengthened, leading to the formation of a small electron polaron (η^-) as shown in Fig. 2(a). The added electron mainly occupied the low-lying V- d_{xy} states at 1.2 eV above the VBM, as illustrated in the PDOS and the shape of the polaronic isosurface. Based on the PBE+ U method ($U = 3.5$ eV), it should be noted that the electron polaron is not fully localized at the V center, but partially (around 10%) spills to the neighboring V center connected to O2 in the *a*-direction. The charge localization is within a unit cell referred to as a small polaron.

On the other hand, the added electron can exhibit delocalization behavior, which partially occupies all V centers in the

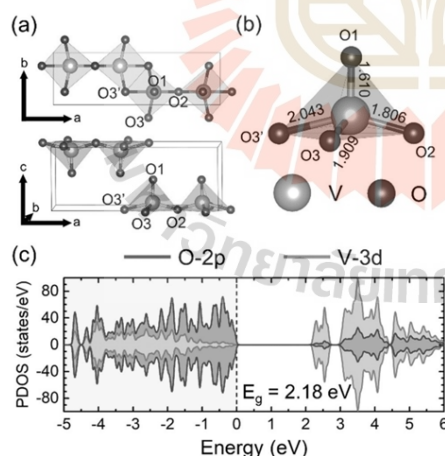


Fig. 1 (a) The unit cell of orthorhombic V_2O_5 containing 14 atoms, where gray and red atoms represent V and O, respectively. (b) The pink polyhedron illustrates the distorted square pyramid of VO_5 and all corresponding V–O bond lengths are in Å. All 3-dimensional representations of the crystal structure were illustrated using the VESTA program.⁷² (c) The calculated projected density of states (PDOS) of pristine V_2O_5 . The zero-energy was set to the VBM, where the dashed line indicates the energy level of the last occupied electron.

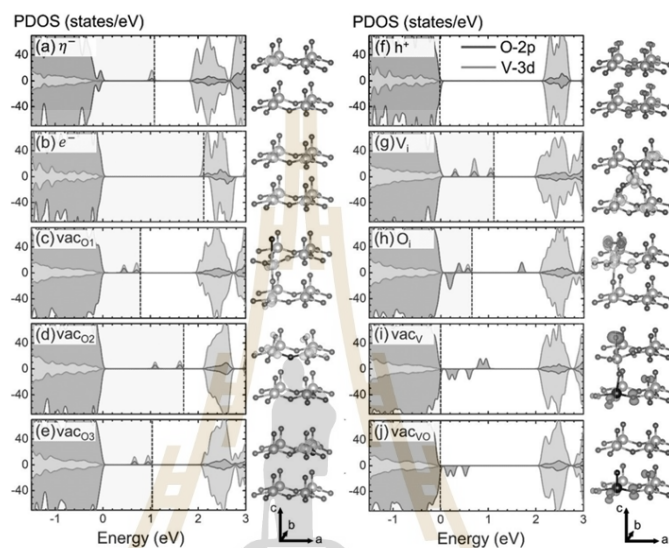


Fig. 2 The optimized structure and PDOS of (a, b and f) electronic defects and (c–e and g–j) several native point defects in neutral charge. Only structures in the region near the defect site are shown for clarity. Black atoms represent the vacancy sites. The zero-energy is set to the VBM, where the dashed lines in each plot indicate the energy level of the last occupied electron. The yellow/blue colored isosurface illustrates the band-decomposed charge density of the occupied/unoccupied defect states aligned in the bandgap. The isosurface level is set to $0.02 \text{ e}^- \text{ \AA}^{-3}$ for all defects except $0.002 \text{ e}^- \text{ \AA}^{-3}$ in the case of (b) free electrons and (f) free holes.

supercell. Such behavior contributes to a shift of the Fermi energy into the conduction band, indicating the formation of a free electron (e^-), as shown in Fig. 2(b). Nevertheless, we found that the formation of a small electron polaron is energetically more favorable with a self-trapped energy of 0.28 eV, which is consistent with the previously reported value of 0.22 and 0.40 eV.^{31,32} The quantitative difference could have originated from the strong influence of the applied U -value as also discussed in our previous work.³² The preferred trapped state implies that carrier species in V_2O_5 are mainly small polarons rather than free electrons as also mentioned in several other theoretical studies.^{29,31,32,55,61,62,74} The computational predictions are consistent with the XPS results of the reduced V_2O_5 showing the existence of partial V^{4+} centers.^{17,30}

The hole-doped system was also investigated where an electron was removed from the supercell. In contrast to electron doping, a hole prefers to be partially delocalized over all the O atoms in the supercell and contributes to unoccupied states as a free hole (h^+) at the VBM, as shown in Fig. 2(f). The formation of a hole polaron was observed when applying an additional U -value at O-2p orbitals at U values greater than 3 eV. Note that extra care needs to be taken since the U parameter is empirical, which could lead to unphysical over-localization of the hole state at a high U -value. The behavior of the hole localization as a function of the U -value is discussed in detail in the ESI,† Section S2.

B. Oxygen vacancies. The presence of oxygen vacancies (vac_O) was extensively studied using many experimental techniques.^{19,23–25,27,29,35,75,76} The roles of vac_O in electronic conductivity, catalysis, and adsorption properties are of particular interest. It is believed that oxygen vacancies produce extra electrons in the system and increase carrier concentrations.^{16,17} Scanlon *et al.* used the DFT+ U method to examine the structural and electronic properties of three distinct vacancy sites, namely, O1, O2, and O3. Their computations revealed a stable O1 vacancy, where its electronic structure is in reasonable agreement with the measured XPS spectra.²⁹

A neutral vac_O , at the O1, O2, or O3 site, similarly induces local lattice distortions and donates two extra electrons localized at two neighboring V-centers, resulting in two-electron polarons as shown in Fig. 2(c–e). The polaronic sites agree very well with that reported in Scanlon's work.²⁹ The PDOS analysis shows that the two polaronic gap states are in the same spin component, consistent with the ferromagnetism of V_2O_{5-x} in previous experiments and calculations.^{76,77} We found that the position and the splitting of polaronic states strongly depend on the local lattice distortion and the interactions between the two states. Note that such behavior was not found in the previous study done by Scanlon *et al.*²⁹ The origin of the inconsistency remains unclear.

In the case of the O1 vacancy (vac_{O1}), the two polaronic states lie at 0.50 and 0.76 eV above the VBM. Their relative

positions are somewhat lower than those of the isolated polaron and other vac_O due to the formation of the stable apex-shared V_2O_5 bi-pyramid, as shown in Fig. 2(c). Upon the formation of vac_O1 , the undercoordinated V atom moves downward to form a V–O1 bond with the O1 of the layer underneath. Such a distorted structure allows the accommodation of the two polarons, resulting in a stable bi-polaronic configuration ($\text{V}^{4+}\text{–O–V}^{4+}$) as illustrated in the isosurface plot of Fig. 2(c). The two polaronic states exhibit t_{2g} character, which is the low-lying energy level in the octahedral crystal field as compared to that of the e_g character.

On the contrary, the polaronic states that originated from the O2 vacancy (vac_O2) lie at 1.14 and 1.66 eV above the VBM which is much higher than those of the vac_O1 as depicted in Fig. 2(d). In this case, vac_O2 repels the two neighboring undercoordinated V centers in the x -direction. The formation of both polarons next to the vacancy site, therefore, mainly comprises x -component orbitals, *i.e.*, the combination of $d_{x^2-y^2}$ and d_{xz} . The contribution of the relatively high crystal field energy of the $d_{x^2-y^2}$ and d_{xz} admixture could be the reason for high-energy polaronic states. In addition, unlike the polaronic states generated upon the vac_O1 , the vac_O2 states are coupled as bonding and antibonding states with a large energy gap of 0.52 eV, as shown in Fig. S3(b) (ESI†).

Similar to the case of vac_O2 , the formation of the O3 vacancy (vac_O3) pushes the neighboring V-centers in the y -direction, resulting in the polaronic contribution of d_{xy} and a small amount of $d_{x^2-y^2}$ on both V-centers as depicted in Fig. 2(e). The small contribution of $d_{x^2-y^2}$ leads to relatively high-energy polaronic states at 0.71 and 1.00 eV above the VBM, which are higher than those of vac_O1 states but significantly lower than the vac_O2 states. The smaller bonding–antibonding splitting of 0.29 eV indicates the weakly coupled polaronic states as shown in Fig. S3(c) (ESI†).

C. Vanadium interstitials. To create the neutral V self-interstitial defect (V_i), a V atom was inserted between V_2O_5 layers where it was surrounded by six O atoms including four O1 atoms of the lower layer and two O2 atoms of the upper layer with the V–O bond lengths of 2.06–2.13 Å, as shown in Fig. 2(g) and Fig. S4 (ESI†) (configuration A). The inserted position of the interstitial atom corresponds well with the previous computational works such as Li interstitial³⁹ and other cation interstitials.³⁹ We tried two other inequivalent configurations as discussed in the ESI,† Section S4. The configuration that we present here in Fig. 2(g) is the most stable defect structure, which was chosen to be a representative of V_i . In Fig. 2(g), The PDOS exhibits five gap states at 0.07, 0.39, 0.78, 0.81 and 1.14 eV above the VBM, which are aligned in the same spin component resulting in the magnetization of $5 \mu_B$. Their band-decomposed charge density revealed that two of the five electrons localized at the V_i site, which exhibited the d_{z^2} and $d_{x^2-y^2}$ character. The other three electrons were trapped as small polarons at the three nearby V-centers, as shown in Fig. 2(g). The local distortion occurred upon the polaron formation and pushed the inserted V atom into the off-centered position, which minimized the distance to the three reduced V-centers

as shown in Fig. S4 (ESI†). These three polarons are arranged in such a way that the in-plane distortion and vertical repulsion are avoided.⁶² It is noted that the V_i , theoretically, donates only three extra electrons to form the polarons, resulting in an oxidation state of V^{3+} . Such a high charge state could dramatically increase carrier concentrations, which in turn, would improve the electronic conductivity of the materials.

D. Oxygen interstitials. Likewise, the neutral O self-interstitial (O_i) was considered similar to the V self-interstitial. We added an O atom at the high symmetric site between the layers as the initial configuration. After geometry relaxation, we find that the inserted O atom is likely to bond with one terminal O1 atom. The O–O bond is tilted from the a -axis to the c -axis by 45° , with the bond length of 1.33 Å and denoted as “normal interstitial” as shown in Fig. S5 (ESI†). In addition, we consider the configuration where the pair of O interstitial and lattice O1 share the same O1 site, which is called “split interstitial”, as shown in Fig. S5 (ESI†). The O–O bond length is 1.34 Å, aligned in parallel to the a -axis. The center of the bond is at the lattice O1 site with the O and V distance of 2.00 Å. This defect can be named as a substitution of an O_2 molecule at the O1 site, whereas the O–O bond is slightly longer than that of the O_2 molecule (1.21 Å). This type of defect is also found in other metal oxides *e.g.* Ga_2O_3 ,⁷⁸ TiO_2 ,⁷³ and ZnO .⁷⁹ We found that the electronic energy of the O split interstitial became lower than that of the normal one at around 0.36 eV. Therefore, the O split interstitial was selected as representative of the defect.

The electronic structure (PDOS) of the neutral O split interstitial (O_i) displays four occupied gap states at 0.22, 0.27, 0.43 and 0.62 eV and one unoccupied state at 1.75 eV above the VBM, as shown in Fig. 2(h). The first two and the latter two states are in the opposite spin component, resulting in the zero net magnetic moment. These states are mainly contributed by the connected V-center with collective contributions from the surrounding O2 and O3 atoms, as shown in the band-decomposed charge density plot in Fig. 2(h). The charge density of the unoccupied state was also plotted as the blue-colored isosurface, which was fully located at the O2 defect site.

To better understand the electronic structure of the O_i defect, it is useful to discuss the molecular orbital of an O_2 molecule. The frontier orbital of the O_2 molecule exhibits half-filled π antibonding orbitals, likewise, the O_i defect states are predominantly of π -antibonding character. Nevertheless, the O_i defect involves the lattice oxygen of the O^{2-} ion, which yields two additional electrons when compared with the O_2 molecule. These two extra electrons of the O_i defect behave quite differently, where one electron is localized at the V-center and forms a small polaron. The other electron is added to the half-filled π -antibonding orbital of the O_2 molecule leading to an elongation of O–O bond, which corresponds to an O^{2-} ion. Such interpretation is consistent with the previous studies of split-interstitial in other metal oxides.^{73,78} The detailed analysis is discussed in the ESI,† Section S5.

E. Vanadium and vanadyl vacancies. As shown in Fig. 2(i), the formation of a neutral V vacancy (vac_V) creates a large lattice reorganization around the defect site. The V-center directly

above the defect site displaces downward to bond with the dangling O1 atom with the V–O1 bond length of 1.61 Å, yielding a distorted VO₆ octahedron. Such reorganization was accompanied by the breaking of the V–O1 bond of the original VO₅ square pyramid, where its equilibrium distance became 2.26 Å, leaving an isolated oxygen atom between the V₂O₅ layers. Its PDOS displayed five unoccupied gap states at 0.23, 0.34, 0.65, 0.96, and 1.00 eV above the VBM where their charge density is plotted as the blue-colored isosurface in Fig. 2(i). The first three states are aligned in the spin-down component and separately localized over the nearby O atoms in the layer. On the other hand, the latter two states are spin-up, which were localized at the O-p_x and O-p_y of the top O1 atom, indicating the formation of small hole polarons. It is noted that a hole polaron must be accompanied by a large lattice distortion, like the case of vac_v, and it cannot be formed in the hole-doped system as an electronic defect as discussed in Section 3.2.A.

The dramatic reorganization that occurred upon the formation of vac_v led to the formation of an isolated oxygen atom and gave rise to the possible formation of a vanadyl vacancy (vac_{vo}). In other words, it is structurally appealing to remove both V and its O1 at the same time. The formation of vac_{vo} did not significantly distort the host structure as compared with that of the vac_v. Its PDOS and charge density of defect states revealed the formation of large hole polarons at the layered oxygen atoms, whereas the small polaronic states were absent, Fig. 2(h). In addition, the formation of vanadium and vanadyl vacancies could provide additional intercalation sites for small cations such as Li and Na, resulting in the enhanced Li/Na capacity for rechargeable battery applications.¹⁸

3.3 Stability of native defects

Defects can possibly exchange electrons with the reservoir, resulting in charged defects where their relative stabilities are of interest. For example, the two occupied gap states of vac_o imply that vac_o can donate up to two electrons to the reservoir and become +1 or +2 charged defects. On the other hand, the vac_v with five unoccupied states possibly accepts up to five electrons from the reservoir, yielding up to –5 charged defects. The stability of a particular charged defect depends on the energy of the electron in the reservoir, *i.e.*, the Fermi energy. Hence, to better understand the donor/acceptor behavior and stabilities of the charged defects in V₂O₅, we calculated their formation energies as a function of Fermi energy ranging from the VBM to the CBM. The defect formation energy (DFE) of a particular point defect X in charge state *q* can be expressed as follows:^{40,80}

$$E^f(X^q, E_F) = E_{\text{tot}}(X^q) - E_{\text{tot}}(\text{bulk}) - \sum_i n_i \mu_i + q(E_{\text{VBM}} + E_F) + E_{\text{corr}},$$

where $E_{\text{tot}}(X^q)$ and $E_{\text{tot}}(\text{bulk})$ are the electronic energy of a defective and bulk supercell, respectively. The integer n_i is the number of elemental species *i* either added to ($n_i > 0$) or removed from ($n_i < 0$) the defective supercell. μ_i represents the chemical potential of elemental species *i* associated with the

required energy for exchanging the element with the reservoir. The detailed calculations of the chemical potential of each elemental species, which correspond to the synthesis conditions, *e.g.* O-poor and O-rich, are described in ESI,† Section S6.^{34,41,58,59,81,82} Under the O-poor conditions, V₂O₅ might be annealed at high temperatures under lower O₂ partial pressure or inert gas atmosphere. In contrast, the materials annealed at relatively low temperatures under O₂ atmosphere corresponded to the O-rich conditions. In the case of a charged defect, the DFE also depends on the energy of the electron reservoir in the material, *i.e.*, $E_{\text{VBM}} + E_F$. The last term, E_{corr} , is the electrostatic energy correction due to the artifact in a finite-sized supercell. The adapted Makov–Payne correction⁸³ was employed to treat the E_{corr} as it was successfully used to account for the anisotropic dielectricity of various quasi-2D materials such as CeO₂⁴⁶ and MoO₃.⁴⁵

As shown in Fig. 3, we considered the formation energies of native defects at different experimental O-poor and O-rich conditions. The slope of each line indicates the charge of the defect, where only the most stable charge states are shown. Firstly, the DFE of the electron polaron in charge state –1 is plotted in the black dashed line in Fig. 3. It intersected with the zero formation energy for perfect V₂O₅ as plotted in the black solid line at the Fermi energy of 1.89 eV. Beyond this Fermi energy, the perfect crystal prefers to receive an electron to form the more stable electron polaron due to its lower DFE. In other words, the polaronic defect exhibits the charge transition level (CTL) between the 0 and –1 charge state at $\epsilon(0/-1) = 1.89$ eV. It should be noted that the electron polaron can occur at the Fermi energy below the $\epsilon(0/-1)$, but in a smaller proportion

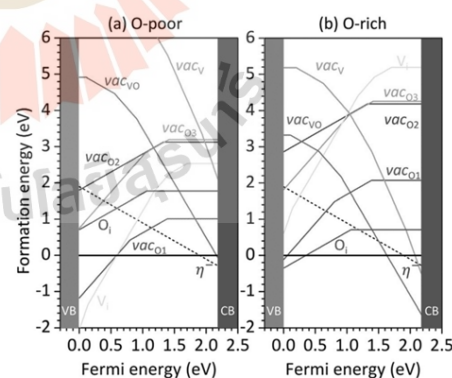


Fig. 3 The formation energy as a function of the Fermi energy of native defects that can occur in V₂O₅ in various charge states. The zero-point of the Fermi energy and its upper limit are set at the valence band maximum and conduction band minimum. The set of elemental chemical potentials is related to (a) O-poor and (b) O-rich conditions. The slope of each line is proportional to the charge state of the defect and only the energetically most favorable charge state for a given Fermi energy. The horizontal black line represents the zero formation energy of the perfect V₂O₅.

(depending on the exponential of its DFE at that Fermi energy). The thermodynamic transition level of the polaron (1.89 eV) is somewhat larger than that defined by its PDOS (1.20 eV). Such a difference is expected because the electronic structures calculated using DFT are subjected to an approximation of the Kohn–Sham equation, whereas the polaronic level of CTL is derived from the total energies including many-particle effects, which is explained in the case of the polaronic state in CeO₂.⁸⁴

Next, we discuss the relative stabilities of different types of oxygen vacancies, *i.e.*, vac_{O1}, vac_{O2}, and vac_{O3}. In general, an oxygen vacancy can donate up to two electrons to the host material, yielding possible charge states of +2, +1, or neutral. In V₂O₅, all vac_O exhibit neutral charge states at the Fermi energy close to CBM. As shown in Fig. 3, these defects donate their electrons to form the charge state of +1 at the $\epsilon(+1/0) = 1.40$, 1.34, and 1.41 eV for vac_{O1}, vac_{O2}, and vac_{O3}, respectively. vac_{O1} and vac_{O3} can further donate the other electron to form charge state +2 at the $\epsilon(+2/+1) = 0.81$ and 1.03 eV, respectively. The vac_{O2} of the +2 charge state does not exist because its optimized structure involves the movement of O1 to occupy the original vac_{O2} position and form a vac_{O1} instead. The calculated formation energies indicate that the vac_{O1} is much more stable than other vac_O by at least 2 eV. This is because the two V-centers of the apex-shared V₂O₅ in vac_{O1} is more stable than the V-centers with dangling bonds in vac_{O2} and vac_{O3}. In addition, its formation energy is significantly lower than those other defects, especially at moderate Fermi energy under O-poor conditions. Thus, vac_O is likely to take place at the O1 site, which agrees very well with the previous works.^{23,29,35,75}

Similar to vac_O, the V_i defect is considered an electron donor where it can donate up to five electrons resulting in charge states ranging from zero to +5. Its CTLs are $\epsilon(+5/+3) = 0.15$ eV, $\epsilon(+3/+2) = 1.19$ eV, $\epsilon(+2/+1) = 1.41$ eV, and $\epsilon(+1/0) = 1.69$ eV. We find that the high charge states of +3 and +5 are energetically stable in a wide region where they are even more stable than double donor vac_{O1} as the Fermi energy approaches the VBM at O-poor conditions.

In contrast, the PDOS of the O_i defect exhibits both occupied and unoccupied gap states indicating that it could act as both donor and acceptor. From the calculated DFE, the O_i defect is stable in the charge states of 0 and +1. The O_i donates an electron occupied in the highest energy state and turns out to be a single donor under lower Fermi energy. The neutral and single donor O_i are dominant under O-rich conditions, with CTL at $\epsilon(+1/0) = 1.06$ eV. Such donor behavior of the O_i has also been reported in other metal oxides.⁸⁵ The acceptor state (charge state of -1) is not likely to occur since the added electron does not fill the unoccupied state of O–O π antibonding, instead it forms a small polaron at the nearby V-center. In addition, a higher charge state of O_i defect was examined. We found that the molecular O₂ located at the O1 site in the double donor O_i tends to move away from the lower V-center. As a result, the defect O_i decomposed into the O₂ molecule and vac_{O1} as shown in Fig. S8 (ESI[†]). When two electrons are removed from the O_i, *i.e.*, polaronic and O–O π antibonding states, the O–O bond in molecular O₂ becomes stronger and leaves the V-center

underneath. Thus, we can ignore the O_i in the higher charge state due to its instability.

In the case of vac_V, the neutral defect has five unoccupied states that can accept up to five electrons. However, the DFE of the lower charged states ranging from 0 to -4 were significantly higher than those other defects, especially in the O-poor conditions. Only the -5 charge state is relatively stable at the Fermi energy close to the CBM. Similar to vac_V, the vac_{V0} are stable in the charge states ranging from -3 to 0. Only the highly charged acceptor of -3 is dominant when the Fermi energy approaches the CBM under O-rich conditions. Note that this defect is identical to the complex defect between vac_V and vac_{O1}. The calculated binding energy of the defect complex, *i.e.*, vac_{V0} \rightarrow vac_V + vac_{O1}, is 3.80 eV at the Fermi energy of 1.0 eV above the VBM under O-rich conditions. Such a high binding energy implies that it is more likely to form the vacancy pair, vac_{V0}, rather than the isolated vac_V and vac_{O1}. According to the PDOS, vac_V and vac_{V0} generate shallow acceptor states that can provide holes to the system. However, the acceptors are readily compensated by the low DFE donors, *i.e.* O_i (O-rich) and vac_{O1} (O-poor), instead of forming a hole under both conditions. As a result, the intrinsic p-type doping is difficult in V₂O₅. Nevertheless, it is noted that the recent work has reported the p-type conductivity of hydrated amorphous V₂O₅.⁸⁶

We also explored the formation of hydrogen passivation in the vac_{V0} defect by adding a H atom at the undercoordinated O2 atom to form a H-vac_{V0} defect, which might be expected from the presence of water even under normal synthetic conditions. As shown in Fig. S9 (ESI[†]), the defect is more stable as a double acceptor. Compared to the vac_{V0}, the H-vac_{V0} is thermodynamically more favorable, especially the synthesis under high H₂O partial pressure. However, it is significantly less stable than other defects such as vac_{O1} and η^- . The detailed calculation and further discussion of the defect are described in the ESI[†] Section S8. Note that the H-vac_{V0} could be formed much more easily in the H-rich conditions such as under a H₂ atmosphere. Both acceptor defects including H-vac_{V0} and vac_{V0} may act as electron trapping centers, which could diminish the electronic conductivity of the materials.

3.4 Defect concentration under thermodynamic equilibrium

As discussed in the previous section, the formation energies of defects and their stabilities depend strongly on the position of the Fermi energy. In this work, we used the recently proposed approach to determine the Fermi energy at a particular thermodynamic equilibrium, as detailed in ESI[†] Section S9.^{75,87} Fig. 4 shows the equilibrium concentrations of defects and charge carriers under growth conditions ranging from O-poor to O-rich. Since V₂O₅ is generally synthesized under atmospheric pressure with an annealing temperature of around 350–450 °C, we set the temperature to be 723 K (450 °C) for this analysis.^{34,91,82}

At the O-poor limit, the pinned Fermi energy of 1.13 eV satisfies the constraint of charge neutrality, where the vac_{O1} defect exhibits the highest concentration of 1×10^{17} cm⁻³. However, this vac_{O1} concentration is relatively low as compared

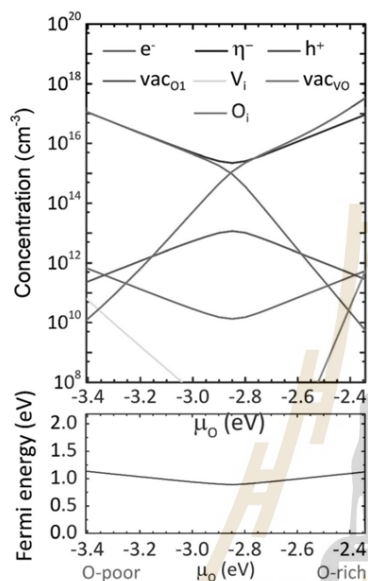


Fig. 4 Concentrations of dominant native defects as a function of the chemical potential of O (μ_{O}) under conditions of charge neutrality [above], and the self-consistent Fermi energy [below] at the annealing temperature of 723 K.

to the number of lattice oxygen sites of $5 \times 10^{22} \text{ cm}^{-3}$ in a perfect crystal. The $\text{vac}_{\text{O}1}$ is mainly stable as the positive charge (+1), which can be compensated by the negatively charged polaron. In addition, the highly positively charged V_i exists at relatively low concentrations, whereas the concentrations of other defects are negligible. As μ_{O} increases, the concentrations of $\text{vac}_{\text{O}1}$ and compensating η^- slightly decrease because the DFE of $\text{vac}_{\text{O}1}$ increases with μ_{O} .

When μ_{O} is larger than -2.85 eV , O_i in both the neutral and positively charged states become more stable than the $\text{vac}_{\text{O}1}$ where the positively charged O_i is compensated by η^- . The equilibrium Fermi energy consistently increases with μ_{O} and concentrations of O_i and η^- until it reaches the O-rich limit where the Fermi energy is 1.12 eV with the concentration of O_i and η^- of 2×10^{17} and $6 \times 10^{16} \text{ cm}^{-3}$, respectively.

At the O-rich limit, O_i is more stable in a neutral charge state rather than as a donor. Here, only a small amount of vac_{VO} can be found, whereas other defects are negligible under the O-rich conditions. Note that the most stable donors ($\text{vac}_{\text{O}1}$ in O-poor condition and O_i in O-rich condition) are compensated by the same species, *i.e.*, electron polaron (η^-). Therefore, η^- is the major charge carrier for electrical conductivity because the density of η^- is significantly higher than that of free carriers, *i.e.*, electrons (e^-) and holes (h^+).

Although V_2O_5 is normally prepared at high temperatures, *e.g.* 723 K, the material is commonly used under ambient conditions. When the system is quenched to room temperature, the populations of defects and carriers are adjusted to a new equilibrium. Generally, the numbers of h^+ , e^- and η^- from thermal excitation decrease with temperature, whereas the concentrations of other defects are assumed to be fixed at the annealing temperature because the required kinetic energy for defect reorganization is quite large. As a result, the ratio between different charge states must be renormalized by the new formation energies at a given Fermi energy. The redistributed concentration of defect X at charge state q is derived from
$$N(X^q) = \frac{\exp(-E^i(X^q)/kT)}{\sum \exp(-E^i(X^{q'})/kT)} N(X),$$
 where $N(X)$ is the total concentration of defect X and q' of all possible charges. We assume that the μ_{O} remains unchanged while quenching.

After annealing at 723 K, V_2O_5 is quenched to room temperature at 300 K resulting in a slight shift of the Fermi energy toward the CBM (n-type), as shown in Fig. 5(a). The alteration of Fermi energy is due to the redistribution of the charge states of $\text{vac}_{\text{O}1}$ and O_i after quenching as shown in Fig. 5(b) and (c). At the O-poor limit, the double and single donor $\text{vac}_{\text{O}1}$ are major defect species under the annealing conditions, as shown in Fig. 5(b). Under the quenched conditions, however, the positively charged $\text{vac}_{\text{O}1}$ becomes neutral where the concentration of η^- consistently decreases with the concentration of single donor $\text{vac}_{\text{O}1}$, as shown in Fig. 5(c).

Likewise, at the O-rich region where O_i is dominant, the donor O_i is neutralized after quenching as illustrated in Fig. 5(c). Nevertheless, the donor O_i concentration in the O-rich region rapidly drops as compared to the $\text{vac}_{\text{O}1}$ case in the O-poor region. In particular, the neutralized proportion, *i.e.*, the ratio between charge state 0 and +1 of O_i (10 000 times under O-rich conditions) is even higher than that of the $\text{vac}_{\text{O}1}$ (50 times under O-poor). The donor O_i is more easily compensated because the CTL of O_i , $\epsilon(+1/0) = 1.06 \text{ eV}$, is deeper than that of $\text{vac}_{\text{O}1}$, $\epsilon(+1/0) = 1.39 \text{ eV}$. As a result, the concentrations of donor and compensating η^- are dramatically low in the quenched O-rich conditions. In addition, the synthesis of V_2O_5 under extreme O-rich conditions could be difficult due to the high O_2 pressure and low temperature, as shown in Fig. S7 (ESI[†]). Overall, to achieve higher carrier concentrations at the operating conditions, it is suggested that the synthesis of V_2O_5 should be carried out under the O-poor conditions rather than the O-rich environment. The formation of oxygen vacancies in O-poor conditions effectively contributes to the carrier concentrations in V_2O_5 and other metal oxides.^{88,89} This is consistent with experiments that normally set the growth condition at the O-poor limit by either increasing the annealing temperature or lowering the O_2 partial pressure.^{17,30} In addition, we explored the effect of annealing temperature on the concentration of $\text{vac}_{\text{O}1}$ and compensating η^- . Fig. 6 shows defect concentrations in the material synthesized under the O-poor conditions with annealing temperature T and then being quenched to 300 K. It can be seen that the concentrations

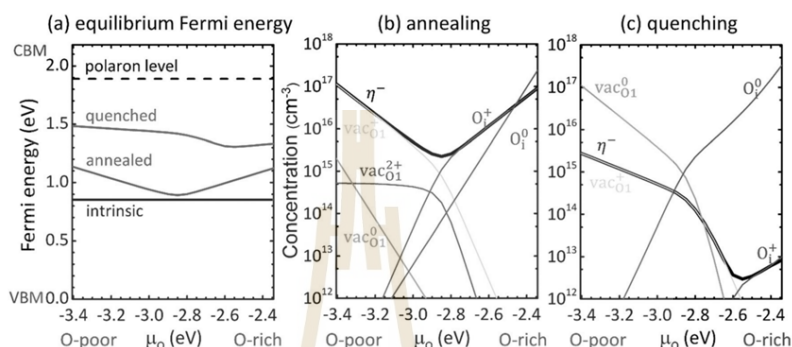


Fig. 5 (a) The pinned Fermi energy in the thermodynamic equilibrium of the material grown at annealing temperature (723 K) and then quenched to ambient conditions (300 K). The corresponding charge state distribution of the dominant defects as a function of the chemical potential of O (μ_{O}) in the material grown at (b) annealing and (c) quenching temperature. The black dashed line in (a) represents the CTL $\epsilon(0/-1)$ of the polaron, i.e., the polaron level in bulk, and the black solid line represents the intrinsic Fermi energy at 300 K where only electron polarons and free holes are considered.

of $\text{vac}_{\text{O}1}$ and compensating η^- rapidly increase with the annealing temperature. For instance, under the conventional annealing temperature of 623–723 K with relatively low O_2 partial pressure, the synthesized material contains the concentration of oxygen vacancies in the order of 10^{16} – 10^{17} cm^{-3} .^{34,81,82}

It is noteworthy that when V_2O_5 is used as the cathode of LIBs, the concentrations of oxygen vacancies and intercalated Li-ions play important roles in determining the charge transport kinetics. At high concentrations of oxygen vacancies and Li-ions, it is speculated that the polarons are very populated and may overlap to yield itinerant behavior of electrons.⁵ In such cases, Li diffusion could be treated as ion diffusion in the field of itinerant electrons in the lattice framework and not as coupled ion-polaron migration as discussed in our previous work.⁶¹

3.5 Polaron transport

Based on thermodynamic calculations, we found that $\text{vac}_{\text{O}1}$ is the dominant defect under the synthesized and quenched conditions. The $\text{vac}_{\text{O}1}$ is mainly stable in the neutral charge state, as shown in Fig. 5(c). However, its CTL $\epsilon(+1/0)$ of 1.39 eV is far below the CBM where the ionization energy required to excite the extra electron to the CB is large as compared to the thermal energy at room temperature. As a result, such a donor defect could not generate free electrons. On the other hand, the deep localized defect state is considered as a small polaron where the extra electron is trapped at a neighboring V-center and accompanied by a small distortion of the VO_5 unit. As discussed in the previous section and shown in Fig. 5(c), a high concentration of small polarons is predicted in V_2O_5 . Therefore, it is expected that the charge transport mechanism of V_2O_5 is based on the thermally activated polaron hopping as also reported in previous experimental and computational works.^{32,61,74,90–92}

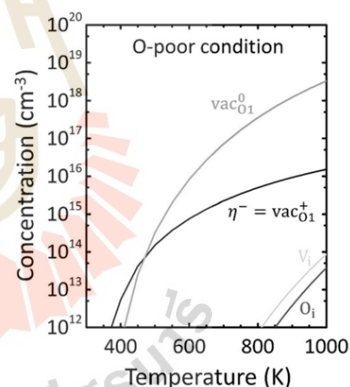


Fig. 6 Concentration of dominant native defects in V_2O_5 grown at annealing temperatures ranging from 300 to 1000 K, and then quenched to 300 K under O-poor conditions.

The neutral charge state of $\text{vac}_{\text{O}1}$ can be considered as a defect complex of positively charged $\text{vac}_{\text{O}1}$ and its compensating polaron, where their binding energy of 0.51 eV ensures a stable defect complex. Nevertheless, a positive binding energy only indicates that the polaron can be bound to the positively charged $\text{vac}_{\text{O}1}$, but not that all polarons and $\text{vac}_{\text{O}1}$ will always form the complex. One reason is the low possibility of finding a polaron near the donor $\text{vac}_{\text{O}1}$ at a low defect concentration.⁴⁰ One of two polarons in the complex defect could hop away from the defect site and yield a donor vacancy and an unbound polaron. To account for the contribution of $\text{vac}_{\text{O}1}$ to the electronic conductivity of V_2O_5 , we calculated the required

energy for one polaron in the complex escaping out of the $\text{vac}_{\text{O}1}$ region as compared to the isolated polaron hopping in the pristine system.

The energy barriers of polaron hopping from the initial site to the neighbors in various crystallographic directions were calculated using the linear interpolation (LE) scheme method. In particular, the atomic coordinates were linearly interpolated between the initial and final configurations. Then, the energy profile along the hopping path was obtained through a set of single-point calculations. This method was used to study the small polaron hopping in several oxides such as TiO_2 ,⁹³ LiFePO_4 ,⁹⁴ BiVO_4 ,⁹⁵ CeO_2 ,⁹⁶ and V_2O_5 .^{32,61} Note that the LE method provides estimations of the hopping barriers that neglects the corrections due to the electronic coupling constant, resulting in the nonadiabatic barriers.⁹⁷

The purpose of this work is to compare hopping barriers of equivalent paths between the system containing an oxygen vacancy and the pristine system, *i.e.*, we focus on qualitative trends in our model study rather than qualitative predictions.

Various polaron migration paths and their barriers in pristine V_2O_5 were extensively elucidated in our previous work.³²

Nevertheless, in this work, all hopping barriers were revisited to consistently compare the calculated barriers with those of the oxygen vacancy system. As shown in Fig. 7(a), the polaron hopping from the initial site (I) to the four inequivalent nearest neighboring sites (A–D) along the [100], [010], [001], and [110] directions were considered, denoted as *a*-, *b*-, *c*-, and *ab*-directions, respectively. We find that the hopping barriers of the polaron toward A, B, C, and D sites are 0.10, 0.22, 0.28, and 0.21 eV, respectively. Although the hopping barriers in the *a*-direction (A site) are significantly lower as compared to the other directions, the next hopping must overcome the higher hopping barriers along the *ab*- or *b*-direction due to the discontinuity of the structure in the *a*-direction. Overall, the most favorable migration path is in-plane and along the *b*-direction, which can either be (i) consecutive hopping in the *ab*-direction (0.21 eV) in a zigzag manner, or (ii) direct hopping in the *b*-direction (0.22 eV), as shown in Fig. 7(a). Note that we also employed the Climbing Image Nudge Elastic Band (CI-NEB) method to calculate the energy barriers of some hopping paths as compared to the LE method. Computations revealed that the LE method provided quite good agreement with the CI-NEB-calculated barriers in the

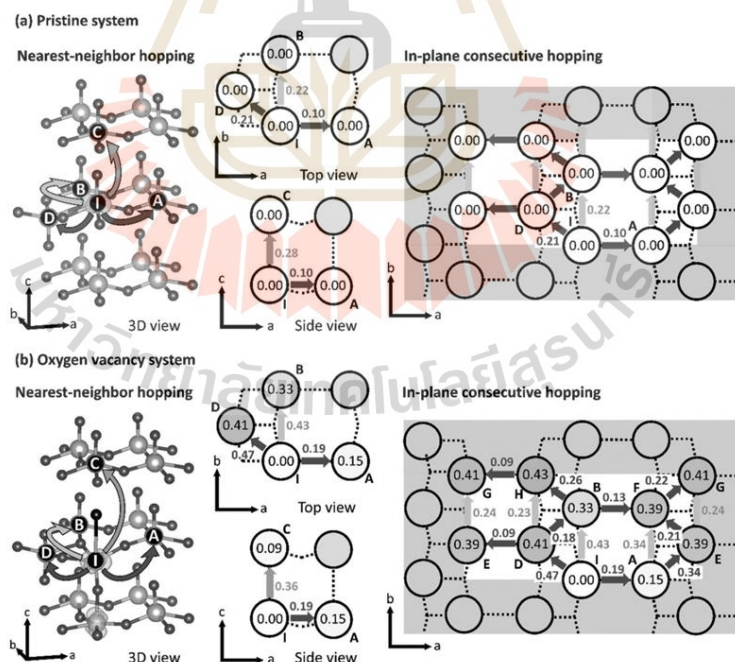


Fig. 7 Schematic illustration of polaron migration paths in (a) pristine and (b) oxygen vacancy systems. The diagrams display the nearest-neighbor [left] and in-plane consecutive hopping [right]. The numbers in the circles are polaronic energies relative to the initial site (I site), whereas the numbers next to the arrows indicate the hopping barriers. All energies are in eV.

a-direction (0.10 vs. 0.09 eV) and *b*-direction (0.22 vs. 0.24 eV). In this regard, it can be inferred that the LE method could capture the major changes of lattice distortion along the reaction coordinate of polaron transfer, e.g. the changes in the V-O bond lengths of the polaronic sites. These results agree very well with previous computational work^{3,2} and the experimentally obtained values of 0.28 and 0.23 eV.^{90,91}

We also investigated the electron occupation of the two V centers involved in the hopping process. For the hopping in the *a*-direction, the electron occupation of the two V centers gradually changed along the hopping coordinate, which implied strong electronic coupling between the initial and final polaronic sites *via* the bridging O2. Such hopping behavior is considered an adiabatic process.⁹⁶ In contrast, for hopping in the other directions, the electron occupies either an initial or final polaronic site along the reaction coordinate, indicating the nonadiabatic behavior of electron transfer.⁹⁶ The non-adiabatic hopping in V₂O₅ is also reported elsewhere.^{61,90}

For the oxygen vacancy system, the initial configuration includes two polarons bound to the vac_{O1} defect site. To determine which polaron, the upper or lower one, is likely to hop away from the defect site, we calculated their hopping barriers and reaction energies when one polaron hops to the nearest-neighboring site while the other polaron remains intact. As shown in Fig. S10 (ESI†) the lower polaron exhibits higher hopping barriers and reaction energies as compared to those of the upper one in all considered directions. The calculated results indicate that it is energetically and kinetically more favorable for the upper polaron to hop away from the defect site. This result agrees with the calculated DOS of neutral vac_{O1} as shown in Fig. 2(c), where the upper polaron is at the higher energy state, which is more activated and likely to become an unbound polaron.

The polaron hopping barriers in the vac_{O1} system are significantly higher than those in the pristine system as shown in Fig. 7(b). In particular, the migration to the D site, which is kinetically favorable in the pristine system, is the least favorable in the vac_{O1} system with a barrier of 0.47 eV. In the presence of vac_{O1}, the hopping barriers to B and C sites also increase to 0.43 and 0.36 eV, respectively. Among these migration paths, hopping along the *a*-direction (A site) exhibited the lowest barrier of 0.19 eV. We also considered the subsequent steps of the in-plane hopping away from the defect region. As shown in Fig. 7(b), the consecutive hopping diagram revealed the required energy for each migration and relative energy as compared to the defect site. For example, the migration from site I to site E could start with the hopping from site I to site A with a small barrier of 0.19 eV. Then, the migration needs to overcome a second barrier of 0.34 eV to site E. Accounting for the relative energy between site I and site A of 0.15 eV, the effective barrier for the migration from site I to site E is 0.15 + 0.34 = 0.49 eV. Likewise, the effective barrier for migration from site I to site F through site B is 0.33 + 0.13 = 0.46 eV. The effective barrier for the hopping to other sites, e.g., H (B to H, 0.33 + 0.26 = 0.59 eV) and G (F to G, 0.39 + 0.22 = 0.61 eV) is around 0.6 eV. When the polaron is located at sites D, E, F, G,

and H, the outward defect regions of its hopping barriers resemble those of the pristine system. In other words, if the polaron can overcome such a high barrier around 0.6 eV, it could leave the defect center and further migrate to the pristine region. Note that we did not consider the events of consecutive polaron hopping in the other V₂O₅ layer or across the layers for the system containing oxygen vacancies due to the supercell-size limitation. Our system includes three layers of V₂O₅ where the polaron may spuriously interact with the defect of the periodic image, which could lead to incorrectly calculated barriers. We further considered the second polaron binding with the defect center when the first polaron is out of range. The calculated binding energy of 1.09 eV indicates the immobilization of the second polaron. Thus, only one of the two polarons that originated from vac_{O1} can escape from the trapping defect site and become an unbound polaron that can contribute to the carrier concentrations in the material.

To determine if the polaron that originated from the oxygen vacancy could contribute to the electronic conductivity of the material, we calculated its in-plane mobility (μ) and compared it with that of the pristine system. The mobility was calculated using the Einstein-Smoluchowski (ES) equation:

$$\mu = \frac{Dq}{k_B T}$$

where q is the charge of the polaron and $k_B T$ is the thermal energy. The diffusion coefficient (D) can be obtained by using the lattice-based kinetic Monte Carlo (kMC) simulation to carry out stochastic sampling of hoppings along each direction in the layer. The kMC simulation was adapted from our previous work where we used kMC to calculate the polaron mobility in BiVO₄.⁹⁸ The rate corresponding to the hop from site i to site j (k_{ij}) is expressed as follows:

$$k_{ij} = \nu^0 \exp\left(-\frac{E_a^{ij}}{k_B T}\right) \text{ where } \nu^0 = 2h/k_B T$$

h is Planck's constant, and temperature (T) was set to 300 K. The calculated barrier from the neighboring hopping from Fig. 7 was used for E_a^{ij} . The sampling of 10^8 hopping steps was used to estimate the diffusion coefficient and polaron mobility for three different systems with periodic boundary conditions including the pristine system, the vac_{O1} system, and a diluted vac_{O1} system.

Computations revealed that the calculated polaron mobilities in the pristine, vac_{O1}, and diluted vac_{O1} systems are 2.7×10^{-4} , 6.8×10^{-8} , and $8.0 \times 10^{-8} \text{ cm}^2 \text{ V}^{-1} \text{ s}^{-1}$, respectively. Due to the relatively high effective barriers at the oxygen vacancy sites, the calculated mobilities of the system containing vac_{O1} are 4 orders of magnitude lower than that of the pristine system. As the concentration of oxygen vacancies becomes lower, from $7.0 \times 10^{20} \text{ cm}^{-3}$ (vac_{O1} system) to $2.6 \times 10^{19} \text{ cm}^{-3}$ (diluted vac_{O1} system), the polaron mobility slightly increases. The estimated mobilities are consistent with the calculated barriers, which confirmed that the oxygen vacancy acts as a trapping site and diminishes the polaron transport. Nevertheless, the moderately high concentrations of oxygen vacancies under O-poor conditions

($1.2 \times 10^{17} \text{ cm}^{-3}$ compared to $5 \times 10^{22} \text{ cm}^{-3}$ of lattice oxygen) provide a much larger carrier concentration ($1.2 \times 10^{17} \text{ cm}^{-3}$) as compared with the intrinsic polaron concentrations generated from thermal activation at 300 K ($4.2 \times 10^4 \text{ cm}^{-3}$). Despite the sluggish polaron mobility in the oxygen vacancy systems, the dramatically increased carrier concentrations could improve the overall electronic conductivity of the materials. Note that the used lattice-based kMC model provides concentrations of oxygen vacancies that are much higher than those of the predicted value (up to 3 orders of magnitude) due to limited system sizes. The estimated mobility from our model is, therefore, the low limit value where the calculated mobilities of the actual concentration of oxygen vacancies should not be less than these values.

Furthermore, based on the stability of vac_{O_1} in the neutral charge state, we also calculated the migration barriers of the polarons- vac_{O_1} complex where the polarons and vac_{O_1} move in a coupled fashion. We employed the CI-NEB method⁹⁹ to calculate the minimum energy path of this complex along the *a*-, *b*-, and *c*-directions. As shown in the ESI,† Section S11, the hopping barriers along the *a*- (2.0 eV), *b*- (2.50 eV), and *c*- (1.80 eV) directions are extremely high, implying the sluggish kinetics of the defect complex that does not play a role in the charge transport properties of the material.

4. Conclusions

In this work, we utilized the DFT+*U* method and the statistical model to systematically study the electronic and thermodynamic properties of intrinsic point defects in V_2O_5 . The electronic structures and formation energies of all possible point defects, including electronic defects, vacancies, and self-interstitials, were calculated. The concentrations of defects and carriers were estimated based on the constraint of charge neutrality under thermodynamic equilibrium. We found that vanadium and vanadyl vacancies exhibit electronic structures of shallow acceptors, which could provide holes to the system. However, doping with p-type is quite difficult since the acceptor is compensated by the more stable oxygen vacancies and oxygen interstitial species. The vanadyl-oxygen (O1) vacancy is the major native defect found in V_2O_5 synthesized under the O-poor conditions, whereas interstitial oxygen is dominant in the O-rich conditions. In particular, at annealing temperatures, high concentrations of positively charged oxygen vacancies and compensating polarons are predicted. After quenching to ambient temperatures, almost all positively charged defects become neutral due to the charge redistribution at the new equilibrium leading to the decrease in carrier concentrations. Nevertheless, the higher the annealing temperatures, the higher the oxygen vacancy and carrier concentrations at quenched ambient conditions. To determine if polarons generated from oxygen vacancies can contribute to the carrier concentrations, we calculated polaron hopping barriers away from the oxygen vacancy site and compared its barriers to that of the isolated polaron in the pristine system. We found that the effective barrier for escaping from the trapping site (0.6 eV) was significantly higher than that of the isolated polaron (0.2 eV). The

estimated polaron mobilities obtained from kMC simulations agree with the calculated barriers that oxygen vacancies can trap polarons leading to lower mobilities by 4 orders of magnitude. Nevertheless, the dramatically increased carrier concentrations due to the high concentrations of oxygen vacancy could improve the overall electronic conductivity of the materials despite the diminished polaron mobility.

Conflicts of interest

There are no conflicts to declare.

Acknowledgements

This work was primarily funded by the Development and Promotion of Science and Technology Talents Project (DPST Research Grant No. 016/2559) and partially supported by the Research Network NANOTEC (RNN) program of the National Nanotechnology Center (NANOTEC), NSTDA, Ministry of Higher Education, Science, Research and Innovation (MHESI), Thailand. Sirichok Jungthawan was supported by Suranaree University of Technology and Thailand Science Research and Innovation (TSRI). We would like to thank NSTDA Supercomputer Center (ThaiSC); Institute of Science, Suranaree University of Technology; and the Synchrotron Light Research Institute (SLRI) for computational resources.

References

- 1 B. M. Weckhuysen and D. E. Keller, *Catal. Today*, 2003, **78**, 25–46.
- 2 M. Pradhan, A. Roy, A. K. Sinha, R. Sahoo, D. Deb and T. Pal, *Dalton Trans.*, 2015, **44**, 1889–1899.
- 3 N. A. Chernova, M. Roppolo, A. C. Dillon and M. S. Whittingham, *J. Mater. Chem.*, 2009, **19**, 2526–2552.
- 4 X. Liu, J. Zeng, H. Yang, K. Zhou and D. Pan, *RSC Adv.*, 2018, **8**, 4014–4031.
- 5 L. R. De Jesus, J. L. Andrews, A. Parija and S. Banerjee, *ACS Energy Lett.*, 2018, **3**, 915–931.
- 6 J. Yao, Y. Li, R. C. Massé, E. Uchaker and G. Cao, *Energy Storage Mater.*, 2018, **11**, 205–259.
- 7 E. Umeshbabu and G. R. Rao, *J. Colloid Interface Sci.*, 2016, **472**, 210–219.
- 8 R. Santos, J. Loureiro, A. Nogueira, E. Elangovan, J. V. Pinto, J. P. Veiga, T. Busani, E. Fortunato, R. Martins and I. Ferreira, *Appl. Surf. Sci.*, 2013, **282**, 590–594.
- 9 D. Nunes, A. Pimentel, A. Goncalves, S. Pereira, R. Branquinho, P. Barquinha, E. Fortunato and R. Martins, *Semicond. Sci. Technol.*, 2019, **34**, 60.
- 10 V. Mounasamy, G. K. Mani and S. Madanagurusamy, *Microchim. Acta*, 2020, **187**, 253.
- 11 A. A. Akande, T. Mosuang, C. N. M. Ouma, E. M. Benecha, T. Tesfamichael, K. Roro, A. G. J. Machatine and B. W. Mwakikunga, *J. Alloys Compd.*, 2020, **821**, 153565.
- 12 K. Schneider and W. Maziarz, *Sensors*, 2018, **18**, 11.

- 13 Z. Tong, J. Hao, K. Zhang, J. Zhao, B.-L. Su and Y. Li, *J. Mater. Chem. C*, 2014, **2**, 3651–3658.
- 14 A. Jarry, M. Walker, S. Theodoru, L. J. Brillson and G. W. Rubloff, *Chem. Mater.*, 2020, **32**, 7226–7236.
- 15 I. Mjejri, A. Rougier and M. Gaudon, *Inorg. Chem.*, 2017, **56**, 1734–1741.
- 16 H. Song, C. Liu, C. Zhang and G. Cao, *Nano Energy*, 2016, **22**, 1–10.
- 17 Y. Sun, Z. Xie and Y. Li, *RSC Adv.*, 2018, **8**, 39371–39376.
- 18 K. E. Swider-Lyons, C. T. Love and D. R. Rolison, *Solid State Ionics*, 2002, **152–153**, 99–104.
- 19 H. H. Kristoffersen and H. Metiu, *Top. Catal.*, 2016, **59**, 809–816.
- 20 K. Devriendt, H. Poelman, L. Fiermans, G. Creten and G. F. Froment, *Surf. Sci.*, 1996, **352–354**, 750–754.
- 21 D. S. Su and R. Schlögl, *Catal. Lett.*, 2002, **83**, 115–119.
- 22 K. Hermann, M. Witko, R. Druzinic, A. Chakrabarti, B. Tepper, M. Elsner, A. Gorschlüter, H. Kuhlenbeck and H. J. Freund, *J. Electron Spectrosc. Relat. Phenom.*, 1999, **98–99**, 245–256.
- 23 T. D. Kang, J. S. Chung and J.-G. Yoon, *Phys. Rev. B: Condens. Matter Mater. Phys.*, 2014, **89**, 094201.
- 24 D. Dreifus, M. P. F. Godoy, A. C. Rabelo, A. D. Rodrigues, Y. G. Gobato, P. C. Camargo, E. C. Pereira and A. J. A. de Oliveira, *J. Phys. D: Appl. Phys.*, 2015, **48**, 445002.
- 25 M. Hussain, M. Nadeem, H. Sun, S. Karim, A. Nisar, M. Khan and M. Ahmad, *Mater. Chem. Phys.*, 2015, **159**, 19–24.
- 26 K. Hermann, M. Witko, R. Druzinic and R. Tokarz, *Appl. Phys. A: Mater. Sci. Process.*, 2001, **72**, 429–442.
- 27 M. V. Ganduglia-Pirovano and J. Sauer, *Phys. Rev. B: Condens. Matter Mater. Phys.*, 2004, **70**, 045422.
- 28 J. Goclon, R. Grybos, M. Witko and J. Hafner, *J. Phys.: Condens. Matter*, 2009, **21**, 095008.
- 29 D. O. Scanlon, A. Walsh, B. J. Morgan and G. W. Watson, *J. Phys. Chem. C*, 2008, **112**, 9903–9911.
- 30 Q.-H. Wu, A. Thissen, W. Jaegermann and M. Liu, *Appl. Surf. Sci.*, 2004, **236**, 473–478.
- 31 L. R. De Jesus, G. A. Horrocks, Y. Liang, A. Parija, C. Jaye, L. Wangoh, J. Wang, D. A. Fischer, L. F. J. Piper, D. Prendergast and S. Banerjee, *Nat. Commun.*, 2016, **7**, 12022.
- 32 P. Wathaisong, S. Jungthawan, P. Hirunsit and S. Suthirakun, *RSC Adv.*, 2019, **9**, 19483–19494.
- 33 Y. Natanzon, A. Azulay and Y. Amoyal, *Isr. J. Chem.*, 2020, **20**, DOI: 10.1002/ijch.201900101.
- 34 Y. W. Li, J. H. Yao, E. Uchaker, M. Zhang, J. J. Tian, X. Y. Liu and G. Z. Cao, *J. Phys. Chem. C*, 2013, **117**, 23507–23514.
- 35 Y. Fujikata, F. Ota, K. Hatada and P. Krüger, *Phys. Rev. B*, 2020, **101**, 125124.
- 36 H. L. Tuller and S. R. Bishop, *Annu. Rev. Mater. Res.*, 2011, **41**, 369–398.
- 37 V. B. Vykhodets and T. E. Kurenykh, *RSC Adv.*, 2020, **10**, 3837–3843.
- 38 A. Alkauskas, M. D. McCluskey and C. G. Van de Walle, *J. Appl. Phys.*, 2016, **119**, 181101.
- 39 K. McColl, I. Johnson and F. Cora, *Phys. Chem. Chem. Phys.*, 2018, **20**, 15002–15006.
- 40 C. Freysoldt, B. Grabowski, T. Hickel, J. Neugebauer, G. Kresse, A. Janotti and C. G. Van de Walle, *Rev. Mod. Phys.*, 2014, **86**, 253–305.
- 41 J. Lee and S. Han, *Phys. Chem. Chem. Phys.*, 2013, **15**, 18906–18914.
- 42 X. Xiang, G. Zhang, X. Wang, T. Tang and Y. Shi, *Phys. Chem. Chem. Phys.*, 2015, **17**, 29134–29141.
- 43 B. J. Morgan and G. W. Watson, *Phys. Rev. B: Condens. Matter Mater. Phys.*, 2009, **80**, 4.
- 44 Y. Cui, B. Liu, L. Chen, H. Luo and Y. Gao, *AIP Adv.*, 2016, **6**, 105301.
- 45 D. S. Lambert, S. T. Murphy, A. Lennon and P. A. Burr, *RSC Adv.*, 2017, **7**, 53810–53821.
- 46 L. Shi, E. Vathonne, V. Oison, M. Freyss and R. Hayn, *Phys. Rev. B*, 2016, **94**, 115132.
- 47 G. Kresse and J. Hafner, *Phys. Rev. B: Condens. Matter Mater. Phys.*, 1993, **47**, 558–561.
- 48 G. Kresse and J. Furthmüller, *Comput. Mater. Sci.*, 1996, **6**, 15–50.
- 49 G. Kresse and J. Furthmüller, *Phys. Rev. B: Condens. Matter Mater. Phys.*, 1996, **54**, 11169–11186.
- 50 G. Kresse and D. Joubert, *Phys. Rev. B: Condens. Matter Mater. Phys.*, 1999, **59**, 1758–1775.
- 51 P. E. Blöchl, *Phys. Rev. B: Condens. Matter Mater. Phys.*, 1994, **50**, 17953–17979.
- 52 J. P. Perdew, K. Burke and M. Ernzerhof, *Phys. Rev. Lett.*, 1996, **77**, 3865–3868.
- 53 J. Klimeš, D. R. Bowler and A. Michaelides, *J. Phys.: Condens. Matter*, 2009, **22**, 022201.
- 54 J. Klimeš, D. R. Bowler and A. Michaelides, *Phys. Rev. B: Condens. Matter Mater. Phys.*, 2011, **83**, 195131.
- 55 J. Carrasco, *J. Phys. Chem. C*, 2014, **118**, 19599–19607.
- 56 S. L. Dudarev, G. A. Botton, S. Y. Savrasov, C. J. Humphreys and A. P. Sutton, *Phys. Rev. B: Condens. Matter Mater. Phys.*, 1998, **57**, 1505–1509.
- 57 Q. H. Wu, A. Thißen and W. Jaegermann, *Surf. Sci.*, 2005, **578**, 203–212.
- 58 S. Lutfalla, V. Shapovalov and A. T. Bell, *J. Chem. Theory Comput.*, 2011, **7**, 2218–2223.
- 59 L. Wang, T. Maxisch and G. Ceder, *Phys. Rev. B: Condens. Matter Mater. Phys.*, 2006, **73**, 195107.
- 60 T. Das, S. Tosoni and G. Pacchioni, *Comput. Mater. Sci.*, 2019, **163**, 230–240.
- 61 S. Suthirakun, A. Genest and N. Rösch, *J. Phys. Chem. C*, 2018, **122**, 150–157.
- 62 S. Suthirakun, S. Jungthawan and S. Limpijumnong, *J. Phys. Chem. C*, 2018, **122**, 5896–5907.
- 63 N. V. Hieu and D. Lichtman, *J. Vac. Sci. Technol.*, 1981, **18**, 49–53.
- 64 H. J. Monkhorst and J. D. Pack, *Phys. Rev. B: Solid State*, 1976, **13**, 5188–5192.
- 65 H. Bachmann, F. Ahmed and W. Barnes, *Z. Kristallogr.*, 1961, **115**, 110.
- 66 V. Eyert and K. H. Höck, *Phys. Rev. B: Condens. Matter Mater. Phys.*, 1998, **57**, 12727–12737.

- 67 R. Enjalbert and J. Galy, *Acta Crystallogr., Sect. C: Cryst. Struct. Commun.*, 1986, **42**, 1467–1469.
- 68 W. Lambrecht, B. Djafari-Rouhani and J. Vennik, *J. Phys. C: Solid State Phys.*, 1981, **14**, 4785–4795.
- 69 A. Chakrabarti, K. Hermann, R. Druzinic, M. Witko, F. Wagner and M. Petersen, *Phys. Rev. B: Condens. Matter Mater. Phys.*, 1999, **59**, 10583–10590.
- 70 Q. Wang, M. Brier, S. Joshi, A. Puntambekar and V. Chakrapani, *Phys. Rev. B*, 2016, **94**, 245305.
- 71 R. De Francesco, M. Stener, M. Causà, D. Toffoli and G. Fronzoni, *Phys. Chem. Chem. Phys.*, 2006, **8**, 4300–4310.
- 72 K. Momma and F. Izumi, *J. Appl. Crystallogr.*, 2008, **41**, 653–658.
- 73 S. Na-Phattalung, M. F. Smith, K. Kim, M.-H. Du, S.-H. Wei, S. B. Zhang and S. Limpijumnong, *Phys. Rev. B: Condens. Matter Mater. Phys.*, 2006, **73**, 125205.
- 74 V. A. Ioffe and I. B. Patrino, *Phys. Status Solidi B*, 1970, **40**, 389–395.
- 75 R. Basu, A. K. Prasad, S. Dhara and A. Das, *J. Phys. Chem. C*, 2016, **120**, 26539–26543.
- 76 Z. R. Xiao and G. Y. Guo, *J. Chem. Phys.*, 2009, **130**, 214704.
- 77 A. B. Cezar, I. L. Graff, J. Varalda, W. H. Schreiner and D. H. Mosca, *J. Appl. Phys.*, 2014, **116**, 163904.
- 78 T. Kobayashi, T. Gake, Y. Kumagai, F. Oba and Y.-I. Matsushita, *Appl. Phys. Express*, 2019, **12**, 091001.
- 79 S. Limpijumnong, X. Li, S.-H. Wei and S. B. Zhang, *Appl. Phys. Lett.*, 2005, **86**, 211910.
- 80 S. B. Zhang and J. E. Northrup, *Phys. Rev. Lett.*, 1991, **67**, 2339–2342.
- 81 Z. Y. Li, C. K. Zhang, C. F. Liu, H. Y. Fu, X. H. Nan, K. Wang, X. Y. Li, W. D. Ma, X. M. Lu and G. Z. Cao, *Electrochim. Acta*, 2016, **222**, 1831–1838.
- 82 L. Xing, Q. Yu, Y. Bao, J. Chu, K. Han, S. Chong, C.-Y. Lao, F. Lai, P. Li, K. Xi and W. Wang, *J. Mater. Chem. A*, 2019, **7**, 25993–26001.
- 83 S. T. Murphy and N. D. M. Hine, *Phys. Rev. B: Condens. Matter Mater. Phys.*, 2013, **87**, 094111.
- 84 C. W. M. Castleton, A. Lee and J. Kullgren, *J. Phys. Chem. C*, 2019, **123**, 5164–5175.
- 85 P. Pakeetood, P. Reunchan, A. Boonchun, S. Limpijumnong, R. Munprom, R. Ahuja and J. T-Thienprasert, *J. Phys. Chem. C*, 2019, **123**, 14508–14516.
- 86 H. Choi, Y. J. Kwon, J. Paik, J.-B. Seol and Y. K. Jeong, *ACS Appl. Electron. Mater.*, 2019, **1**, 1881–1889.
- 87 J. Buckeridge, *Comput. Phys. Commun.*, 2019, **244**, 329–342.
- 88 J. Buckeridge, C. R. A. Catlow, M. R. Farrow, A. J. Logsdail, D. O. Scanlon, T. W. Keal, P. Sherwood, S. M. Woodley, A. A. Sokol and A. Walsh, *Phys. Rev. Mater.*, 2018, **2**, 054604.
- 89 A. Janotti, J. B. Varley, P. Rinke, N. Umezawa, G. Kresse and C. G. Van de Walle, *Phys. Rev. B: Condens. Matter Mater. Phys.*, 2010, **81**, 085212.
- 90 H. M. R. Giannetta, C. Calaza, D. G. Lamas, L. Fonseca and L. Fraigi, *Thin Solid Films*, 2015, **589**, 730–734.
- 91 M. Przeźniak-Welenc, N. A. Szreder, A. Winiarski, M. Łapiński, B. Kościelska, R. J. Barczyński, M. Gazda and W. Sadowski, *Phys. Status Solidi B*, 2015, **252**, 2111–2116.
- 92 A. Parija, Y. Liang, J. L. Andrews, L. R. De Jesus, D. Prendergast and S. Banerjee, *Chem. Mater.*, 2016, **28**, 5611–5620.
- 93 N. A. Deskins and M. Dupuis, *Phys. Rev. B: Condens. Matter Mater. Phys.*, 2007, **75**, 195212.
- 94 T. Maxisch, F. Zhou and G. Ceder, *Phys. Rev. B: Condens. Matter Mater. Phys.*, 2006, **73**, 104301.
- 95 V. Pasumarthi, T. Liu, M. Dupuis and C. Li, *J. Mater. Chem. A*, 2019, **7**, 3054–3065.
- 96 L. Sun, X. Huang, L. Wang and A. Janotti, *Phys. Rev. B*, 2017, **95**, 245101.
- 97 P. Liao, M. C. Toroker and E. A. Carter, *Nano Lett.*, 2011, **11**, 1775–1781.
- 98 F. Wu and Y. Ping, *J. Mater. Chem. A*, 2018, **6**, 20025–20036.
- 99 G. Henkelman, B. P. Uberuaga and H. Jónsson, *J. Chem. Phys.*, 2000, **113**, 9901–9904.

Abstract submitted in the 2nd Taiwan-Thailand-Vietnam Workshop on Theoretical
and Computational Chemistry (TTV2) (2019)



The 2nd Taiwan-Thailand-Vietnam Workshop on Theoretical and Computational Chemistry (TTV2)

**First-Principles Study of the Defect Formation in Sn-Doped V₂O₅ for
Li-ion Batteries**

Lappawat Ngamwongwan^{1,2}, Sirichok Jungthawan^{1,2}, Suwit Suthirakun^{2,3*}

¹*School of Physics, Institute of Science, Suranaree University of Technology,
Nakhon Ratchasima, 30000, Thailand*

²*Center of Excellence in Advanced Functional Materials, Suranaree University of Technology,
Nakhon Ratchasima, 30000, Thailand*

³*School of Chemistry, Institute of Science, Suranaree University of Technology,
Nakhon Ratchasima, 30000, Thailand*

*E-mail: suthirak@sut.ac.th

Abstract:

Orthorhombic vanadium pentoxide (V₂O₅) is one of the most promising cathode materials used in alkaline-ion batteries because of its high theoretical capacity. However, it still suffers from several limitations such as slow electrochemical kinetics and structural instability upon charge-discharge processes. Introduction of defects such as oxygen vacancy and impurities (Cr [1], Al [2], Cu [3] and Sn [4,5]) doping has intensively been proposed to alleviate the limitations. Although the experimental results of the Sn-doped V₂O₅ show a significant improvement of the overall electrochemical performance of the cathode [4,5], the origin of the enhancement is still unclear. To find theoretical explanations and better understand the role of Sn doping, we utilized the density functional theory (DFT+U) method to explore the stabilities of various defects. In particular, the energetic stabilities of point defect and the electronic structures were calculated to identify the most stable defect formation in the system. In addition, behavior of Li intercalation and diffusion will be examined to obtain insight into the origin of the enhanced charge transport kinetics. Theoretical understanding of the defect formation in the V₂O₅ based cathode materials could be one way to promote the improvement of the battery technologies.

References:

1. S. Zhan, C. Wang, K. Nikolowski, H. Ehrenberg, G. Chen, Y. Wei, *Solid State Ionics*, **180**, 1198-1203 (2009).
2. S. Zhan, Y. Wei, X. Bie, C. Wang, F. Du, G. Chen, F. Hu, *Journal of Alloys and Compounds*, **502**, 92-96 (2010).
3. H. Yu, X. Rui, H. Tan, J. Chen, X. Huang, C. Xu, W. Liu, D. Y. Yu, H. Hng, H. Hoster, Q. Yan, *Nanoscale*, **5(11)**, 4937-4943 (2013).
4. Y. Li, J. Yao, E. Uchakert, M. Zhang, J. Tian, X. Liu, G. Cao, *Journal of Physical Chemistry C*, **117(45)**, 23507-23514 (2013).
5. Z. Li, C. Zhang, C. Liu, H. Fu, X. Nan, K. Wang, X. Li, W. Ma, X. Lu, G. Cao, *Electrochimica Acta*, **222**, 1831-1838 (2016).

Keywords: Sn-doped V₂O₅, defect formation energy, density functional theory(DFT), Li-ion batteries

Abstract submitted in The International Centre for Theoretical Physics (ICTP) Asian
Network School and Workshop on Complex Condensed Matter Systems (2019)



Asian Network School and Workshop on Complex Condensed Matter Systems 2019
National Institute of Physics, University of the Philippines Diliman, Quezon City,
Philippines, Nov. 4 – 8, 2019

Effect of Dopant in Sn-doped V_2O_5 for Li-ion Batteries: A First-principles Calculation

Lappawat Ngamwongwan^{1,2}, Ittipon Fongkaew^{1,2}, Sirichok Jungthawan^{1,2},
Sukit Limpijumnong³, Suwit Suthirakun^{2,4}

¹*School of Physics, Institute of Science, Suranaree University of Technology, Nakhon
Ratchasima, 30000, Thailand*

²*Center of Excellence in Advanced Functional Materials, Suranaree University of
Technology, Nakhon Ratchasima, 30000, Thailand*

³*The Institute for the Promotion of Teaching Science and Technology (IPST), Bangkok
10110, Thailand*

⁴*School of Chemistry, Institute of Science, Suranaree University of Technology, Nakhon
Ratchasima, 30000, Thailand*

Abstracts:

Vanadium pentoxide (V_2O_5) is one of the most promising cathode materials used in metal-ion batteries due to its high theoretical capacity. However, it still suffers from several limitations such as slow electrochemical kinetics. Although the introduction of Sn impurities in V_2O_5 has been proposed to alleviate the kinetic drawback of the cathode, the origin of the enhancement is still vague. To find theoretical explanations and better understand the role of Sn dopants, we performed the density functional theory (DFT+U) method to identify the most energetically stable point defects in the presence of Sn dopants. Specifically, the stabilities of various point defects and charge carriers were compared in term of defect formation energy. Furthermore, the electronic structure of Sn-doped V_2O_5 was calculated to evaluate the electronic transport. Theoretical understanding of the defect formation in the V_2O_5 based cathode materials could be one way to promote the improvement of the battery technologies.

CURRICULUM VITAE

Mr. Lappawat Ngamwongwan was born on February 15, 1995 in Bangkok, Thailand. He received his Bachelor of Science in Physics (first-class honors with gold medal) in 2017 from the Department of Physics, Faculty of Science, Khon Kaen University. He has granted the scholarship from the Development and Promotion of Science and Technology Talents Project (DPST, THAILAND) since 2014. During his senior year in bachelor's degree, he started research in condensed matter physics using density functional theory under the supervision of Asst. Prof. Dr. Thanayut Kaewmaraya and Assoc. Prof. Dr. Nonglak Meethong. In 2018, he continued to pursue the Master's degree program in the School of Physics, Suranaree University of Technology with DPST scholarship under the supervision of Asst. Prof. Dr. Suwit Suthirakun and Assoc. Prof. Dr. Sirichok Jungthawan. He has published articles in international journals and participated in the international conferences (listed in APPENDIX B) during the course of his master program.